Theoretical Vibrational Spectroscopy of Ice

by

Liang Shi

A dissertation submitted in partial fulfillment of the requirements for the degree of

Doctor of Philosophy
(Chemistry)

at the
UNIVERSITY OF WISCONSIN-MADISON
2014

Date of final oral examination: 06/13/14

The dissertation is approved by the following members of the Final Oral Committee:

James L. Skinner, Professor, Chemistry
Edwin L. Sibert III, Professor, Chemistry
Gilbert M. Nathanson, Professor, Chemistry
Etienne Garand, Assistant Professor, Chemistry
Izabela Szlufarska, Associate Professor, Materials Science and Engineering

Abstract

Understanding ice, the solid state of water, has enormously broad and far-reaching implications for our daily life and basic science. In our endeavors to seek a better understanding of ice, vibrational spectroscopy has been and is still playing an essential role due to its sensitivity to molecular structure and motion. However, decoding molecular information from vibrational spectra often requires the assistance of theory and molecular simulations. This thesis presents our recent efforts simulating various vibrational spectroscopies of ice Ih, the most common form of ice, from realistic molecular models, and we believe that these efforts constitute a step towards a reliable and versatile simulation scheme for the vibrational spectroscopy of ice.

We first model the low-frequency infrared spectrum of ice Ih, which contains information about molecular arrangement and hydrogen bonding in ice, and a related macroscopic property, the static dielectric constant, which reveals the structural heterogeneity (proton disorder) in ice Ih. These pieces of information could be also extracted from high-frequency OH (OD) stretch optical vibrational spectroscopy. Both linear and nonlinear OH (OD) stretch optical vibrational spectroscopies of ice Ih are simulated in subsequent chapters, and the spectrum-structure relationship for ice Ih (e.g., relation between inhomogeneous broadening and proton disorder) is investigated on the basis of reasonable agreement between theory and experiment. In addition to optical vibrational spectroscopy, the last chapter of the thesis is devoted to the modeling of a different type of vibrational spectroscopy — incoherent inelastic neutron scattering — and connections and differences between these two types of vibrational spectroscopy is discussed.

Published work and work in preparation

[1] L. Shi, S. M. Gruenbaum and J. L. Skinner, "Interpretation of IR and Raman line shapes for H_2O and D_2O ice Ih" J. Phys. Chem. B **116**, 13821 (2012)

[2] C. J. Tainter, Y. Ni, L. Shi and J. L. Skinner, "Hydrogen bonding and OH-stretch spectroscopy in water: hexamer (cage), liquid surface, liquid, and ice." J. Phys. Chem. Lett. **4**, 12 (2013)

[3] S. M. Gruenbaum, C. J. Tainter, L. Shi, Y. Ni and J. L. Skinner, "Robustness of frequency, transition dipole, and coupling maps for water vibrational spectroscopy." J. Chem. Theory Comput. **9**, 3109 (2013)

[4] L. Shi and J. L. Skinner, "Proton disorder in ice Ih and inhomogeneous broadening in two-dimensional infrared spectroscopy." J. Phys. Chem. B **117**, 15536 (2013)

[5] C. J. Tainter, L. Shi and J. L. Skinner, "Structure and OH-stretch spectroscopy of low- and high-density amorphous ices." J. Chem. Phys. **140**, 134503 (2014)

[6] L. Shi, F. Li and J. L. Skinner, "Resonant vibrational energy transfer in ice Ih." J. Chem. Phys. submitted.

[7] L. Shi, Y. Ni, S. E. P. Drews and J. L. Skinner, "Dielectric constant and structure, low-frequency infrared spectra for water and ice Ih within the E3B model." in preparation.

Contents

List of Figures

List of Tables

Acknowledgments

I would like to thank many people for helping and supporting (as well as tolerating) me in my endeavor of getting my Ph.D. in the past five years.

I thank Jim for being a great advisor, not only on research, but also on how to be a scholar. I remember that after my TBO practice talk, he spent hours sharing his ideas on organizing presentations with me. I also remember that he put aside his own work, and helped me figure out the hopping rate expression step-by-step (impressively he worked out the expression very quickly). When I was stuck with my first project, he not only encouraged me, but also led me to other research directions, which turned out to be more fruitful.

Thank Piotr and Josh for being great office mates. Piotr, a very nice and smart gentleman, taught me how to do research efficiently, and was always ready to help me, then a rookie in theoretical chemistry. He was unique in the way that he would think hard about other people's projects (e.g., supercritical water project) like his own projects, and never hesitated to share his clever ideas (e.g., THz project) with others. Josh, my English teacher, has been a great companion in the office for almost four years. I clearly remember how my drafts for posters and research statement looked after his revisions (or rewriting). His capability of explaining things in a very intuitive way really helped me prepare my talks and come up with physical interpretations for some results in my research. As good friends, Piotr and Josh, I will never forget the good time we had during lunch, and the shot glasses in our office.

Thanks to other Skinner group members, Fu, Scott, Craig, Lu, Mino, Yicun, Zak, Santanu, and my undergraduate coworker, Sam, for making the Skinner group a coherent/pleasant group to work in. Fu pioneered the ice projects in our group, which turned out to be the main body of my graduate research. Scott brought a lot of fun to my graduate life (e.g., making coffee, apple time, and Christmas party), and was very helpful in revising my first paper. Craig kindly answered a lot of my questions on using E3B models (even after he left the group), and Lu helped me a lot with my RP on proteins. I am also very thankful to Mino (on VET), Yicun (on THz), Zak (on dielectrics) and Santanu for many helpful scientific discussions. Also I would like to thank Sam for turning an undergraduate research project into an interesting paper. I really feel privileged to work with these smart and nice people.

Many faculty in chemistry department have played important roles in my graduate education in Madison. Thanks to Ned and Gil for advising me throughout my graduate years. I was

impressed by Gil's enthusiasm about teaching, and his expertise on stat mech was demonstrated in my TBO when he asked me about the connection between PMF and RDF. Ned taught me chemical dynamics at TSTC, and his expertise on that was shown in my RP when he pointed out that using DVR for the momentum operator is tricky. I also would like to thank Ned and JR for their support in my postdoc application. I also thank QC for offering me the chance to work in this department in the first place (and of course teaching me QC). Arun's advice on how to succeed in graduate school in my first year was also helpful. I also would like to thank Prof. Cathy Middlecamp, with whom I did my TA in my first semester, for helping me a lot with my teaching.

My graduate life would not be as smooth as it is without the excellent staff in the chemistry department. I am very grateful to Betty Harwood for her continuous help in all kinds of things I don't really understand (e.g., SSN, insurance, taxes). She and Matt Sanders (as well as Jim, Gil) alleviated my stress in my first several months in US. I also would like to thank April, Stephenie, Alan and other staff on the 9th floor for making my life easy in the department.

I would like to thank many fellow students for being good friends with me. Just name a few: Zhe and Kuang helped me settle down in Madison, and Fei and Zhigeng always lent their hands when I needed help. I also learned a lot (both teaching strategies and course materials) from other TAs in Chem108, Marilyn, Ross, Patrick and Craig. Amber, Jessie, and Kuang have taught me a lot beyond my research areas in journal club. Without all the friends here, my graduate life in Madison would not be as pleasant as it is.

Lastly and most importantly. I owe so much gratitude to my family. My parents have always been the source of support and encouragement, and most importantly they gave me a lot of freedom along my education (even said okay when I had to stay over 10000 km away from them). My grandparents on both sides also played vital roles in my growth, and it is always pleasant to talk with them. I also feel extremely lucky to have my wife, Li, around to share my happiness and sorrow in the past 5 years, and her patience with me is incredibly valuable to me.

Chapter 1

General Introduction

Contents

1.1 Motivation for Studying Ice

He raised a finger and winked at me. "But suppose, young man, that one Marine had with him a tiny capsule containing a seed of ice-nine, a new way for the atoms of water to stack and lock, to freeze. If the Marine threw that seed into the nearest puddle . . ."
"The puddle would freeze?" I guessed.
. . .
"And the rain?"
"When it fell, it would freeze into hard little hobnails of ice-nine - and that would be the end of the world! And the end of the interview, too! Good-bye!"
- Kurt Vonnegut, *Cat's Cradle*

Fortunately, the devastating "ice-nine" in Vonnegut's fiction does not exist in real life (the real "ice IX" has nothing to do with the fictional "ice-nine"). However, understanding ice is still essential for our life, especially in the modern era.[1] Modern aviation industry connects people all over the world, and flight safety is its most important concern. One serious hazard to flight safety is actually in-flight icing,[2] and some fatal accidents were due to the formation of ice crystals on aircrafts (e.g., the Air France Flight 447 accident).[3] The basic scientific question here is how to prevent ice formation from supercooled moisture (water droplets) in clouds, and its solutions rely on our understanding of homogeneous or heterogeneous ice nucleation. Understanding ice is also important for ground transportation, especially for people living in cold regions. During the winter season, roads and highways in these cold regions might be shifted or deformed due to the effects of frost heaves.[4] It is often mistakenly thought that simply the expansion of water on freezing gives rise to this destruction. However, frost heaving is a very complex non-equilibrium process, and it involves ice surface premelting and ice segregation within porous materials.[4] In order to reduce these destructive effects, one needs to understand ice surface premelting and ice nucleation in confined environments.

Because of its extreme practical importance, ice has been an exciting research topic for over a century, and an enormous number of studies have been published. Comprehensive discussions could be found in some books and many review articles,[5–7] and only a few historical milestones will be mentioned here to emphasize the importance of studying ice in basic science. In 1900, the polymorphism of ice was discovered by Tammann,[8] and since then the effort to find new phases of ice has lasted for over a century and is still going on. So far there are 16 crystalline phases and 3 amorphous phases for ice,[9] the most common form of which in daily life is hexagonal ice, also called ice Ih. Investigating the rich phase behavior of ice greatly advances our understanding of molecular systems (e.g., packing, order-disorder transition).[10] Around 1935, Bernal, Fowler, and Pauling proposed a structure for ice Ih (i.e., the Pauling structure),[11,12] which was confirmed by neutron diffraction experiments in 1949.[13] In this structure, the orientations of water molecules are disordered, and this disorder remains down to extremely low temperature, making ice Ih the first identified frustrated system. Motivated by this structure, people have proposed and prepared a type of magnetic system analogous to ice Ih, called "spin ice",[14,15] which is relatively a new topic in materials science. In the 1970s, people started building "artificial" ice Ih in computers,[16–18] and since then computer simulation of ice has been an

indispensible part of ice research. Moreover, simulating the properties and phase diagram of ice has been a common practice to benchmark or develop water models recently.[19–21] Therefore, the aforementioned progress in the research field of ice not only elucidated some important problems about ice, but also provided new insights to relevant scienctific topics.

1.2 Present Knowledge of Ice Ih

This section is meant to provide briefly a contemporary picture of a perfect crystal of ice Ih at the molecular level based on studies since the beginning of the last century. A twelve-molecule fragment of ice Ih is shown in Fig. 1.1, in which the blue spheres are oxygen atoms and the smaller white spheres are hydrogen atoms. It is clear from Fig. 1.1 that the oxygen atoms form a regular hexagonal lattice, and each water molecule is still intact in perfect ice Ih. Between two adjacent oxygen atoms, there is one and only one hydrogen atom (we are not considering defects here), which binds to one oxygen covalently, and to the other one via a hydrogen bond (HB). However, which oxygen atom is binded covalently to hydrogen is more or less random as long as each oxygen atom has two covalently bonded hydrogen atoms and two hydrogen bonded ones. As a result, the orientation of the water molecule in ice Ih is disordered, and this disorder is called proton disorder in the literature. The rules described above are the famous Bernal-Fowler ice rules,[11] and the resulting ice Ih structure is the Pauling structure.[12] This proton disorder leads to many peculiar properties of ice Ih, such as residual entropy, large static dielectric constant, etc.[7] Regarding the molecular dynamics (molecular motions) in ice Ih, there are two types of motions, well-separated in their time scales. One is hindered translation and rotation (i.e., libration) due to thermal fluctuation. These hindered motions involve small but fast displacement or distortion of water molecules, and the hinderance comes from the constraints exerted by the hydrogen-bond network in ice Ih. The other type of motion is the reorientation of water molecule, which requires a large activation energy and local violations of the Bernal-Fowler ice rules (i.e., defects). This is a very slow process in pure ice Ih, and its (Debye) relaxation time scale is about a μs at $T = -10\,^{\circ}\mathrm{C}$, and many years at 100 K.[7,22] However, this slow motion makes possible the interchange of all configurations allowed by the ice rules, giving rise to the large static dielectric constant of ice Ih. Note that here we adopt a molecular perspective (the water molecule is always intact), but in reality the reorientation of

water molecule in ice Ih can be achieved by ionic defects in addition to the defects mentioned above (i.e., Bjerrum defects), and both types of defects lead to the protonic conductivity of ice Ih (see Ref. 7). The next section aims to provide a brief introduction of vibrational spectroscopy as a tool to probe molecular structure and dynamics of ice Ih.

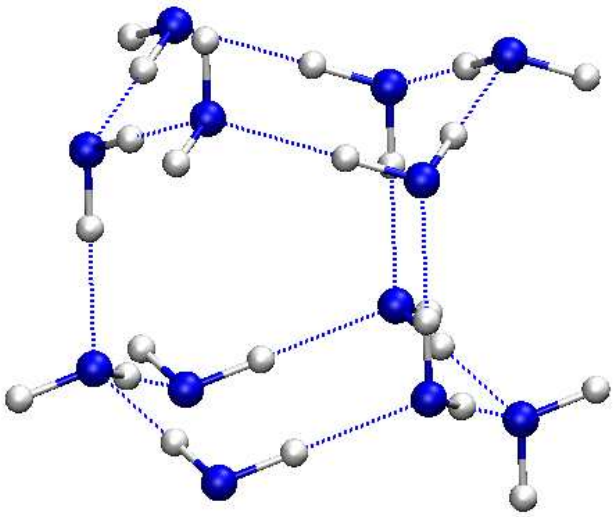

Figure 1.1: 12-molecule fragment of ice Ih. Blue spheres are oxygen atoms, smaller white spheres are hydrogen atoms, and the dotted lines are hydrogen bonds. The crystallographic c axis in hexagonal lattice is vertical.

1.3 Vibrational Spectroscopy

Vibrational spectroscopy has been a very useful tool to study the structure and dynamics of condensed phase systems. In a typical vibrational spectroscopic measurement, the condensed phase system is perturbed by incident waves (e.g., electromagnetic fields, neutrons), and experimentalists record the response of the nuclei in the condensed phase system to the external perturbation. Assuming that the perturbation is small (which usually is a good approximation), one can extract structural and dynamical information about the unperturbed system from the response. This section will briefly discuss how people can learn something from vibrational spectroscopy about structure and dynamics of a particular system — ice Ih.

1.3.1 As a Probe of Molecular Structure

There are at least two strategies in terms of probing molecular structures using vibrational spectroscopy. One is using a vibrational chromophore (e.g., OH or OD stretch in water,[23] amide I mode in proteins,[24]and CN stretch in biological systems[25]) to probe the molecular structure around it. Such a chromophore usually has a large absorption coefficient, and its vibrational frequency is very sensitive to changes in its local environment (e.g., hydrogen bonding). For ice Ih, the commonly chosen vibrational chromophore is the OH or OD stretch as it has a large absorption coefficient, and the OH vibrational frequency is red-shifted by hundreds of wavenumbers when it forms hydrogen bonds to nearby water molecules. In the 1930s, the similarities between the Raman spectra (OH stretch region) of water vapor, liquid water and ice Ih led Bernal and Fowler to speculate that the H_2O molecule's integrity is retained in ice Ih.[11] However, the further establishment of the spectrum-structure relationship for pure H_2O ice Ih was largely hindered due to vibrational couplings. Many OH chromophores in ice are near-degenerate, and the vibrational couplings between them delocalize the vibrational eigenstates to some extent, making the structural interpretation of the spectra very challenging. In the 1960s, experimentalists started measuring OH (OD) vibrational spectra for isotope-diluted ice Ih, such as dilute HOD in D_2O.[26–28] Because of the large frequency mismatch between OH and OD stretches, the OH stretch local mode is now essentially a normal mode, and its frequency is mainly affected by its local environment. Therefore, the spectrum of such an isotope-diluted system reflects the heterogeneity of local molecular environments in the system, as is discussed thoroughly in Chapter 6. Another strategy is to make use of the interactions or correlations between (nearby) molecules in condensed phase systems. One particularly useful technique is coherent neutron scattering,[29] from which one can extract the radial distribution function, one key quantity characterizing molecular arrangement in condensed phases. Historically, Pauling's proposed structure for ice Ih was verified by this type of neutron scattering technique in 1949,[13] as this techique is sensitive to hydrogen atoms (hydrogen has a larger neutron scattering cross section than oxygen). For optical vibrational spectroscopy, as discussed above, the OH stretch spectra for pure H_2O ice Ih is influenced by OH vibrational coupling, which also carries some information about local molecular structure. However, the extraction of this information from spectra usually requires theoretical modeling, and our efforts on this are presented in Chapter 4. Vibrational coupling can also lead to resonant vibrational energy transfer, and if Förster theory

(an approximate theory for incoherent resonant electronic energy transfer, see Chapter 5) could be applied here, information about molecular distance and orientation could be obtained just like in the case of electronic energy transfer.[30] In fact, experimentalists have taken advantage of this to study ice Ih,[31] and our theoretical interpretation on this is reviewed in Chapter 5.

1.3.2 As a Probe of Molecular Dynamics

There are at least two windows in the vibrational spectra of ice Ih from which people can learn something about molecular dynamics. One regime is below about 1000 cm^{-1}, which reflects intermolecular motions directly. For example, a peak at about 225 cm^{-1} in the IR spectrum of pure H_2O ice Ih at 266 K[32] is usually assigned to hydrogen bond stretching mode. The reproduction of this peak in theoretical modeling is discussed in Chapter 3. Details of this hydrogen bond stretching motion can also be inferred from another regime of the vibrational spectra — the OH-stretch region. Considering dilute HOD in D_2O ice Ih, the OH-stretch frequency fluctuates due to the change of its local environment, which results from intermolecular motions (low-frequency motions modulate high-frequency vibrations), in particular from the hydrogen bond stretching motion.[23,33–35] Therefore, if one can extract the time scale of the OH-stretch frequency fluctuation from OH-stretch spectra, one would know something about the intermolecular motions. In fact, people have done this by analysing the line-widths of linear spectra and performing ultrafast nonlinear vibrational spectroscopic experiments.[35,36] This is further discussed briefly in Section 6.5.

A technique worth mentioning separately from the above general discussion is incoherent inelastic neutron scattering (IINS). In linear optical vibrational spectroscopy (e.g., IR and Raman), the perturbation to the system due to electromagnetic waves is largely through the dipole moment (or induced dipole) of the system. Therefore, the spectral intensity is determined not only by the intrinsic vibrational motion (i.e., vibrational density of states) but also by the dipole moment change associated with the vibrational motion.[37] This is basically the origin of the so-called selection rules for IR and Raman spectra. However, within reasonable approximations, IINS can provide direct information about vibrational density of states.[37–39] Moreover, for hydrogen-containing systems, it is possible to extract the hydrogen velocity time correlation function from IINS.[40] This provides a direct route to the comparison with molecular dynamics simulations. Chapter 7 is devoted to the modeling of IINS spectra for ice Ih as well as liquid

and supercooled water.

1.4 Role of Theoretical Vibrational Spectroscopy

If experiment can be regarded as a top-down approach (i.e., speculating microscopic details by observing macroscopic signals), theoretical modeling is often a bottom-up approach: one builds an artificial molecular system (e.g., molecular dynamics (MD) and Monte Carlo (MC) simulations with model Hamiltonians), then calculates macroscopic observables from that using appropriate theories. Nowadays, it is quite common to combine these two approaches: experimentalists need modeling to verify their speculations or interpret their observations, and theorists need experiment to validate their artificial molecular systems. In this sense, theoretical simulations of vibrational spectroscopy are used widely to bridge the gap between experimental spectroscopic measurements and molecular simulations. The next section is dedicated to the formulation of theoretical vibrational spectroscopy with a focus on a mixed quantum/classical approach developed in the Skinner group.[23]

Chapter 2

Line Shape Theory and Its Implementation

Contents

The scope of this chapter is limited to linear vibrational spectroscopy, and the discussion is started with using Fermi's Golden Rule based on the first-order time-dependent quantum-mechanical perturbation theory. For nonlinear spectroscopy, the nonlinear response theory is laid out in great detail in Ref. 41, and will be mentioned when necessary in subsequent chapters. In order to keep the notation clean, unless we redefine them, throughout the thesis we use (i) i, j, l as indices for OH (OD) stretch local modes and associated OH bonds or H atoms (when i is not an index, it is usually the imaginary unit), (ii) p, q, r, s as indices for Cartesian components. The dot above a symbol denotes a time derivative.

2.1 Line Shape and Time Correlation Function

In this section, the procedure to derive a time correlation function formula for the line shape is outlined briefly, and the details can be found in Ref. 37. Within the weak perturbation approximation, the cross section of absorption or scattering can be written in a sum-over-states form based on Fermi's Golden Rule (for neutron scattering, the neutron-nuclei interaction is defined by the Fermi pseudopotential, and its sum-over-states formula is called first Born approximation[37]). By using the Fourier transform representation of the delta function, the sum-over-states expression can be recast into a formula containing the (full or half) Fourier transform of a time correlation function (TCF) in the Heisenberg picture of quantum mechanics. The Fourier transform of that TCF is usually defined as the line shape function (for neutron scattering, the TCF is called the intermediate scattering function, and its Fourier transform is called the scattering function). In this chapter, we will use the term "line shape function" as a more general term for the Fourier transform of some TCF. Therefore, the focus of the spectral calculation is a quantum-mechanical time correlation function, the general form of which is given by

$$C_{AB}(t) = \langle A(t)B(0)\rangle\,, \tag{2.1}$$

where $A(t) = U^{\dagger}(t)AU(t)$, $U(t) \equiv e^{-iHt}$, and H is the unpertubed Hamiltonian of the whole system. The brackets denote an equilibrium quantum-mechanical ensemble average. Note that throughout the thesis, $\hbar = 1$. A listing of vibrational spectra and their corresponding TCFs is shown in Table 2.1. The full Fourier transform in this thesis is defined as

$$F(\omega) = \frac{1}{2\pi}\int_{-\infty}^{\infty} e^{i\omega t} f(t)dt. \tag{2.2}$$

The integration interval of the half Fourier transform is $[0, \infty]$.

Spectrum	Observable	$A(t)$	$B(0)$	Fourier transform
IR[37]	$I_p(\omega)$	$M_p(t)$	$M_p(0)$	full
Raman[37]	$I_{pq}(\omega)$	$\alpha_{pq}(t)$	$\alpha_{pq}(0)$	full
SFG[42]	$\chi^R_{pqr}(\omega)$	$\alpha_{pq}(t)$	$M_r(0)$	half
VCD[43]	$\Delta I_p(\omega)$	$M_p(t)$	$D_p(0)$	full*
IINS[37]	$S(\vec{k},\omega)$	$e^{-i\vec{k}\cdot\vec{r}_j(t)}$	$e^{i\vec{k}\cdot\vec{r}_j(0)}$	full

Table 2.1: Some vibrational spectra and corresponding TCFs. SFG: sum-frequency generation; VCD: vibrational circular dichroism; IINS: inelastic incoherent neutron scattering; $I(\omega)$: line shape function; $\chi^R(\omega)$: resonant part of the second-order susceptibility for SFG; $\Delta I(\omega)$: VCD line shape function; $S(\vec{k},\omega)$: incoherent scattering function; $\vec{k}$: momentum transfer in IINS; M: electric dipole; α: polarizability; D: magnetic dipole; $\vec{r}$: position of nucleus; *: for VCD line shape, one needs to take the imaginary part after performing the Fourier transform; p, q, r are Cartesian coordinate indices.

2.2 Approximation: System-Bath Treatment

It is quite common in condensed phases that some motions are fast, and some are slow relatively. For nuclear motions in ice Ih, intramolecular stretching and bending motions are fast (i.e., high-frequency), and intermolecular libration and translation are slow (i.e., low-frequency). The separation of timescales leads us to divide the material into two parts: system and bath. The system consists of fast degrees of freedom, while the bath consists of the slow modes. This division is not necessary, but it allows different levels of theoretical treatments for the system and bath, especially when one is only interested in the system. Regarding the vibrational spectroscopy of ice Ih, many studies focus on the low-frequency region or the OH (OD) stretch region. Even though the HOH (DOD) bending mode can couple to low-frequency modes or OH (OD) stretches (e.g., via Fermi resonance), some previous studies suggested that this effect is usually secondary.[44–46] As a result, the bending mode is neglected in this work (note that we do not have to do so). Similarly, when we consider dilute HOD in D_2O ice Ih, we ignore OD stretches. The system now is formed by all the OH (OD) stretches of interest on the ground

electronic Born-Oppenheimer potential energy surface (PES), and librations and translations (i.e., phonons) constitute the bath. The OH (OD) stretch frequency is usually over 3000 (2000) cm^{-1}, its accurate treatment requires quantum mechanics at typical temperatures (i.e., $T <$ 300 K) as $\hbar\omega \gg k_B T$ ($k_B T \approx 200$ cm^{-1} at 300 K). For the bath, there is no guarantee that classical mechanics is sufficient; however, many rigid water models have been able to reasonably reproduce many properties (thermodynamic, structural, and dynamical) of water and ice Ih. Moreover, several path-integral based simulations showed that quantum treatment of nuclei does not change the classical results for the low-frequency IR spectrum (below 1000 cm^{-1}) for liquid water by much.[46,47] Therefore, for the sake of computational efficiency, we use classical molecular dynamics with rigid water models to treat the bath. A comprehensive discussion on different levels of treatments for vibrational spectroscopy can be found in Ref. 23, and the rest of this section briefly reviews the key steps in the system–bath treatment.

Suppose that we are considering the OH stretches as the system. The full Hamiltonian can be written as

$$H = H_0 \left|0\right\rangle \left\langle 0\right| + \sum_i H_i \left|i\right\rangle \left\langle i\right| + \sum_{i \neq j} H_{ij} \left|i\right\rangle \left\langle j\right|, \tag{2.3}$$

where $\left|0\right\rangle$ is the vibronic ground state, $\left|i\right\rangle$ is the vibronic state where only the ith OH chromophore is excited to its first vibrational excited state on the ground electronic PES ($i, j > 0$), $H_i \equiv \left\langle i\right| H \left|i\right\rangle$, and $H_{ij} \equiv \left\langle i\right| H \left|j\right\rangle$. By writing the Hamiltonian in this way, we are using the OH stretch local modes (i.e., diabatic states) rather than normal modes as the basis, and neglecting the vibrational couplings between ground state and excited states. Note that H_0, H_i and H_{ij} are bath operators now.

To proceed further, we employ the system–bath treatment based on the well-separated time scales of the system and bath, and invoke an adiabatic approximation: the total density operator ρ can be written as

$$\rho \approx \rho_s \rho_b, \tag{2.4}$$

where ρ_s and ρ_b are system and bath density operators, respectively (note that the time dependence is with operators). By doing this, we ignore the energy dissipation from system to bath, which in reality is important (in other words, we only have vibrational phase relaxation, but no energy relaxation). At ambient or lower temperatures, only $\left|0\right\rangle$ is significantly populated in the system, and $\rho_s^{eq} \approx \left|0\right\rangle \left\langle 0\right|$. For the bath, $\rho_b^{eq} \approx \rho_0 \equiv e^{-\beta H_0} / \text{Tr}_b e^{-\beta H_0}$, where $\beta \equiv 1/k_B T$, and

Tr_b denotes a trace over bath degrees of freedom.

With the completeness relation for the system $I_s = \sum_i |i\rangle \langle i| + |0\rangle \langle 0|$, Eq. (2.3) becomes

$$H = I_s \otimes H_0 + \sum_i (H_i - H_0) |i\rangle \langle i| + \sum_{i \neq j} H_{ij} |i\rangle \langle j| . \tag{2.5}$$

Now, we move to work in the interaction picture of quantum mechanics with $I_s \otimes H_0$ as the reference Hamiltonian. Note that we always use this as our reference Hamiltonian even when the second vibrational excited state is accessible in nonlinear spectroscopy, in contrast to the reference choices in Ref. 41. The reason for this is that we will later run classical MD simulations with rigid water models, in which we are sampling the configuration space of H_0. The standard machinery in the interaction picture[41] leads to the following expression for $C_{AB}(t)$

$$C_{AB}(t) \approx \mathrm{Tr}_b \rho_0 \langle 0| U_I^\dagger(t) A_I(t) U_I(t) B(0) |0\rangle , \tag{2.6}$$

where $U_I(t) = e^{iI_s \otimes H_0 t} U(t)$, and $A_I(t) = e^{iI_s \otimes H_0 t} A e^{-iI_s \otimes H_0 t}$. Inserting the completeness relation of the system states three times results in the expressions

$$C_{AB}(t) = C_{AB}^l(t) + C_{AB}^h(t), \tag{2.7}$$

where

$$C_{AB}^l(t) = \langle A_{00}(t) B_{00}(0) \rangle_b , \tag{2.8}$$

and

$$C_{AB}^h(t) = \sum_{ij} \langle A_{0i}(t) U_{ij}(t) B_{j0}(0) \rangle_b . \tag{2.9}$$

$C_{AB}^l(t)$ (l here is for low-frequency) is related to calculations of low-frequency vibrational spectroscopy (bath motions: molecular translations and rotations), and $C_{AB}^h(t)$ is related to calculations of high-frequency vibrational spectroscopy (system motions: OH stretches). Other symbols are defined as follows: $\langle \cdots \rangle_b \equiv \mathrm{Tr}_b\{\rho_0 \cdots\}$, $A_{00}(t) \equiv \langle 0| A_I(t) |0\rangle$, $B_{00}(0) \equiv \langle 0| B(0) |0\rangle$, $A_{0i}(t) \equiv \langle 0| A_I(t) |i\rangle$, $B_{j0}(0) \equiv \langle j| B(0) |0\rangle$, and $U_{ij}(t) \equiv \langle i| U_I(t) |j\rangle$. The next three sections are devoted to the implementations of the above theory in three different frequency regimes: very low frequency regime (below 100 MHz), THz and far-infrared regime (10 – 1000 cm^{-1}), and mid-infrared regime (OH or OD stretch).

2.3 Static Dielectric Constant: Slow Long-Range Structure Fluctuation

The static dielectric constant is a macroscopic property of molecular system (most molecular systems are dielectric materials), which tells how the charges in a molecular system are re-distributed to respond to a static, external electric field. Therefore, if molecular rearrangement gives rise to large change in the total dipole moment of the molecular system (in other words, the dipole surface is very rough), the molecular system will have a large static dielectric constant. By examining the static dielectric constant, one could learn something about the slow long-range structural change of the molecular system. In this section, we derive the microscopic expression for the static dielectric constant from absorption line shape theory, rather than from direct perturbative treatment based on the macroscopic radiation-matter interaction.[48–50] However, since the basis of the (linear) line shape theory is the same perturbative treatment, both derivations essentially carry the same approximations (e.g., first-order perturbation, electric dipole approximation). The advantage of the indirect derivation below is that one can see clearly what kind of motions significantly contribute to the static dielectric constant.

To simplify the derivation, we assume the material of interest is isotropic (i.e., $\langle M_p(t)M_p(0)\rangle = \left\langle \vec{M}(t)\cdot\vec{M}(0)\right\rangle/3$)[37] and not ferroelectric (i.e., $\langle M_p\rangle = 0$). The absorption line shape $I(\omega)$ is the Fourier transform of total dipole TCF, $C_{MM}(t) = \left\langle \vec{M}(t)\cdot\vec{M}(0)\right\rangle$, and is related to the frequency-dependent imaginary part of the dielectric constant $\varepsilon''(\omega)$ through

$$\varepsilon''(\omega) = \frac{4\pi^2(1-e^{-\beta\hbar\omega})}{3\hbar V} I(\omega), \tag{2.10}$$

where V is the volume of the material (assuming the whole material is absorbing light), and $\hbar$ is shown explicitly here for clarity. Note that the real and imaginary parts of the complex dielectric constant (i.e., $\varepsilon'(\omega)$ and $\varepsilon''(\omega)$) are related through the Kramers-Kronig relation,[51] so we have

$$\varepsilon_s \equiv \varepsilon'(0) = 1 + \frac{1}{\pi}\text{P.P.}\int_{-\infty}^{\infty} d\omega \frac{\varepsilon''(\omega)}{\omega}, \tag{2.11}$$

where ε_s is static dielectric constant and P.P. denotes the Cauchy principle value concerning the singularity at $\omega = 0$. Combining Eq. (2.10) and (2.11), the static dielectric constant can be

obtained from the absorption line shape through

$$\varepsilon_s = 1 + b \int_{-\infty}^{\infty} \frac{1 - e^{-\beta\hbar\omega}}{\beta\hbar\omega} I(\omega) d\omega, \tag{2.12}$$

where $b = 4\pi\beta/3V$. Note that P.P. is not needed because the singularity is gone. Eq. (2.12) implies that only the low-frequency part of absorption spectrum will significantly contribute to the static dielectric constant due to the ω factor in the denominator, and this is consistent with the descriptive discussion in the previous paragraph. In practice, the static dielectric constant is usually extrapolated from the measurement of frequency-dependent dielectric constant by assuming Debye relaxation model and using the Cole-Cole diagram.[7,22,52] Next, we may ask how low frequency must be to generate a significant contribution to the ε_s. To do this, we define a cutoff frequency ω_0 and partition Eq. (2.12) into two parts:

$$\varepsilon_s = \varepsilon_\infty + b \int_{-\omega_0}^{\omega_0} \frac{1 - e^{-\beta\hbar\omega}}{\beta\hbar\omega} I(\omega) d\omega, \tag{2.13}$$

where

$$\varepsilon_\infty \equiv 1 + b \int_{\omega_0}^{\infty} \frac{1 - e^{-\beta\hbar\omega}}{\beta\hbar\omega} I(\omega) d\omega + b \int_{-\infty}^{-\omega_0} \frac{1 - e^{-\beta\hbar\omega}}{\beta\hbar\omega} I(\omega) d\omega. \tag{2.14}$$

ε_∞ takes into account the contribution from the high-frequency part, which is presumably small. There are at least three choices of ω_0 for liquid water and ice Ih. One is the onset frequency of the optical (electronic) part of absorption spectrum, in which case ε_∞ is related to optical refractive index n_{op} through $\varepsilon_\infty = n_{op}^2$, and also to the (isotropic) molecular polarizability through Clausius-Mossotti relation (also called Lorenz-Lorentz relation if n_{op} is used instead of ε_∞) within a simple classical dielectric model.[51] Another choice is to place ω_0 in the MHz region (e.g., 100 MHz),[53] which is often used by experimentalists to measure the static dielectric constant. In this case, ε_∞ includes the contributions from electronic response, intramolecular vibrations and most intermolecular vibrations, which are usually still small. The last term on the right-hand-side (RHS) of Eq. (2.13) is then due to very low-frequency long-range structural rearrangment (also see Section 1.2), which accounts for the majority of the static dielectric constant. Note that since the relevant frequency is so low (for ω_0=100 MHz, $\beta\hbar\omega_0 \approx 0.000016$ at 300 K), a classical treatment is sufficient. The last senario is for molecular simulations with nonpolarizable rigid water models, in which electronic degrees of freedom and intramolecular

vibrations are frozen, and ω_0 is around 1200 cm^{-1}. Fortunately, as the contributions from high-frequency motions (electronic motion and vibrations) to the static dielectric constant are fairly small for liquid water and ice Ih, there is not a significant difference between these three choices in practice. However, it is important to keep in mind that only in the second case is the classical treatment of the problem entirely justified, although in practice a classical treatment can also be applied to the third case.

Now, we focus on the third case, and recall the discussion in Section 2.2. Replacing $I(\omega)$ with $I^l(\omega)$ and extending the integral limits of the last term in Eq. (2.13) to infinity (allowed because $I^l(\omega)$ is zero for $|\omega| > \omega_0$), we have

$$\varepsilon_s = \varepsilon_\infty + b \int_{-\infty}^{\infty} \frac{1 - e^{-\beta\hbar\omega}}{\beta\hbar\omega} I^l(\omega) d\omega, \tag{2.15}$$

where $I^l(\omega)$ is the Fourier transform of $C^l_{MM}(t) = \left\langle \vec{M}_{00}(t) \cdot \vec{M}_{00}(0) \right\rangle_b$ (see Eq. (2.8). Taking the classical limit ($\hbar \to 0$ or $\beta \to 0$) and using the Fourier transform representation of the delta function, we reach the widely used expression for the static dielectric constant:[48–50]

$$\varepsilon_s = \varepsilon_\infty + \frac{4\pi\beta}{3V} \left\langle \vec{M}_{00} \cdot \vec{M}_{00} \right\rangle_b, \tag{2.16}$$

where the brackets with subscript b now are an equilibrium classical ensemble average over the bath. Eq. (2.16) and Eq. (2.10) only work with the conducting boundary condition in simulations, which is used in all the simulations in this thesis (note that the line shape function is independent of the choice of boundary condition, but how the line shape is related to the complex dielectric constant is not.).[54] In addition, the assumption that the system is isotropic and not ferroelectric is not necessary, and a more general expression can be obtained easily by redefining the TCF and considering ε_s as a tensor. In most cases, one can easily find dielectric principal axes (e.g., crystallographic axes for hexagonal crystals) to make the static dielectric constant tensor diagonal, and obtain the following expression:[50,55]

$$\varepsilon_{s,pp} = \varepsilon_{\infty,pp} + \frac{4\pi\beta}{V} (\left\langle M^2_{00,p} \right\rangle_b - \langle M_{00,p} \rangle^2_b), \tag{2.17}$$

where p is the coordinate in the frame formed by the dielectric principal axes.

2.4 Low-Frequency Vibrational Spectroscopy: Intermolecular Motions

As discussed in Section 1.3.2, the low-frequency window (below about 1000 cm^{-1}) can provide useful information about the molecular dynamics of liquid water or ice Ih. Since the frequency of interest is low, classical mechanics might be sufficient. The working equation in this section is Eq. (2.8) and the ensemble average there is still quantum mechanical but only over bath degrees of freedom. The simplest way forward is to replace the quantum ensemble average with its classical counterpart, and to perform classical MD simulations to evaluate this average. However, as the frequencies of most intermolecular vibrations are still not low enough to be considered entirely classical, a more correct method is to run quantum MD simulations, which are usually expensive. One simple method that balances accuracy and efficiency is the application of a quantum correction factor (QCF) $Q(\omega)$: one first performs a classical MD simulation to obtain the classical lineshape $I^{cl}(\omega)$, and multiplies it by $Q(\omega)$ to get the quantum line shape $I(\omega)$,[23,56]

$$I(\omega) = Q(\omega)I^{cl}(\omega). \tag{2.18}$$

This simple correction is phenomenological, but at least guarantees the symmetry property of quantum $I(\omega)$ (i.e., detailed balance for quantum TCF).[57] Fuller discussions on QCFs can be found in Refs. 57 and 58. One popular QCF is the harmonic QCF, given by[56]

$$Q^H(\omega) = \frac{\beta\hbar\omega}{1 - e^{-\beta\hbar\omega}}. \tag{2.19}$$

The harmonic QCF is exact for harmonic systems in some cases (e.g., the observable in TCF is a linear function of position and momentum operators),[57–59] and also satisfies the fluctuation-dissipation theorem in the linear response theory.[60]

2.5 High-Frequency Vibrational Spectroscopy: OH (OD) Stretch

For the high-frequency OH (OD) stretch, most classical simulations work very poorly (even with the application of QCFs) except for those water models parametrized from vibrational spectroscopy.[61–64] Expensive quantum MD simulations could reproduce experimental OH (OD)

stretch IR spectra well if a good water model is used, in which the intramolecular potential for OH (OD) stretch has to capture the huge anharmonicity of OH (OD) stretch in condensed phases.[47,65,66] Also note that the ring-polymer MD (a popular quantum simulation method) could suffer from its high-frequency problem so that one should be cautious to use it directly to model OH (OD) vibrational spectroscopy.[47,67] A popular approach for modeling high-frequency vibrational spectroscopy is to use semi-classical methods.[41,68–75] In particular, the Skinner group has developed a reliable mixed quantum/classical approach,[23] which will be reviewed briefly in this section.

The starting equation here is Eq. (2.9). Note that the equation of motion for the time evolution opertor $U_I(t)$ in the interaction picture is

$$i\dot{U}_I(t) = e^{iI_S\otimes H_0 t}\left(\sum_i (H_i - H_0)\left|i\right\rangle\left\langle i\right| + \sum_{i\neq j} H_{ij}\left|i\right\rangle\left\langle j\right|\right) e^{-iI_S\otimes H_0 t}U_I(t). \tag{2.20}$$

We further define $\omega_i(t) \equiv e^{iI_S\otimes H_0 t}(H_i - H_0)e^{-iI_S\otimes H_0 t}$, and $\omega_{ij}(t) \equiv e^{iI_S\otimes H_0 t}H_{ij}e^{-iI_S\otimes H_0 t}$. Then, Eq. (2.20) can be written as

$$i\dot{U}(t) = \tilde{H}(t)U(t), \tag{2.21}$$

where subscript I for the interaction picture is omitted (and will be omitted henceforth for simplicity), and $\tilde{H}(t)$ is defined as

$$\tilde{H}(t) = \sum_i \omega_i(t)\left|i\right\rangle\left\langle i\right| + \sum_{i\neq j}\omega_{ij}(t)\left|i\right\rangle\left\langle j\right|. \tag{2.22}$$

$\tilde{H}(t)$ is sometimes called Frenkel exciton Hamiltonian, and its matrix element in the local mode basis is $\kappa_{ij}(t) \equiv \left\langle i\right|\tilde{H}(t)\left|j\right\rangle = \omega_i(t)\delta_{ij} + \omega_{ij}(t)(1-\delta_{ij})$. $\omega_i(t)$ is fluctuating transition frequency of ith OH chromophore, $\omega_{ij}(t)$is fluctuating vibrational coupling between ith and jth OH chromophores, and both are bath operators in our treatment.

2.5.1 Mixed Quantum/Classical Approach

The key step in the mixed quantum/classical (Q/C) approach is to assume the bath degrees of freedom (i.e., intermolecular translations and rotations) are classical; therefore, the bath oper-

ators (e.g., $\omega_i(t)$, $\omega_{ij}(t)$, $A_{0i}(t)$, $B_{j0}(0)$) are classical variables (we use "variable" rather than "observable" because if we take IR as an example, the total dipole operator is Hermitian, but the transition dipole bath operator is not necessarily Hermitian, and we have to assume it is.). Note that the evaluation of these transition variables still requires quantum mechanics, and will be addressed in the next subsection. As mentioned in the Section 2.2, one important piece is still missing — vibrational energy relaxation, which will be introduced phenomenologically.[41,76] Finally, we reach a useful expression for the TCF related to the OH (OD) stretch spectroscopy:

$$C_{AB}^{h}(t) = \sum_{ij} \langle A_{0i}(t) U_{ij}(t) B_{j0}(0) \rangle_b \, e^{-|t|/2T_1}, \tag{2.23}$$

where T_1 is the vibrational relaxation lifetime (usually taken from experiment), and $U_{ij}(t)$ is determined by Eq. (2.21) with initial condition $U_{ij}(0) = \delta_{ij}$. In practice, one usually only considers positive time, and performs a half Fourier transform to obtain the spectrum of interest, as the expression in Fourier transform can be converted to that in half Fourier transform using the symmetry properties of a quantum TCF. When isotopic dilution is used (e.g., dilute HOD in D_2O), there is essentially only one chromophore in the system (no vibrational coupling), and $U_{ij}(t) = \delta_{ij}\text{exp}[-i\int_0^t \omega_i(\tau)d\tau]$ for positive t.

2.5.2 Implementation of Mixed Quantum/Classical Approach

In principle, the transition variables in Eq. (2.23) are functions of all the bath degrees of freedom, and could be calculated on-the-fly during simulations. However, such a calculation is usually too expensive for condensed phases. Another strategy is to find few collective coordinates, which are highly correlated with the transition variables and are also easy to calculate during the simulation.[77] One can then parametrize this correlation ("map") prior to the simulation, and apply the map on-the-fly to calculate line shapes. Previous studies in the Skinner group showed that the classical electric field on hydrogen along the OH bond direction (E_i) is a good collective coordinate for OH stretch,[75] and maps for all the transition variables have been developed. In Table 2.2, a set of maps which are used in Chapters 4 - 6 for TIP4P-like water models are shown (for Chapter 7, a different set of maps is used after a reparametrization described in Ref. 78). For instance, the key steps of the parametrization of the map for transition frequency ω_i are as follows: a one-dimensional (1D) stretch PES of a given OH chromophore

is calculated using a DFT method in the presence of surrounding water molecules (nearby ones are also treated explicitly by DFT, and distant ones are included as point charges in the DFT calculation); then the resulting 1D vibrational Schrodinger equation is solved numerically by a method called discrete variable representation.[79] Therefore, the transition frequency map captures many important charateristics of the OH stretch in condensed phases — large anharmonicity, high sensitivity to its hydrogen bonding condition (many-body effect), and nuclear quantum effects. These maps turn out to be reasonally accurate and very efficient, and their performance has recently been evaluated systematically against DFT calculations.[78] Note that the maps are dependent on the water models used, as snapshots from MD simulations were used as sample configurations for map parametrization.

OH frequency, coordinate, and momentum maps
$\omega_{01} = 3732.9 - 3519.8E - 153520E^2$
$\omega_{12} = 3606.0 - 3498.6E - 198715E^2$
$x_{01} = 0.19318 - 1.7248 \times 10^{-5}\omega_{01}$
$x_{12} = 0.26836 - 2.3788 \times 10^{-5}\omega_{12}$
$p_{01} = 1.6102 + 5.8697 \times 10^{-4}\omega_{01}$
$p_{12} = 2.0160 + 8.7684 \times 10^{-4}\omega_{12}$
OD frequency, coordinate, and momentum maps
$\omega_{01} = 2748.2 - 2572.2E - 102980E^2$
$\omega_{12} = 2673.0 - 1763.5E - 138534E^2$
$x_{01} = 0.16598 - 2.0752 \times 10^{-5}\omega_{01}$
$x_{12} = 0.23167 - 2.8596 \times 10^{-1}\omega_{12}$
$p_{01} = 1.9813 + 9.1419 \times 10^{-4}\omega_{01}$
$p_{12} = 2.6233 + 13.1443 \times 10^{-4}\omega_{12}$
dipole derivative and intramolecular coordinate coupling constant map
$\mu' = 0.1646 + 11.39E + 63.41E^2$
$k_{ij}^a = -1361 + 27165(E_i + E_j)$

Table 2.2: Spectroscopic maps for TIP4P-like water models.[35,78,80–82] ω_{01}, x_{01} and p_{01} are transition frequency, coordinate and momentum matrix elements for the 0-1 vibrational transition, respectively. Likewise, the quantities with the subscript 12 are for the 1-2 transition. μ' is the

dipole derivative, and k_{ij}^{a} is the intramolecular coordinate coupling constant. E is the classical electric field on water hydrogen along the OH (OD) bond direction from all other molecules within a cutoff of 7.831 Å. The position of the transition dipole is 0.67 Å away from the water oxygen along the OH (OD) bond. Regarding the polarizability for Raman, see Ref. 35.

2.6 Describing the Bath: E3B Water Model

The success of the calculations described in the previous section relies on how well the bath is described: a good classical rigid water model is needed. Throughout this thesis, we use the explicit three-body (E3B) water model,[83,84] developed in the Skinner group (for Chapters 3 - 6, the second version[84] is used, and for Chapter 7, the third version[85] is used.). The E3B model has been proven accurate and versatile in describing water properly in various molecular environments (e.g., liquid water,[86] ice Ih,[35,80,81] air/water interface,[87–89] hexamer[90] and amorphous ices[91]). Specifically for ice Ih, it can describe low-frequency vibrational dynamics fairly well. This is the topic of the next chapter.

Chapter 3

Dipole Fluctuations: Static Dielectric Constant and Low-Frequency IR

Contents

Most of the content of this chapter is drawn from a manuscript in prepartion with Yicun Ni, Samuel Drews and James Skinner. We thank Prof. David Eisenberg for pointing out Ref. 92, Prof. Marivi Fernández-Serra for explaining their results on ice Ih, Dr. Fu Li and Shushan He for discussions on the IINS for ice Ih, Dr. Craig J. Tainter for helping with the E3B simulations, and Zachary Kann for discussions on dielectrics.

3.1 Introduction

As mentioned in section 1.2, ice Ih has an unusually large static dielectric constant ε (130 at 200 K[22]) due to the proton disorder (the subscript s is dropped from ε_s for notational simplicity in this chapter). In fact, liquid water also has a fairly large static dielectric constant (about 78.5 at

298 K[93]), and even more interestingly the static dielectric constants for ice Ih and liquid water near the melting point are quite close (ice has slightly larger ε). However, these experimental observations have provided a challenge for rigid non-polarizable water models ("rigid" means that the intramolecular degrees of freedom are frozen, and "non-polarizable" means that the charge distribution in the water molecule is fixed, independent of its local environment). In Fig. 3.1, the calculated ε for liquid water and ice Ih with some common non-polarizable rigid water models (symbols) are shown, along with experimental values (solid lines). It is clear that all of these models significantly underestimate ε for ice Ih, and even worse, incorrectly predict that the static dielectric constant of ice Ih is lower than that of liquid water near the melting point (the dashed line).[50,55,94–96] The failure to reproduce ε is also related to another shortcoming of rigid non-polarizable models:[97] they fail to reproduce the hydrogen-bond stretch peak (around 200 cm^{-1}) in the low-frequency IR spectra for ice Ih[32,98] and liquid water.[99–103] This is not surprising at all since both properties are related to the low-frequency part of total dipole TCF, discussed in Sections 2.3 and 2.4. In this chapter, both ice Ih and liquid water are considered as these two issues exist for both systems, but the focus will be ice Ih.

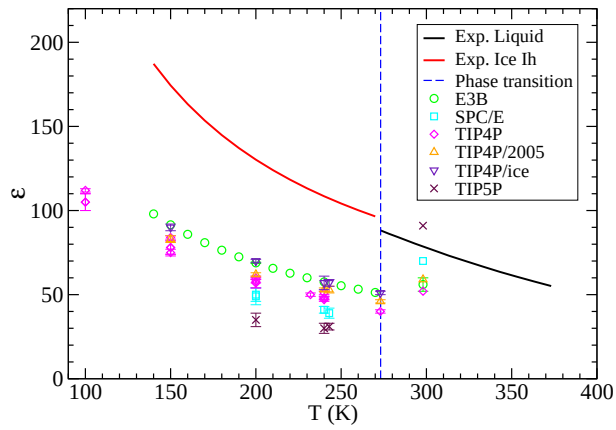

Figure 3.1: Experimental static dielectric constants of liquid water and ice Ih (solid lines), and calculated results from some rigid non-polarizable water models (symbols).

One attempt to solve these problems is to make the water molecule flexible, which introduces the intramolecular degrees of freedom (i.e., OH stretches and HOH bend) into the molec-

ular dynamics (MD) simulations. However, it seems that little success has been achieved in this direction: TIP4P/2005f, a flexible non-polarizable model based on TIP4P/2005, gives quite a similar ε for liquid water to that from TIP4P/2005;[104] the low-frequency IR spectrum calculated with a flexible SPC model developed by Praprotnik and coworkers still misses the peak at 200 cm^{-1};[105] and although the flexible model SPC/Fw[106] can reproduce ε fairly well for the liquid water and supercritical water,[107] it still underestimates ε for ice Ih significantly ($\varepsilon = 60$ at 240 K for this model)[96] and fails to reproduce the 200 cm^{-1} peak for liquid water.[64] Another approach is to make the water molecule polarizable, allowing the charge distribution of water molecules to be influenced by their local environments. There are many approaches for implementing the polarization effect, such as the fluctuating charge method, the Drude oscillator model, and the point dipole interaction model.[108–113] This direction seems very promising: rigid polarizable TIP4P-FQ model reproduces ε for both liquid water and ice Ih very well, and some flexible polarizable water models (such as the *ab initio* based TTM3-F model,[61,65,114] the POLI2VS model,[115] and the iAMOEBA model[64]) generate the peak at about 200 cm^{-1} in the IR spectrum for liquid water. Furthermore, as computing power steadily increases, it is becoming affordable to simulate the structure and even the molecular dynamics of water on-the-fly with electronic structure methods.[116–123] Car and his coworkers showed that ε for liquid water from Car-Parrinello molecular dynamics (CPMD) is in good agreement with experiment,[121] and the low-frequency IR spectra for deuterated liquid water and ice Ih from CPMD show peaks around 200 cm^{-1},[119,122] though the overall lineshapes are somewhat different from the experiment. From all the above theoretical efforts on modeling ε and the low-frequency IR for liquid water and ice Ih, it is clear that the inclusion of the polarization effect in the water model is essential for calculating these properties with a greater degree of accuracy.

Despite the success of some polarizable water models and electronic structure methods (e.g., CPMD) mentioned above, they are usually much more computationally expensive than the rigid non-polarizable water models. Another concern with these advanced models is that their overall performance in modeling water is rarely benchmarked systematically against various properties of liquid water and ice, whereas many rigid non-polarizable water models have been assessed extensively.[124] Therefore, it may be useful to incorporate polarization effects into well-benchmarked rigid non-polarizable models without modifying their simple interaction potentials. One straightfoward approach is to scale the molecular dipole associated with the model

during post-simulation analysis,[125] and Vega and coworkers pointed out that a simple scaling factor can get ε in qualitative agreement with experiment for several different ice phases (although a different scaling factor is needed for liquid water).[55] However, scaling the molecular dipole uniformly does not help the low-frequency IR spectrum. It is also worth mentioning that the fluctuating charge model TIP4P-FQ does not introduce any additional intermolecular interactions beyond those already in TIP4P, though it does require re-parametrization of TIP4P and has its dipole polarizability only in the plane of water molecule, which is quite unphysical.[110] Another strategy is to find a collective variable to correlate with the polarization effect on the dipole surface, but keep the form of intermolecular potential in the rigid non-polarizable model, as the polarization effect on the potential energy surface has already been implicitly taken into account during model parametrization, especially for empirical water models. This final strategy is chosen in this chapter. In principle, the dipole surface depends on all the electronic and nuclear degrees of freedom in the system. If we assign a molecular dipole to each molecule in the system, we can imagine the molecular dipole to consist of a permanent dipole from the rigid non-polarizable model and an induced dipole generated by its environment. Therefore, our goal is to find a collective variable to correlate with the molecular induced dipole. A natural choice for this variable is the electric field on the water molecule from the classical electrostatic perspective.

The first step in applying this strategy is to choose a good rigid, non-polarizable water model for the molecular simulations; here, we choose the second version of the explicit three-body (E3B) water model,[84] mentioned in Section 2.6. The model utilizes TIP4P as a reference potential and includes a two-body correction and three-body interactions, the functional forms of which are based on electronic structure calculations. The parameters in the potential are empirically fit to six experimental properties of water. It has been shown that the overall performance of the E3B model in reproducing various properties of liquid water and ice is generally better than the commonly used SPC/E and TIP4P models.[84] For instance, the melting temperature, ice density, second and third virial coefficients, and some dynamical properties (diffusion coefficient and H–H rotational correlation time) from the E3B model are in better agreement with experiment. It is also worth pointing out the connection and differences between the E3B model and conventional polarizable models: the intermolecular potential energy of the whole system is a sum of many-body interactions, and the E3B model is essentially an analytic potential fitting

to the first two terms (i.e., two-body and three-body terms) in the many-body expansion; the treatment of the polarization effect on the intermolecular interaction in most polarizable models is an approximate way to account for the many-body interactions beyond the two-body term. However, as the charge distribution in E3B water is still fixed as that in TIP4P, the polarization effect on the dipole surface is still missing in the E3B model. As a result, ε calculated from the E3B model is about 56 for liquid water at 298 K, close to 52 from TIP4P and much lower than the experimental value of 78.5.[84] Nevertheless, the E3B model provides a reliable potential for modeling water in its condensed phases, and we would like to introduce the polarization effect on the dipole surface into the E3B model by using the strategy described in the previous paragraph, and resolve the two aforementioned issues for the E3B model.

The rest of the chapter is organized as follows. In Section 3.2, we outline the method for generating ice Ih configurations and describe the details of the MD simulations; in Section 3.3, the parametrization is performed, and the calculated static dielectric constants are compared to experiment; in Section 3.4, we calculate and analyze the low-frequency IR spectra; and in Section 3.5 we conclude.

3.2 Generating Ice Ih Configurations

For the ice simulation, we need to sample over many proton-disordered configurations before running conventional MD simulations as MD simulation is not able to reorient the water molecules at the expense of overcoming large energy barriers between different proton-disordered configurations. There are many algorithms available in the literature.[95,96,126–128] In the present work, we used the algorithm proposed by Buch and coworkers,[127] and modified it to work with the geometry of the E3B (TIP4P) water molecule. We started with setting up a hexagonal lattice for oxygen atoms to match the experimental lattice constants (i.e., a, b and c) at one given temperature; the size of the lattice is $6a \times 3b \times 3c$, giving 432 H_2O molecules in the simulation box.[7,126] Then Buch's algorithm was utilized to generate ice Ih configurations subject to the Bernal-Fowler ice rule[11] using a simple topological Monte-Carlo scheme.[127] Note that the HOH angle of the water molecule in the algorithm is about 109.5°, whereas the value for the E3B model is 104.5°. We adjusted the bond angle to that of the model (i.e., 104.5°) such that the direction of the permanent molecular dipole (i.e., molecular bisector) is unchanged. This

approach for generating proton-disordered configurations has been used recently by Vega and coworkers,[55] who termed it the Pauling model. For calculations of ε, we generated 5000 proton-disordered configurations using the Pauling model, and calculated ε directly using these "static" configurations without running further MD simulations. The rationale for this approach will be explained in Section 3.3. For the calculation of the low-frequency IR spectrum at one given temperature, further MD simulations were performed for 20 proton-disordered configurations randomly picked from those 5000 using a modified version of GROMACS 3.3.[129] The Berendsen thermostat with a coupling constant of 0.5 ps was employed to control the temperature of the NVT-ensemble simulation in the production run.[130] The SETTLE algorithm was used to hold the water molecules rigid.[131] Periodic boundary conditions (PBC) were applied with the particle-mesh Ewald (PME) method for the electrostatic interactions.[132,133] In the production run, a trajectory of 1 ns was saved every 4 fs for each configuration.

3.3 Static Dielectric Constant

The formula for the calculation of static dielectric constant is Eq. (2.16) (note that the ice sample in Ref. 22 was polycrystalline ice). As we discussed earlier, if we can assign a molecular dipole to each water molecule (this assignment has some ambiguities from the point of electronic structure theory), we can write the total dipole of the system as a sum of molecular dipoles

$$\vec{M} = \sum_i \vec{\mu}_i, \tag{3.1}$$

where $\vec{\mu}_i$ is the molecular dipole of ith molecule. Also mentioned earlier, in order to implement the polarization effect on the dipole surface in our model, we would like to write the molecular dipole of ith molecule $\vec{\mu}_i$ as the sum of the molecular permanent dipole $\vec{\mu}_i^{per}$ associated with the model and the molecular induced dipole $\vec{\mu}_i^{ind}$: $\vec{\mu}_i = \vec{\mu}_i^{per} + \vec{\mu}_i^{ind}$. Consequently, we have the total dipole of the system as

$$\vec{M} = \vec{M}^{per} + \vec{M}^{ind}, \tag{3.2}$$

where $\vec{M}^{per}$ and $\vec{M}^{ind}$ are the permanent and induced components of the total dipole, respectively.

The goal of the present work is to come up with a practical way to calculate $\vec{\mu}_i^{ind}$ from MD

simulations. In this work, we correlate $\vec{\mu}_i^{ind}$ with the classical electric field on the oxygen atom of the ith molecule $\vec{E}_i$ from all the water molecules within 7.831 Å of the ith molecule based on the oxygen-oxygen distance. The cutoff of 7.831 Å is chosen for historical reasons,[35,78,134] but we verified that larger cutoffs do not change our results in the parametrization. For the sake of simplicity and for some physical reasons explained later, the correlation is chosen to be linear

$$\vec{\mu}_i^{ind} = \gamma \vec{E}_i, \tag{3.3}$$

where γ is parametrized below. Note that although γ resembles the conventional dipole polarizability, it should be regarded as a parameter for the most part as we do not calculate the induced dipole in a self-consistent manner, as many polarizable models do. We will call Eq. (3.3) a map between $\vec{\mu}_i^{ind}$ and $\vec{E}_i$. Note that we also tried other parametrization schemes (e.g., using the electric field on oxygen atom along the bisector of the water molecule as the collective coordinate), but this seems to be of the simplest form that gives reasonable agreement with experiment.

For the calculation of ε for ice Ih, we have to sample many proton-disordered configurations first. For this purpose, the Pauling model was used to generate 5000 configurations as described in the previous section. We used these configurations directly (without further MD simulations) to calculate $\langle M^2 \rangle$, and fit ε to the experimental value of 130 at 200 K for ice Ih. The optimal γ from this is 2.300 Å^3 (we are using cgs units here), giving a calculated ε of 130.3$\pm$0.8 at 200 K. Note that the same strategy was also applied to liquid water (though one configuration with a long enough MD simulation is sufficient for liquid water), and we obtained a γ of 1.495 Å^3 by fitting it against the experimental ε of 76.75 at 303 K.[93] The reason why we get a different γ for liquid water from that for ice Ih is that the electronic structures are different in these two phases, and rigid non-polarizable models do not capture this. As the polarization effect is mainly an electronic structure effect, we need different mapping parameters (γ) to incorporate it into the non-polarizable model. A further point is that the molecular geometry (nuclear charge distribution) is changed slightly from liquid water to ice Ih.[135–139] This treatment is also consistent with the observation by Vega and coworkers that different scaled molecular dipoles for liquid water and ice Ih are required in order to match the experiment values of ε.[55] With $\gamma = 2.300$ Å^3, we calculated ε as a function of temperature from 140 K to 270 K for ice Ih, and the results are plotted as green circles on the left side of the blue, dashed line (which indicates

the melting point) in Fig. 3.2. Note that for the volume of the system in the calculation of ε from Eq. (2.16), we used the simulation box size at 200 K. The density of ice changes slightly from 140 K to 270 K,[7] but we verified that this density effect has little effect on the results of ε. Surprisingly, the agreement between theory and experiment is excellent over a wide temperature range considering the simplicity of our model. In Fig. 3.2 the calculated static dielectric constants for liquid water at different temperatures based on the same parametrization scheme are also shown as green circles on the right side of the blue dashed line. Moreover, the model correctly captures the difference of ε for liquid water and ice Ih around the melting temperature.

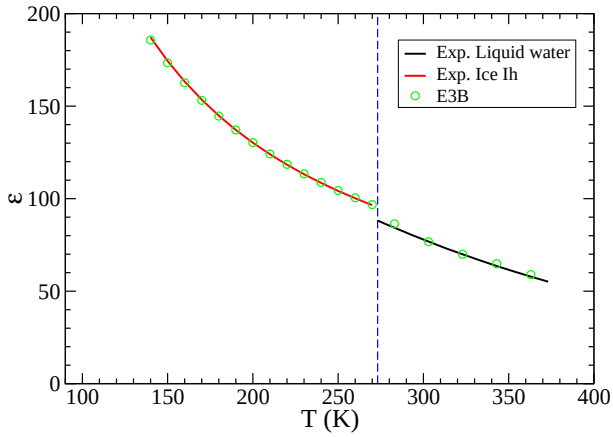

Figure 3.2: Calculated and experimental[22,93] dielectric constant of liquid water and ice Ih as a function of temperature. The blue dashed line indicates the melting temperature of ice Ih.

Despite the success of our model in reproducing ε for ice Ih in a wide range of temperatures, it is worth discussing the implications and errors in our model. The Pauling model (Buch's algorithm) is based on a topological Monte-Carlo scheme, and we did not perform MD simulation for the proton-disordered configurations. As a result, our model does not include energy or temperature effects. The fact that the temperature dependence of our calculated ε is in excellent agreement with experiment implies that the temperature dependence of ε for ice Ih is simply due to the trivial $1/T$ factor (in β) in Eq. (2.16). In other words, $\langle M^2 \rangle$ is more or less temperature-independent. In addition, the Pauling model assumes that each proton-disordered

configuration is equally probable, and from our results it seems that this assumption is fairly good for most relevant temperatures. Indeed, we find that the energy difference between these configurations with the E3B potential is much smaller than the thermal energy at most temperatures (less that 1% at 200 K). This is also found by others,[55,96] though the energy difference between different configurations with MD simulations is larger in their studies. We estimate the error with our model in calculating ε by implementing the algorithm proposed by Lindberg and Wang[96] and running MD simulations after the configurations are generated. We find that our model overestimates ε by about 12% at 100 K when γ is set to zero. Similar errors are also found in the calculations of Vega and coworkers with the Pauling model and TIP4P/2005 potential.[55] Even though this error is not negligible, and running MD simulations with more advanced algorithms could give a different optimal γ during our parametrization, we think it is more important to taken into account polarization effects, the biggest missing piece in the non-polarization model. The apparent advantage of the Pauling model is its simplicity, and as we will show later, our simple model reproduces the low-frequency IR for ice Ih fairly well.

Besides the static dielectric constant, researchers are also interested in the magnitude of the molecular dipoles in condensed phases of water. The molecular dipole of an isolated water molecule is about 1.85 D,[140] and is believed to increase significantly in liquid water and ice. Experiments suggest that the molecular dipole in liquid water is about 2.9-3.0 D.[141,142] The values from theoretical calculations vary greatly, 2.4 – 3.1 D for liquid water,[64,110,111,121,143–161] and 2.3 – 3.7 D for ice Ih,[16,64,92,111,121,143,160,162–169] depending on the methods and the partitioning of the charge density. We calculated the distribution of the molecular dipole in our model for ice Ih at 245 K from MD simulations, shown in the panel (a) of Fig. 3.3. The average value from the distribution is 3.56 D for ice Ih, greater than most theoretical estimates. Another interesting property to examine is the angle between the molecular permanent and induced dipoles, the distribution of which for ice Ih is shown in the panel (b) of Fig. 3.3. We find that for most water molecules, the induced dipole is aligned with its permanent dipole (i.e., the bisector of the molecule) to some extent. This is mainly due to the tetrahedral coordination of water molecules in ice Ih. Moreover, this interesting observation provides a possible physical interpretation for our empirical mapping parameter γ. In the seminal paper by Coulson and Eisenberg in 1966, they investigated the dipole moment of a water molecule in ice Ih using a purely electrostatic method.[92] They argued that if the induced dipole is along the direction of the permanent dipole

(with an isotropic dipole polarizability), the self-consistent treatment of the induced dipole can be simplified to a sum of a geometric series, leading to a closed-form expression for the molecular dipole (Eq. (7) in Ref. 92). In this sense, our parameter γ (at least for ice Ih) is an effective polarizability that has already taken into account the effect of the self-consistent treatment. This also explains why we do not need to calculate the induced dipole self-consistently as most polarizable models do. In fact, the parameter γ estimated from their model is close to our value of 2.300 Å^3 for ice Ih. The analysis was also performed for liquid water, and the results are also shown in Fig. 3.3: the calculated average molecular dipole in water is 2.96 D for liquid water, in a good agreement with experiment,[141,142] and the molecular induced dipole is also aligned with the molecular permanent dipole to some extent.

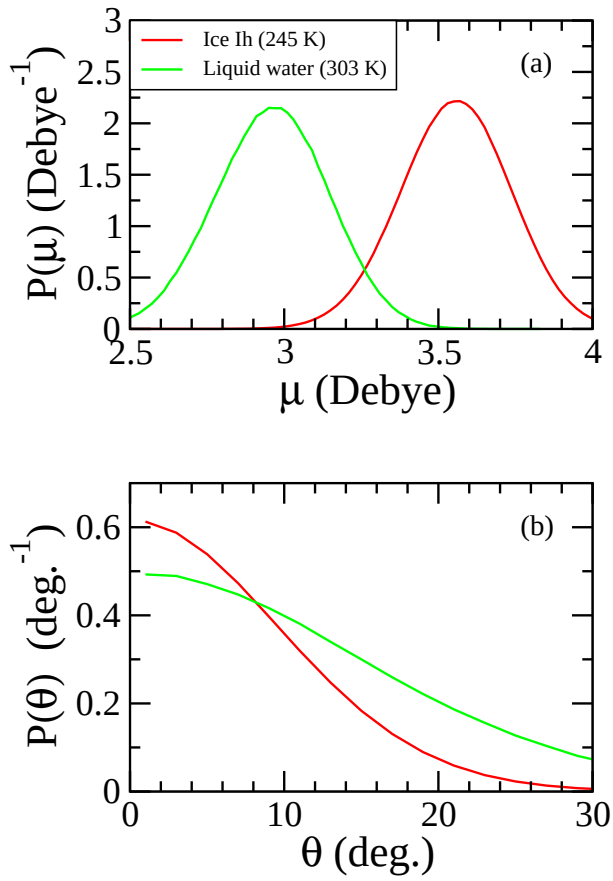

Figure 3.3: Probability distribution functions of (a) molecular dipole and (b) the angle between the molecular permanent dipole and induced dipole for liquid water at 303 K (green line) and

ice Ih at 245 K (red line) from molecular dynamics simulations. Note that $P(\theta)$ satisfies the normalization condition $\int_0^{180^\circ} P(\theta)\sin\theta d\theta = 1$.

3.4 Low-Frequency Infrared Spectra

In this section, we attempt to use the γ parametrized in the previous section to reproduce the peak around 200 cm^{-1} in the low-frequency IR spectrum of ice Ih. Using the Fourier transform of Eq. (2.8) as $I^{cl}(\omega)$ and harmonic QCF (Eq. (2.19)) as $Q(\omega)$ in Eq. (2.18), we obtain the final expression for the low-frequency IR spectrum

$$S(\omega) \equiv \alpha(\omega)n(\omega) = \frac{2\pi\omega^2}{3ck_BTV}\int_{-\infty}^{\infty} dt\, e^{i\omega t}\langle \vec{M}(t)\cdot\vec{M}(0)\rangle, \tag{3.4}$$

where $\alpha(\omega)$ is the absorption coefficient, $n(\omega)$ is the frequency-dependent refractive index, $\alpha(\omega)n(\omega)$ is often reported for low-frequency IR spectra, c is the speed of light, the brackets indicate a classical ensemble average over the bath (subscript b is omitted), the subscript 00 is also dropped from $\vec{M}_{00}$ in Eq. (2.8), and the relation $4\pi^2\omega(1-e^{-\beta\hbar\omega})I(\omega) = 3\hbar cn(\omega)\alpha(\omega)V$ is used to convert $I(\omega)$ to $n(\omega)\alpha(\omega)$.[37] Note that for ice Ih, the ensemble average includes the average over different proton-disordered configurations (20 in our calculations). For the ice configuration with a non-zero total dipole, one needs to subtract $\langle\vec{M}\rangle\cdot\langle\vec{M}\rangle$ from $\langle\vec{M}(t)\cdot\vec{M}(0)\rangle$ before performing the Fourier transform in order to avoid singularity at zero frequency. We have verified that the IR spectra are converged for the simulation boxes used here (432 molecules for ice Ih).

In Fig. 3.4, we show the calculated IR spectra (red lines) for ice Ih at 100 K (top panel) and 245 K (middle panel), in good agreement with the experimental spectra (black lines) at 100 K[98] and 266 K,[32] respectively. The reason why we choose 245 K is that the melting temperature of the E3B model is 251 K.[84] The experimental IR spectrum at 266 K (100 K) shows three main peaks at 148 (160) cm^{-1}, 208 (225) cm^{-1} and 800 (850) cm^{-1}, as well as a small shoulder on the red side of the second peak. The experimental spectrum at 266 K also shows some features around 500 and 600 cm^{-1}, which are not seen in the spectrum at 100 K due to its low resolution. The peaks below 400 cm^{-1} can be assigned to the oxygen lattice modes (phonons),

while the peak around 800 cm^{-1} is the librational mode.[170] Our calculation at 100 K (245 K) reproduces these peaks at about 170 (187) cm^{-1}, 246 (266) cm^{-1} and 755 (809) cm^{-1}, and even the slight shoulder on the red side of the second peak. The peak positions are slightly shifted compared to the experiment: the peaks of lattice modes are shifted to blue by about 25 cm^{-1} and 40 cm^{-1}, respectively, and the librational peak is shifted to red by about 50 cm^{-1}. This is primarily due to inaccuracies in the E3B potential. The relative peak intensity between the lattice and librational modes in our calculated spectra is also in good agreement with experiment (the intensity of lattice modes is slightly too high). Moreover, the temperature dependence of the peak positions for the calculated spectra is also consistent with the experimental trend (a blue-shift as the temperature decreases). In fact, this temperature-dependence is primarily due to the fact that ice Ih has a larger density at lower temperature.[7,171] Furthermore, we set γ to zero for ice Ih (green line), we find that the lattice modes in ice Ih become almost IR-inactive. Therefore, the polarization effect is responsible for the intensity below 400 cm^{-1}, which is associated with the hydrogen bond (HB) stretching mode (note that this interpretation focuses on the local water dimer in ice Ih, while "lattice mode" or "phonon" adopts a global view).[172–174] If the model is non-polarizable, the total dipole of the system does not change much during the HB stretching so that little intensity is observed for this mode (green line). However, if the model includes polarization effects, the molecular induced dipole will change significantly because HB stretching changes the distance between the hydrogen-bonded molecules. Thus, it is essential to include the polarization effect to make the HB stretching mode bright in the IR spectrum. On the other hand, the librational mode, carrying the rotational characteristics, gives rise to total dipole fluctuations even for the non-polarizable model (green line). Another important observation to mention is that the low-frequency IR spectra for ice Ih calculated from different proton-disordered configurations are quite similar, though these configurations have quite different total dipoles.

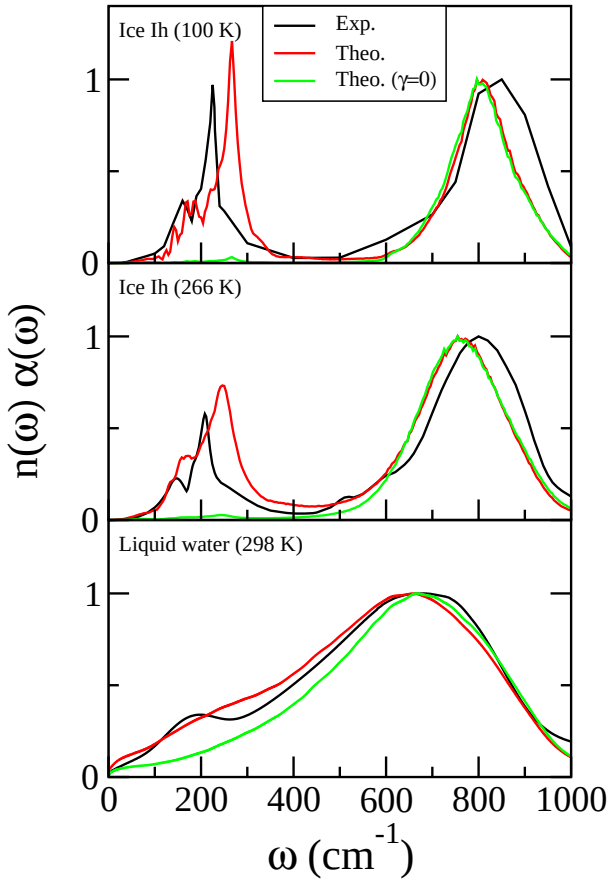

Figure 3.4: Experimental (black lines) and calculated (red lines) low-frequency infrared spectra for liquid water and ice Ih. The experimental spectra, from top to bottom, are at 100 K,[98] 266 K[32] and 298 K,[103] respectively. The calculated spectra, from top to bottom, are at 100 K, 245 K and 303 K, respectively. The green lines are the infrared spectra, calculated with γ set to zero.

It is surprising even to us that such a simple model with an empirical γ can reproduce the low-frequency IR spectra for ice Ih fairly well. Therefore, we would like to understand the effect of polarization on the IR spectrum further by decomposing the spectrum based on Eq. (3.2). The spectrum can be modeled as of three parts, shown in Fig. 3.5: spectrum from the permanent-permanent correlation $S^{pp}(\omega)$ (red line), from the induced-induced correlation $S^{ii}(\omega)$ (green line), and from the permanent-induced cross correlation $S^{pi}(\omega)$ (blue line). It is clear that $S^{ii}(\omega)$ and $S^{pi}(\omega)$ are responsible for the enhancement of the intensity of the lattice modes,

but most importantly $S^{pi}(\omega)$ attenuates the intensity of the librational mode significantly. The physical reason for this is easy to understand in ice Ih, and herein we will consider a hydrogen-bonded water pair in the ice crystal: when the H-bond donor water molecule in the dimer librates slightly away from its equilibrium position, the hydrogen atom originally involved in the H-bond gets farther away from the oxygen atom of the H-bond acceptor water molecule, leading to a smaller induced dipole of the H-bond acceptor; meanwhile, this rotation in most cases makes the alignments of the two molecules better, leading to an increase of the total permanent dipole. This anti-correlation gives rise to the negative intensity for the librational mode in $S^{pi}(\omega)$. A similar result was also observed by Saito and coworkers using their TTM3-F model,[175] while Hasegawa and Tanimura did not observe this in their spectral decomposition.[115]

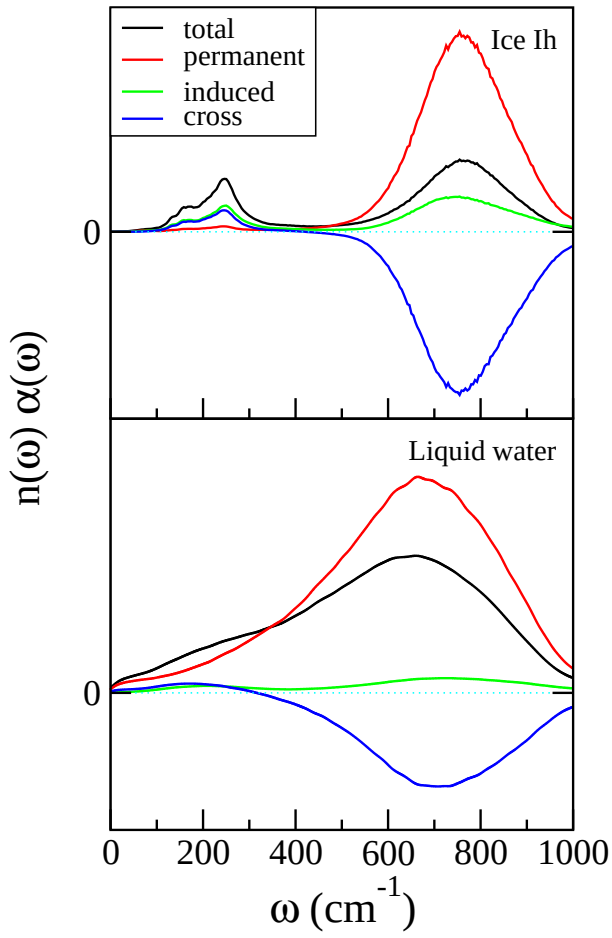

Figure 3.5: Decomposition of the calculated low-frequency infrared spectra (black lines) for ice Ih at 245 K (top panel) and liquid water at 303 K (bottom panel) into permanent-permanent terms (red lines), induced-induced terms (green lines) and permanent-induced cross terms (blue lines).

Lastly, we would like to discuss the assignment of the peaks in the IR spectra further. Based on the relation that $\langle \vec{M}(t) \cdot \vec{M}(0) \rangle = \sum_{ij} \langle \vec{\mu}_i(t) \cdot \vec{\mu}_j(0) \rangle$, we can decompose the IR spectrum $S(\omega)$ to the contribution from the single-particle correlation $S^s(\omega)$ ($i = j$ terms), and the contribution from the intermolecular cross correlation $S^c(\omega)$ ($i \neq j$ terms). Another important single-particle correlation function is the velocity time correlation function $C_{vv}(t) = \langle \vec{v}(t) \cdot \vec{v}(0) \rangle$, and its Fourier transform $f(\omega)$ is proportional to the phonon density of states for a harmonic system,[37] which in principle can be probed by the inelastic incoherent neutron scattering (IINS). Note that we are considering the classical hydrogen velocity $\vec{v}$ here, and do not apply the harmonic quantum correction factor for $f(\omega)$. In Fig. 3.6, we plot $S(\omega)$ (black line), $S^s(\omega)$ (red line), $S^c(\omega)$ (green line) and $f(\omega)$ (blue line) for ice Ih at 245 K. For ice Ih, there are four peaks/shoulders in the lattice-mode region of the calculated $f(\omega)$ for ice Ih, which are also observed in the experimental IINS,[173,176] indicating that the E3B model is reliable in describing the phonons in ice Ih, even though the peak positions are slightly shifted, explaining the discrepancy in the peak positions in the IR spectrum. The assignments of these four peaks are available in the literature,[172–174] though new ideas have also been forwarded recently.[117,177,178] We tentatively take the simple assignments made by Prask and coworkers:[172] the four peaks, from low to high frequency, are from TA, LA, LO and TO lattice modes, respectively (T, L, A and O stand for transverse, longitudinal, acoustic and optic, respectively), though other mechanisms might be also involved (e.g., LO-TO splitting and proton disorder[117,174]). In the librational region, $f(\omega)$ shows three peaks/shoulders at 245 K. The calculated $f(\omega)$ at 15 K, meanwhile, shows four peaks/shoulders, consistent with the experimental IINS at 15 K.[176] Since $S^s(\omega)$ and $f(\omega)$ are both calculated from single-particle correlation, $S^s(\omega)$ shows similar spectral features to $f(\omega)$, though the peak intensities are different. With the inclusion of the intermolecular cross correlation contribution $S^c(\omega)$, the TA peak in the translational region, and the first and third librational peaks in $S^s(\omega)$ are largely attenuated, while the LA and LO peaks get further en-

hanced. This leaves the two phonon peaks (LA and LO) and the second librational peak visible in the IR spectrum, reflecting the effects of the IR selection rules.

The low-frequency IR spectrum for liquid water was also calculated (panel (c) of Fig. 3.4), the same analysis was performed, and the results are presented in Figs. 3.5 and 3.6. The agreement between experiment and theory for liquid water is not as good as for ice Ih, but the overall physical picture is similar.

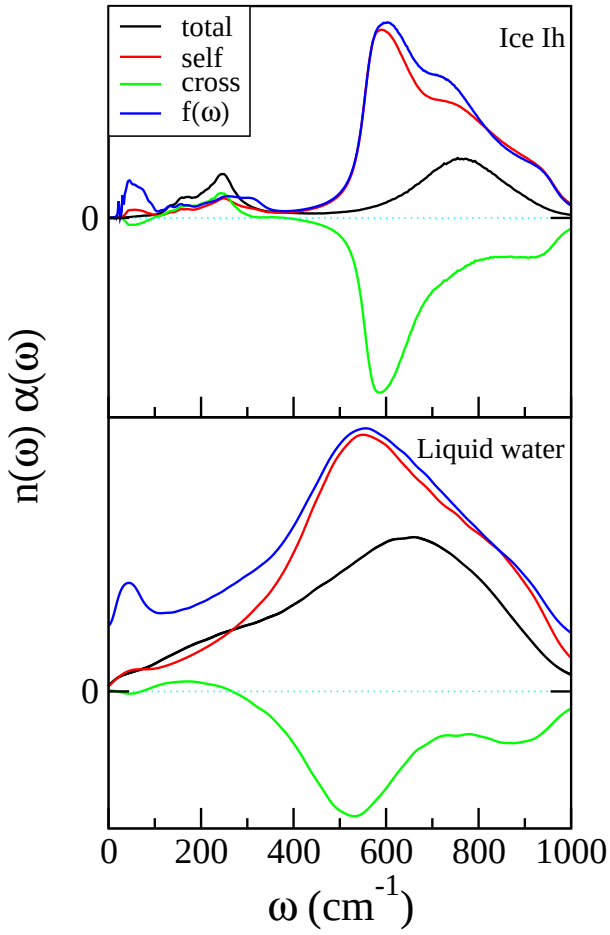

Figure 3.6: Decomposition of the calculated low-frequency infrared spectra (black lines) for ice Ih at 245 K (top panel) and liquid water at 303 K (bottom panel) into self terms (red lines) and cross terms (green lines). The blue lines are the Fourier transform of the classical velocity auto-correlation function for hydrogen atom (without harmonic quantum correction factor).

3.5 Concluding Remarks

The static dielectric constant and low-frequency IR spectra, which reflect dipole fluctuations, are excellent probes for the structures and dynamics of the H-bonded systems, such as liquid water and ice Ih. However, conventional rigid, non-polarizable water models are not able to reproduce these properties for liquid water and ice Ih due to the absence of the polarization effect on the dipole surface in these models. In this chapter, we proposed a simple scheme to incorporate the polarization effect into a reliable rigid, non-polarizable water model (i.e., the E3B model) through a linear mapping between the induced dipole of the water molecule and the electric field on its oxygen atom. The mapping parameter (γ) was obtained by a parametrization against the experimental static dielectric constant at one temperature for either liquid water or ice Ih. The optimal γ values are different for liquid water and ice Ih (1.495 Å^3 for liquid water, and 2.300 Å^3 for ice Ih) as a result of their different electronic structures. The temperature dependence of the static dielectric constant was reproduced well for both systems, and the gap between the dielectric constants of liquid water and ice Ih around the experimental melting temperature was captured quantitatively. Moreover, qualitative agreement between calculated and experimental low-frequency IR spectra was also achieved. In the calculations of the static dielectric constants for ice Ih, the topological algorithm proposed by Buch and coworkers[127] was utilized to generate the proton-disordered configurations, and our results suggest that the thermal fluctuation and the energy differences between different configurations play minor roles in the determination of the dielectric constant, while the polarization effect contributes to the dielectric constant considerably. By decomposing the IR spectra into the contributions from the permanent dipole, induced dipole and their cross term, we showed that the polarization effect is primarily responsible for the intensity of the peaks below 400 cm^{-1} for both liquid water and ice Ih. We also demonstrated the effects of the IR selection rules (e.g., only two out of four translational peaks and one out of three librational peak are visible in the low-frequency IR for ice Ih) by decomposing the IR spectra to the single-particle contribution and the intermolecular contribution. Overall, considering that it requires no further parametrization of the interaction potential in the water model, the present scheme provides a simple and reasonably accurate way to account for the polarization effect on the dipole surface in the calculations of the static dielectric constant and low-frequency IR spectra for liquid water and ice Ih.

As mentioned in section 1.3.2, intermolecular motions will also modulate the high-frequency

OH (OD) stretch in ice Ih. A good description of intermolecular degrees of freedom (i.e., translation and libration) is desirable for the accurate simulations of OH (OD) stretch vibrational spectroscopy, which is the main topic of the subsequent chapters. The quality of the E3B model (at least in terms of describing intermolecular interactions) makes it our choice for describing the bath in the mixed quantum/classical approach for OH (OD) stretch vibrational spectroscopy. The next chapter describes our use of the mixed quantum/classical approach to simulate the simplest vibrational spectrocopy — linear IR and Raman — with the E3B model.

Chapter 4

Vibrational Coupling: IR and Raman

Contents

The content of this chapter corresponds to Ref. 82. Reprinted with permission from J. Phys. Chem. B 116, 13821 (2012); copyright 2012 American Chemical Society. We thank Dr. Fu Li for helpful discussions.

4.1 Introduction

As mentioned in Section 1.3.1, many coupled OH (OD) chromophores in pure H_2O (D_2O) ice Ih could delocalize the OH vibrational eigenstates, and this fact is a double-edged sword for spectral interpretation: on one hand some spectral features (e.g., peak positions) might not directly correspond to local structures in ice Ih (e.g., hydrogen bonding environments) because of

this delocalization; on the other hand, if these spectra can be interpreted appropriately (usually with the help of theory and simulation), additional information may be gleaned concerning the structure and dynamics of ice Ih. In this chapter, we will examine the IR and Raman spectra for neat H_2O and D_2O ice Ih using the mixed quantum/classical approach, and provide assignments of some spectral features.

The OH (OD) stretch spectral range for neat H_2O (D_2O) ice Ih is about 3000-3500 cm^{-1} (2200-2600 cm^{-1}), which is significantly red-shifted from the corresponding gas-phase frequencies due to hydrogen-bonding in ice Ih. The widths of these spectra may arise from multiple sources: 1) the proton disorder in ice Ih (structural heterogeneity); 2) thermal broadening, which could be narrowed spectroscopically; 3) splitting due to the intramolecular coupling between two OH (OD) stretches on the same water molecule; 4) splitting due to the intermolecular coupling between OH (OD) stretches on different water molecules; 5) splitting due to the coupling between stretching modes and lower-frequency modes, such as bending modes and lattice vibations (this type of coupling is sometimes referred to as Fermi resonance). Along with the IR and Raman selection rules, these factors lead to broad spectra with multiple peaks and shoulders,[27,28,36,98,179–193] which have attracted a number of theoretical investigations in the past 40 years,[44,45,122,183,189,194–199] including previous works in our group.[35,80,81]

Whalley[183] summarized progress in the assignments of spectral features prior to 1977. The lowest frequency peak in the ice Raman spectra was assigned to the globally in-phase symmetric stretch, and the rest of the features resulted from the out-of-phase symmetric and anti-symmetric stretches with longitudinal and transverse optical (LO-TO) phonon splitting.[183] Rice and collaborators published a series of theoretical papers on this topic shortly thereafter.[44,45,194–196] They employed a model Hamiltonian including many factors mentioned above (e.g., proton disorder, intra- and intermolecular couplings, Fermi resonance, etc.). They attributed most features in the spectra of neat ice to the interplay between intra- and intermolecular couplings, and argued that the Fermi resonance was a second-order effect, which has more influence on the spectra of D_2O ice Ih.[44,45] In fact, they concluded that the assignment of the spectral features to the molecular symmetric and anti-symmetric stretch modes "may be meaningless."[194] They also thought that the LO-TO splitting had little effect on the OH (OD) stretch vibrational line shapes of ice Ih.[44,45] About two decades later, Buch and Devlin proposed a tetrahedral basic unit to interpret the spectra of ice Ih.[189] A similar theoretical study was later carried out by Wójcik

and collaborators.[197] Researchers are also beginning to employ *ab initio* molecular dynamics methods to calculate vibrational spectra of ice Ih.[122,198] These approaches are promising, but they typically underestimate the OH (OD) stretching frequency. A recent theoretical study by our group found that the intermolecular couplings between the nearest-neighbor local-mode OH chromophores determine most spectral features of H_2O ice Ih.[80,81] In particular, in our model, unlike in the gas phase, the intramolecular coupling in H_2O ice is almost zero, and certainly much smaller than the width of the local frequency distribution (diagonal disorder) and typical intermolecular couplings. Thus, we concur with Rice and co-workers that interpretation of the spectra in terms of the molecular symmetric and anti-symmetric stretches is not appropriate for H_2O ice Ih.[80] We assigned the peaks in the spectra as arising from "strong" and "weak" intermolecular coupling.

Despite the aforementioned studies, one observation remains unexplained: the intensities and patterns of the spectral peaks are quite different in H_2O and D_2O ice Ih, which cannot be simply explained by the frequency shift due to isotope substitution. For instance, the IR spectrum of D_2O ice Ih has a clear peak on the low-frequency side (about 2330 cm^{-1}), while there is only a shoulder in the IR spectrum of H_2O ice Ih. In this chapter, we suggest the intramolecular coupling as a possible reason for this spectral difference. The rest of the chapter is organized as follows. In Section 4.2, we outline our methodology for the spectral calculations; in Section 4.3, we compared our calculated spectra to experiment; in Section 4.4, we analyze our theoretical spectra and provide assignments of the experimental spectral peaks for both H_2O and D_2O; and in Section 4.5, we conclude.

4.2 Simulation Detail

4.2.1 Molecular Dynamics Simulation

As it turns out that OH stretch vibrational spectra of ice Ih are not sensitive to the choice of proton-disordered configuration, a 432-molecule proton-disordered configuration generated by Hayward and Reimer[126] is employed as the initial configuration for MD simulation. This configuration carries zero net dipole and a minimal net quadrupole,[126] and is used as well in subsequent chapters. A molecular dynamics simulation of ice Ih is then performed in the NVT ensemble at 245 K using GROMACS version 3.3,[129] modified for the E3B potential. The simulation

box is scaled to give the experimental lattice constants at 245 K.[7] Simulations are performed using the SETTLE constraint algorithm[131] with a 1 fs time step, and a Berendsen thermostat is employed with a 0.5 ps coupling constant for production runs.[130] Periodic boundary conditions are applied, the cut-off for Lennard-Jones interaction is set to 0.95 nm, and particle-mesh Ewald[132,133] is used to compute the electrostatic interactions. The atomic coordinates are saved every 2 fs in the production run for the spectral calculations. Molecular dynamics simulations are also performed at 100 K and 10 K for spectral calculations using corresponding experimental lattice constants.[7]

4.2.2 Maps for Vibrational Couplings

The focus of this chapter will be vibrational coupling, and we have used two different schemes to calculate the intra- and intermolecular couplings, respectively. In the local-mode basis, the intramolecular coupling ω_{ij}^a between the two OH (OD) stretches on the same molecule is approximated as[200]

$$\hbar\omega_{ij}^a = k_{ij}^a x_i x_j + \frac{cos(\phi)}{m_O} p_i p_j, \tag{4.1}$$

where k_{ij}^a is the mixed second derivative of the potential energy with respect to both bond lengths, evaluated at the minimum, x_i is the $0-1$ position matrix element (using the anharmonic states) of the stretch coordinate for local mode i, p_i is the corresponding $0-1$ momentum matrix element, ϕ is the HOH (DOD) bond angle ($\phi = 104.52^\circ$ for E3B water[84]), and m_O is the oxygen mass. k_{ij}^a, x_i, and p_i all depend on the molecule's environment, and this dependence is reflected in their electric-field "maps" in Table 2.2.

For intermolecular coupling between chromophores i and j on different water molecules, we assume the form of transition dipole coupling, given by

$$\hbar\omega_{ij}^e = \frac{\mu_i'\mu_j'\{\hat{u}_i \cdot \hat{u}_j - 3[(\hat{u}_i \cdot \hat{n}_{ij})(\hat{u}_j \cdot \hat{n}_{ij})]\}}{r_{ij}^3} x_i x_j, \tag{4.2}$$

where $\hat{u}$ is the unit vector in the OH (OD) direction, $\hat{n}_{ij}$ is the unit vector along the line connecting the two point dipoles, r_{ij} is the distance between these point dipoles, and μ_i' is the dipole derivative associated with the ith chromophore. (This form comes from the standard dipole-dipole interaction energy, expanding each dipole to first order in position, and then taking the

appropriate matrix elements.) The map for μ' has also been parametrized against DFT calculations.[82] The only free parameter is then the location of the point dipole, and it was previously parameterized to be 0.67 Å from the oxygen atom along the OH (OD) bond, for TIP4P water model.[80]

4.2.3 Spectral Calculation

As explained in Section 2.5, the OH (OD) stretch has to be modeled quantum mechanically to some extent. The mixed quantum/classical approach with DFT-based "maps" is used here and in subsequent chapters. The working equation in this chapter is Eq. (2.23) with A and B chosen to be the dipole operator, and the lifetime (T_1) is taken to be 300 (700) fs for neat H_2O (D_2O) ice Ih.[31,80]

One subtle point for ice Ih concerns orientational averaging. For an aligned (anisotropic) single crystal, the polarizations of the light electric field can be chosen to be along the a, a' or c crystal axes, leading to three IR spectra, three polarized Raman spectra, and three depolarized Raman spectra. For (isotropic) polycrystalline samples, one needs to average over the orientations of the crystal axes with respect to the lab-fixed axes, as we usually have single crystal ice in an anisotropic simulation box. This has been worked out by McQuarrie,[37] and the formulae we use to calculate spectra in these cases are given in Appendix B.

4.3 Results and Comparison with Experiment

In Fig. 4.1, we plot experimental polarized (cc and aa) and depolarized (aa' and ca) Raman spectra for single crystal H_2O and D_2O ice Ih at 269 K.[182] The polarized spectra have a low-frequency main peak, and two features at higher frequency, while the depolarized spectra only show the higher frequency peaks. The peak frequencies are indicated by the vertical dashed lines. The differences between the D_2O and H_2O spectra are three-fold: 1) the overall D_2O spectra are significantly narrower, 2) the peaks are sharper for D_2O, 3) the spacing between the peaks is even for H_2O, but not so for D_2O. In the same figure we also show our theoretical spectra.

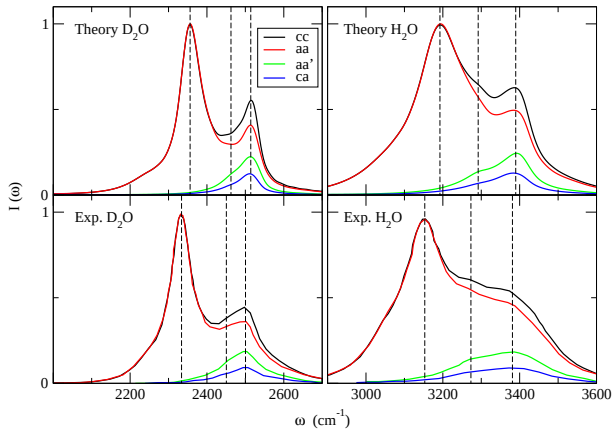

Figure 4.1: Theoretical (E3B model at 245 K, top) and experimental[182] (at 269 K, bottom) polarized (cc and aa) and depolarized (aa' and ca) Raman line shapes for single crystal D_2O (left) and H_2O (right) ice Ih. The vertical dashed lines indicate the frequencies of the different transitions.

Next we consider the IR and unpolarized Raman spectra of neat H_2O and D_2O polycrystalline ice Ih at 100 K. In Fig. 4.2 we show experimental spectra (black lines).[183] The Raman spectra again have three peaks, but now the middle peak is more pronounced. The spacings between the peaks are more or less as above, but all peaks are slightly red-shifted at this lower temperature. The IR spectra also have three peaks—the lowest frequency peak is more pronounced in D_2O. In each case the higher two frequency peaks correspond with the higher two Raman peaks, while the lower frequency peak is blue-shifted from the lower frequency Raman peak. Thus there appear to be four distinct transitions, which are present to greater or lesser extent in IR or Raman spectra. This experimental situation is indicated by the four vertical dashed lines for each isotope. In the same figure we also show our theoretical calculations; theory is again in qualitative agreement with experiment, although the theoretical H_2O IR spectrum does not exhibit the highest frequency peak.

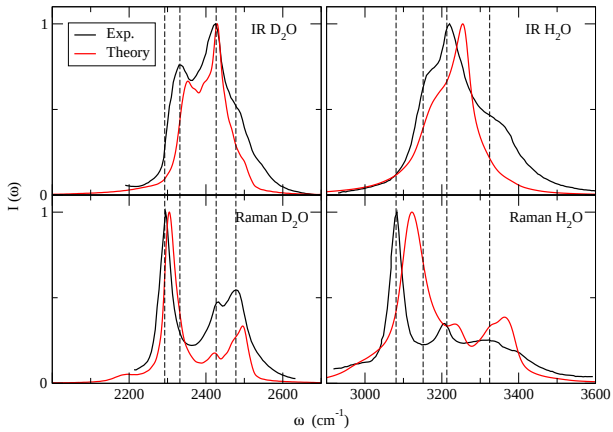

Figure 4.2: Theoretical (E3B model) and experimental IR (top) and unpolarized Raman (bottom) line shapes for polycrystalline D_2O (left) and H_2O (right) ice Ih at 100 K. Experimental line shapes are taken from Ref. 183. The dashed vertical lines indicate the frequencies of the four experimental transitions.

We have also performed theoretical calculations at 10 K, at which temperature the spectra sharpen up and are easier to interpret. (Note that the equilibrium phase at 10 K is ice XI,[7] but one can still study supercooled ice Ih at this temperature, both experimentally and theoretically.) We show the evolution of the theoretical polarized (cc) Raman, depolarized (aa') Raman, and polycrystalline IR line shapes, as a function of temperature, for H_2O and D_2O ice Ih in Figs. 4.3 and 4.4. The frequencies of the four peaks, in all spectra taken together, are shown as the vertical dashed lines for each temperature. All lines blue shift with increasing temperature, and the spacings remain roughly the same. To summarize then, for both H_2O and D_2O there appear to be four transitions, labeled from red to blue, 1 to 4. Peaks 1, 3 and 4 are Raman active, and peaks 2, 3 and 4 are IR active.

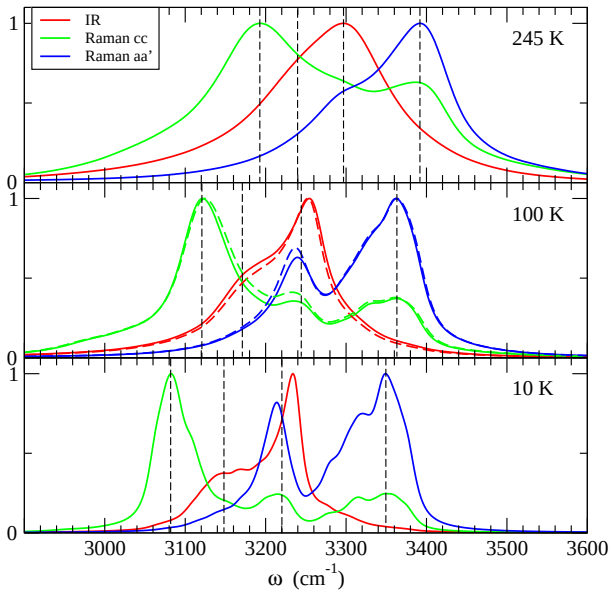

Figure 4.3: Theoretical line shapes for H_2O ice Ih at 245 K, 100 K, and 10 K (from top to bottom). The red lines are the (polycrystalline) IR line shapes, the green lines are the Raman cc line shapes, and the blue lines are the Raman aa' line shapes. The three line shapes are normalized to the same peak height. The dashed lines in the 100 K panel are calculated line shapes setting the intramolecular coupling to 0. The vertical dashed lines are the frequencies of the four transitions at each temperature.

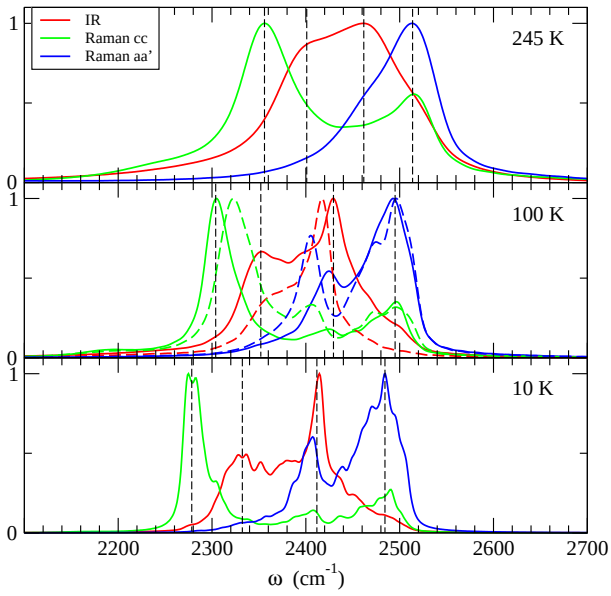

Figure 4.4: Same as Fig. 4.3 but for D_2O ice Ih.

In Figs. 4.5 and 4.6 we plot all available experimental data for the frequencies of these four peaks, as a function of temperature. The open squares are Raman (polarized, depolarized, or unpolarized; single crystal or polycrystalline) experimental results, and the open triangles are IR (polycrystalline) experimental results. For each transition the dashed lines are guides to the eye, to see the temperature dependence. From these graphs one can see how the spacing of the lines differ for H_2O and D_2O. For each isotope we also plot our theoretical results (from Figs. 4.3 and 4.4) as the filled squares for Raman transitions 1, 3, and 4, and filled triangles for IR transitions 2 and 3. The theoretical results show the same trends as experiment, but are uniformly somewhat too blue.

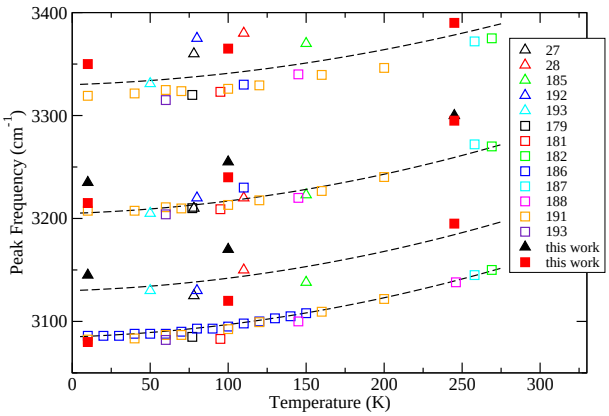

Figure 4.5: Temperature dependence of peak frequencies for H_2O ice Ih. The triangles are from IR line shapes, and the squares are from Raman line shapes. Open symbols are from experimental line shapes with reference number in the legend, and filled symbols are from calculated line shapes. The dashed lines are guides to the eye for the experimental data.

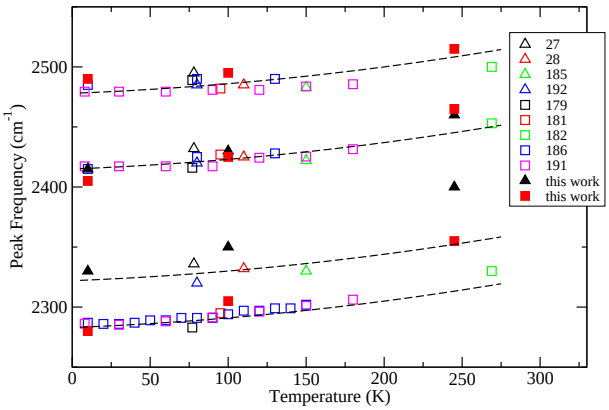

Figure 4.6: Same as Fig. 4.5 but for D_2O ice.

4.4 Spectral Interpretation and Discussion

With the success of our model in qualitatively reproducing several experimental spectra, we can attempt to understand the differences between the line shapes of H_2O and D_2O ice Ih, and to interpret their spectral features. The properties and nature of the vibrational eigenstates, and their selection rules, reflect the competing effects in the exciton Hamiltonian (Eq. (2.22)) of diagonal (transition frequency $\omega_i(t)$) disorder due to the proton-disordered environments of the local chromophores, intramolecular coupling (i.e., ω_{ij}^a), the various kinds of intermolecular coupling (i.e., ω_{ij}^e), and thermal disorder. We can minimize the effect of the latter by focusing here on results at 10 K.

As a first step, let us quantify the extent of diagonal disorder. The diagonal elements of our exciton Hamiltonian are the local OH (OD) stretch 0 - 1 transition frequencies, which are sensitive to hydrogen-bonding and local environments. In ice Ih, all water molecules are tetrahedrally hydrogen bonded (with two donors and two acceptors) to four nearest neighbors, which produces no dispersion in the frequency distribution. If we consider the configuration of the hydrogen-bonding partner of a specific OH, however, one finds that there are four distinct classes[201,202] based on the relative orientations of hydrogen-bonded donor and acceptor, as shown in Fig. 4.7. The hydrogen bonds in the eclipsed dimers (A and B) are along the c axis of ice Ih, while those in the staggered dimers (C and D) are along a direction oblique to the c axis.[202] These motifs can be visualized from the 12-molecule fragment of ice Ih shown in Fig. 1.1 of Chapter 1, where the c axis is vertical and the dotted lines are hydrogen bonds.

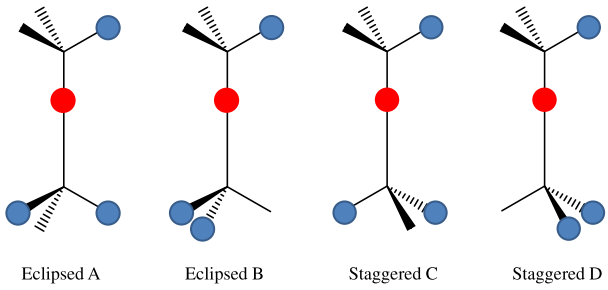

Figure 4.7: Four possible hydrogen-bonding dimers in ice Ih based on the relative orientations of the hydrogen bond donor and acceptor. The red and blue circles are hydrogen atoms in the

dimer. The hydrogen bonds in the eclipsed dimers (A and B) are along the c axis of ice Ih; the hydrogen bonds in the staggered dimers (C and D) are along a direction oblique to the c axis.

We can decompose the site frequency distribution into contributions from each class, as shown in Fig. 4.8 for ice Ih at 10 K. The relative area of the distribution for each class reflects the statistical percentage of that class in ice Ih, which in our configuration is very close to the percentage assuming the proton disorder is locally random (A: $1/6$; B: $1/12$; C: $1/2$; D: $1/4$). The frequency distributions of each class are very similar, indicating that this is not an important source of diagonal disorder. This is not consistent with the claim of two different kinds of hydrogen bonds in ice,[201,203] but is consistent with the refutation[204,205] of this claim. The widths of the frequency distributions for each class are mainly due to the proton-disordered environments of each dimer, but the imperfect tetrahedral hydrogen bond network of E3B water molecules (with HOH angles of 104.52°, not 109.47°), and residual thermal motions at 10 K, also contribute. A noticeable difference between H_2O and D_2O ice Ih is that the site frequency distribution of D_2O ($\sim$55 cm^{-1}) is narrower than that of H_2O ($\sim$80 cm^{-1}) at 10 K, which partially explains the difference in the line widths of H_2O and D_2O vibrational spectra. These differences have to do with the difference in scale between OH and OD stretch frequencies, whose ratio is approximately related to the square root of the ratio of the relevant reduced masses (which is roughly $\sqrt{2}$).

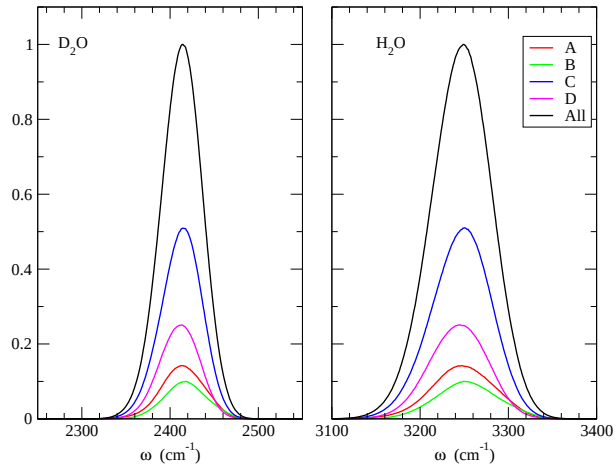

Figure 4.8: Calculated local OH (OD) stretch frequency distributions for the four classes of OH (OD) bonds in ice Ih, and their sum, at 10 K. Left panel is for D_2O; right panel is for H_2O.

We next consider the off-diagonal elements of the Hamiltonian, the vibrational couplings (i.e., ω_{ij}^a and ω_{ij}^e). Intramolecular couplings are calculated using Eq. (4.1), and intermolecular couplings are calculated within the interacting transition dipole approximation, Eq. (4.2). In order to understand the intermolecular couplings, we plot in Fig. 4.9 the radial distribution function of the point dipole positions, $g_{MM}(r)$ (M designates point dipole position), for ice Ih at 10 K. The dipolar couplings within 3.6 Å in $g_{MM}(r)$ are grouped into six classes, shown in Fig. 4.10. Again, in order to understand these classes, it may be helpful to consult Fig. 1.1. The nearest OH pairs are approximately 2.4 Å apart, denoted as S (for strong). Four types of pairs are similar in terms of distances (from 3.1 to 3.5 Å), and are all within the first solvation shell of the hydrogen bond donor water molecule. They are denoted as W0, W60, W120 and W180 (W for weak), in which the numerals are the dihedral angles formed by the two OH bonds. The final class, denoted as WII, is for molecules in the second solvation shell of the hydrogen bond donor water molecule (II means the second solvation shell). However, point dipoles in the WII pairs are not far away from each other (∼3.45 Å apart) in the imperfect tetrahedral hydrogen bond network of E3B water molecules.

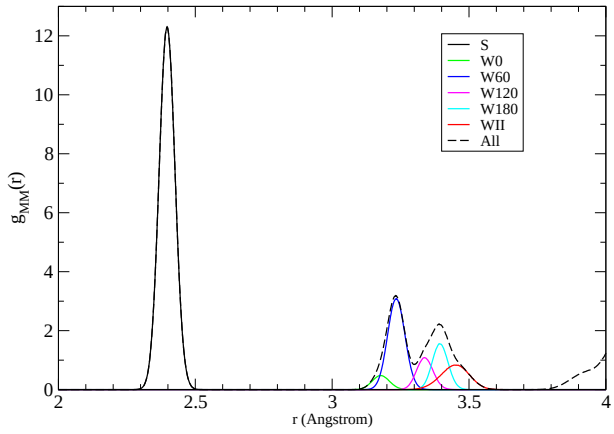

Figure 4.9: Calculated radial distribution function of the dipole positions for OH stretches in ice Ih, and its decomposition into the six classes of pairs in H_2O ice Ih at 10 K. The dipole position of the OH chromophore is located at 0.67 Å from the oxygen atom along the OH bond.[80]

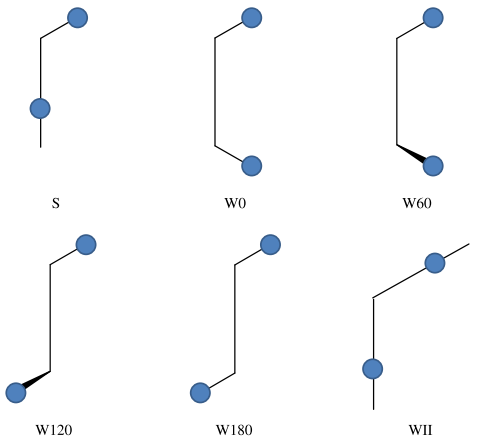

Figure 4.10: Six possible classes of dipolar couplings between two OH chromophores within 3.6 Å at 10 K. Blue circles are the two hydrogen atoms in the pair. The oxygen atoms are represented by the vertices.

We plot the distributions of intermolecular couplings, as well as intramolecular couplings, for both H_2O and D_2O at 10 K, in Fig. 4.11. The S pairs lead to the strongest (in magnitude) intermolecular couplings (about -40 cm^{-1} for H_2O). The dipolar intermolecular coupling is affected not only by the distance between two transition dipoles, but also by their relative orientations (see Eq. (4.2)), and so nearer pairs do not necessarily have stronger coupling. In fact, relatively distant WII coupling pairs show the largest positive couplings in the exciton Hamiltonian. As Li and Skinner have seen before,[80,81] the intramolecular couplings in H_2O are relatively small, peaked at -3 cm^{-1}. Given that the diagonal disorder in the Hamiltonian for H_2O at 10 K is about 80 cm^{-1}, one may anticipate that the intramolecular couplings will not

significantly change the vibrational density of states, while the intermolecular couplings may introduce splittings. The widths of the coupling distributions arise primarily from the intrinsic structural heterogeneity due to the proton disorder and imperfect tetrahedral hydrogen bond network of E3B, rather than residual thermal motions at 10 K.

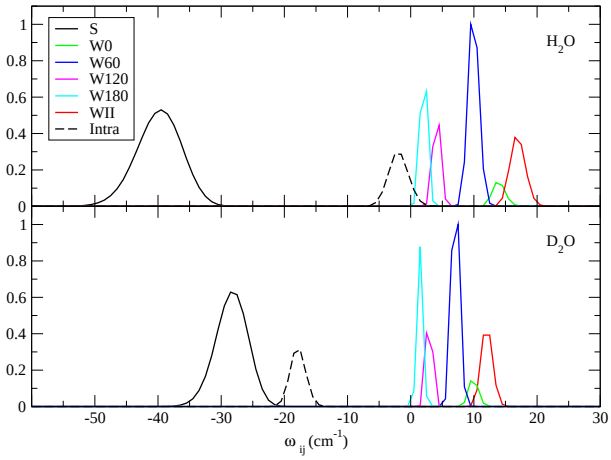

Figure 4.11: Calculated distributions of dipolar intermolecular couplings within 3.6 Å, and intramolecular coupling, for H_2O (top) and D_2O (bottom) ice Ih at 10 K.

The coupling distributions for D_2O (bottom panel of Fig. 4.11) are quite different from those for H_2O. The intermolecular couplings (S pairs: on the order of -28 cm^{-1}; WII pairs: 12 cm^{-1}) are smaller in magnitude for D_2O, while the intramolecular couplings (-18 cm^{-1}) are much larger. These can be qualitatively understood from Eqs. (4.1) and (4.2): for a harmonic oscillator, the position matrix element x is proportional to the square root of the reduced mass of the oscillator, while the momentum matrix element p is inversely proportional to the square root.[206] The intermolecular couplings in Eq. (4.2) depend on x, but not p, so a smaller reduced mass leads to a larger coupling magnitude for H_2O. In Eq. (2) for intramolecular couplings, k_{ij}^a is usually positive, and $cos(\phi)/m_O$ is negative. It is the competition between the two terms in Eq. (4.1) that results in more negative intramolecular couplings for D_2O. As the diagonal disorder in the Hamiltonian for D_2O at 10 K is about $\sim$55 cm^{-1}, we can expect that in D_2O

both inter- and intramolecular couplings will introduce splittings in the OD stretch vibrational density of states (see below).

With a better understanding of the exciton Hamiltonian for H_2O and D_2O, we next investigate the effects of these couplings on the OH (OD) vibrational frequency distribution.[80] The top (bottom) panel in Fig. 4.12 shows the vibrational frequency distribution with various couplings for H_2O (D_2O) at 10 K. We begin by showing the frequency distribution when all vibrational coupling is neglected—these are the black curves, which are identical to those in Fig. 4.8. Next we include only the intramolecular coupling for each molecule, and then diagonalize the Hamiltonian for each configuration, which produces the red lines. For H_2O this coupling does essentially nothing, since the magnitude of the coupling is small compared to the width of the diagonal disorder, while for D_2O, where the intramolecular coupling is much larger, it splits the peak significantly. Next we remove the intramolecular coupling and include intermolecular coupling involving all pairs with separations greater than 3 Å (that is, we include all the "weak" couplings). These results are shown by the green curves. The effect of these weak couplings is similar for both H_2O and D_2O, broadening the frequency distribution, with the highest amplitude on the low-frequency side. For D_2O we next include both intramolecular and weak coupling to obtain the orange curve, which shows that the intramolecular coupling further broadens the frequency distibution, but the highest amplitude is still on the low-frequency side. We next remove the weak and intramolecular coupling, and now include only the strong couplings, which results in the blue curves. These show dramatic perturbations from the diagonal distributions, because these strong couplings are on the order of the width of the diagonal disorder. One sees that the strong couplings substantially broaden the distributions (but less so for D_2O, since the couplings are smaller). Finally, if one includes all couplings, one obtains the magenta lines. For both H_2O and D_2O these curves each have three main peaks, at about 3140, 3220, and 3360 cm^{-1} for H_2O, and 2320, 2410, and 2490 cm^{-1} for D_2O. Comparing the magenta, blue, and green curves for H_2O, one can reasonably conclude that these three peaks arise from strong, weak, and strong couplings respectively, which we denote SL (L is for low-frequency), W, and SH (H is for high), respectively. For D_2O one compares the magenta, blue, and orange curves, similarly labeling the three peaks as SL, W/I (I is for intramolecular), SH.

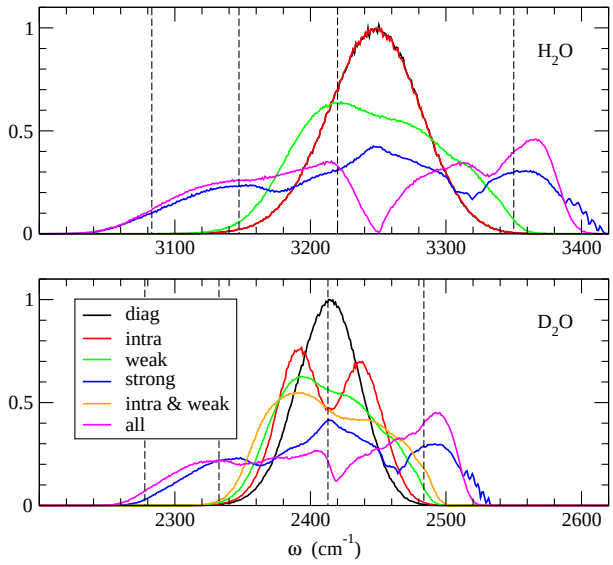

Figure 4.12: Theoretical frequency distributions of H_2O and D_2O ice Ih at 10 K. The black lines are the local OH (OD) stretch frequency distributions. The red lines include only the intramolecular couplings. The green lines include only the "weak" intermolecular couplings. The blue lines include only the "strong" intermolecular couplings. The orange line includes only the intramolecular and weak intermolecular couplings. The magenta lines include all couplings. The dashed vertical lines are the frequencies at 10 K from Figs. 4.3 and 4.4, and are labeled from left to right, as C, SL, W (W/I), SH in H_2O (D_2O) ice.

The frequency distributions are related to spectra, but are, of course, not the same thing, since the latter are weighted by the square of the transition dipoles or polarizability, and also have dynamical and lifetime effects. Still, one would expect to see signatures of the frequency distribution in the spectra, to different extents for the different kinds of line shapes. In Figs. 4.3 and 4.4 we showed vertical dashed lines for the four peaks in the different spectra, for each of the temperatures and isotopes. In Fig. 4.12 we also show these same four dashed lines for 10 K for each isotope. In each case the three higher-frequency lines correspond roughly to the peaks in the frequency distribution, and which we label as SL, W (W/I), SH for H_2O (D_2O). For each isotope the lowest frequency line occurs where the frequency distribution is actually quite small. The transition only appears in polarized Raman spectra, where, as discussed

earlier,[80,183,189,194,195,197,207] the intensity is enhanced by the constructive interference of many in-phase transitions, which we denote as C for collective. In summary, then, the four transitions 1, 2, 3, and 4, are designated C, SL, W (W/I), SH for H_2O (D_2O). Transition 1 occurs in the polarized Raman (it is the main peak), transition 2 is in the IR, and transitions 3 (which is the main peak in the IR) and 4 appear in all spectra.

Certainly for H_2O our results show that the intramolecular coupling makes essentially no contribution to the spectroscopy. To make this very clear, in Fig. 4.3 we show theoretical Raman and IR line shapes for 100 K where the intramolecular coupling has been set to 0—one sees essentially no change. Since the intermolecular couplings are so much larger than the intramolecular couplings, this implies that the basis of the symmetric and anti-symmetric molecular eigenstates is not useful or relevant for understanding the spectra. This is in agreement with the previous anlaysis by Li and Skinner[80] and with earlier work by Rice and coworkers,[194] but in disagreement with the recent intrepretation by Shigenari and Abe.[193] For D_2O the intramolecular coupling is clearly much more important (see the results for no intramolecular coupling at 100 K in Fig. 4.4), and it changes the spacing among the four transitions, and their intensities. Still, the qualitative features of the spectra do not change from H_2O to D_2O, and so our conclusion is that here too the molecular eigenstates are not relevant.

With regard to the temperature dependence of the theoretical line shapes in Figs. 4.3 and 4.4, higher temperatures lead to larger amplitudes of the low-frequency motions, which on average weakens hydrogen bonds, producing a blue shift in the frequencies. In addition, the larger range of configurations sampled at higher temperatures broadens the lines. Obtaining the correct frequency for the C (collective) line is particularly difficult for us, since it is collective (and not related to specific more local vibrational eigenstates). And indeed, one sees in Figs. 4.5 and 4.6 that we do not predict the temperature dependence of the peak frequency for this (lowest-frequency) transition very well.

4.5 Concluding Remarks

In this chapter, we employ our mixed quantum/classical approach to simulate high-frequency OH (OD) spectra of neat H_2O (D_2O) ice Ih at different temperatures, including IR and Raman spectra of single crystal and polycrystalline ice Ih. Reasonable agreement is found between

calculated and experimental line shapes. Through investigation into the structure and frequency distributions for both H_2O and D_2O, we find that it is the stronger intramolecular couplings that change the spectral features (spacings and widths) in D_2O, and it is primarily the smaller "strong" intermolecular couplings that makes the line shapes for D_2O narrower compared to H_2O, in agreement with Rice and co-workers' results.[44] Based on these, we have suggested assignments for the experimental peaks for both H_2O and D_2O. Our assignments are based on understanding the strong and weak intermolecular couplings and intramolecular couplings in the basis of local OH (OD) stretches, rather than in the basis of molecular symmetric and anti-symmetric stretches.[183,193] Large intermolecular couplings and diagonal disorder make molecular symmetric and anti-symmetric stretches not useful as a basis for spectral interpretations.

The model is not without its shortcomings. These include: (1) Ice Ih should have nuclear quantum effects.[171,208,209] Classical molecular dynamics does not describe the spatial delocalization of hydrogen (deuterium) positions in ice Ih,[210] which will potentially affect the line width, and the classical treatment of lattice librations at low temperature is not well justified. (2) The Fermi resonance between OH (OD) stretches and bending overtones is neglected in our model. This effect has been studied extensively by both experiments[211,212] and theory.[44,45,196] It is thought that the effects of Fermi resonance in D_2O ice is likely to be more profound than for H_2O,[44] so the peaks at $\sim$2425 cm^{-1} and $\sim$2485 cm^{-1} in the experimental Raman spectra at 100 K may have contributions from Fermi resonance. (3) In terms of the spectroscopic modeling, the use of the transition bond polarizability model might contribute to the overestimation of the intensity of high-frequency modes in Raman spectra. Transition dipole coupling is not necessarily a good approximation for the nearest OH pairs. Actually, many researchers[44,189,197] treat these couplings differently from longer range intermolecular couplings. Finally, our frequency maps may not be particularly accurate, since they were parameterized from liquid water.[35,80] Nonetheless, our model appears to be good enough to help us understand most of the qualitative spectral features in both H_2O and D_2O ice Ih.

As demonstrated in this chapter, the extraction of the information about vibrational coupling from linear vibrational spectroscopy requires some level of theoretical modeling. Therefore, experimentalists would like some techniques to examine vibrational coupling more directly, and pump-probe anisotropy decay measurement is one of such techniques. The next chapter aims to understand this nonlinear vibrational spectroscopy and its relation to vibrational coupling.

Chapter 5

Vibrational Coupling: Pump-Probe Anisotropy Decay

Contents

Most content of this chapter corresponds to a manuscript submitted to J. Chem. Phys. with Fu Li and James L. Skinner. We thank Professor Mino Yang for helpful conversations.

5.1 Introduction

We have discussed vibrational coupling extensively in the previous chapter, primarily from a frequency-domain perspective, and we know that vibrational coupling delocalizes vibrational eigenstates in ice Ih so that the vibrational excitation is shared by many chromophores. However, we have not yet answered the question of how quickly the vibrational excitation is delocalized between these chromophores. In order to answer this question, experimentalists have utilized time-domain ultrafast nonlinear vibrational spectroscopy, one type of which — vibra-

tional pump-probe anisotropy decay — will be the focus of this chapter. In the time-domain description, we use the term "resonant vibrational energy transfer (VET)" to describe the delocalization of vibrational excitation. "Resonant" is used because of the near-degeneracy of VET donor and acceptor chromophores in vibrational energy levels. This resonant energy transfer process, in fact, has been discussed extensively for electronic excitation in the past fifty years.

Most studies on electronic resonant energy transfer also adopt the system-bath description mentioned in Section 2.2. The system includes many chromophores (excitons) coupled through inter-chromophoric coupling, whose energy levels are modulated by the bath (i.e., phonons) through the system-bath (exciton-phonon) coupling. With a perturbative treatment and within the Markovian approximation, there are two limits for resonant energy transfer:[213–216] incoherent and coherent. The former case is in the weak inter-chromophoric coupling limit, and can be described either by a master equation in the local site basis,[214,215] or by the Förster theory with some additional approximations.[30,215,217] The latter case is in the weak system-bath coupling limit, and can be described by the Redfield equation[218] or Lindblad equation.[219,220] The Förster theory in the incoherent limit is particularly useful as it allows the extraction of some structural information (e.g., distance and relative orientation) of molecular systems from some signatures (e.g., pump-probe anisotropy decay) of resonant energy transfer in ultrafast spectroscopic measurements.

Due to the recent development of ultrafast infrared spectroscopy, people have the opportunity to examine resonant *vibrational* energy transfer.[31,221–229] Specifically, OH (OD) vibrational energy transfer has been studied in liquid water and ice Ih.[225–229] The system-bath description for vibrations in ice is already discussed in Section 2.2, and it is very natural for experimentalists to apply the theories developed originally for electronic excitation to the vibrational case. In fact, Bakker and coworkers have used the Förster theory to interpret their pump-probe anisotropy decay results, which carry information about OH (OD) VET, for both liquid water and ice Ih. On the theoretical side, a recent work by Yang, Li and Skinner[230] showed that the VET process in liquid water is incoherent on the time scale of the pump-probe anisotropy measurement, and could be described by the Förster theory with some modifications. Therefore, the remaining question is whether incoherent description is appropriate for VET in ice Ih.

To the best of our knowledge, there are only two theoretical papers by Poulsen, Nyman and coworkers on the VET in ice Ih.[231,232] They used the clusters of 15 water molecules to

represent ice Ih, and ran either the wave packet dynamics or Car-Parrinello molecule dynamics (CPMD) to monitor the survival probability of the excitiation on the initially excited mode or potential energy of the excited molecule.[231,232] Both methods led them to conclude that the resonant OH vibrational energy transfer in ice Ih occurs within 100 fs,[231,232] in agreement with the recent pump-probe experiment.[31] However, they neither made direct comparison with the pump-probe anisotropy measurement (since their calculations preceded the experiment), nor identified the VET in ice to be incoherent or coherent. Therefore, in this chapter we take up the task of resolving these two issues. The rest of the chapter is organized as follows: In Section 5.2, we introduce pump-probe anisotropy decay, and outline the methodology for calculating it; in Section 5.3, we present our calculated anisotropy decay, and compare it to experiment; in Section 5.4, we analyze the mechanism, timescales, and transport pathways of OH vibrational energy transfer in neat H_2O ice Ih; and in Section 5.5, we conclude.

5.2 Pump-Probe Anisotropy Decay

In a typical vibrational pump-probe experiment, two infrared pulses are incident on the sample: the first (pump) pulse excites some chromphores (e.g., OH stretch), and after a delay time t, a second (probe) pulse probes the vibrational excitation, which might remain on the original excited chromophores or might be transferred to other chromophores. As the polarization (i.e., direction of the electric field) of laser pulse can be well controlled, the polarizations of pump and probe pulses can be parallel or perpendicular to each other, and the collected signals are denoted as $I_{\parallel}(t)$ and $I_{\perp}(t)$, respectively. As light preferentially interacts with chromophores aligned with its polarization, the difference signal $I_{\parallel}(t) - I_{\perp}(t)$ will decrease with t primarily due to three mechanisms: 1) molecular rotation: the excited chromophore, which is aligned well with the pump pulse, might rotate during t; 2) VET: the vibrational excitation is transferred to another chromophore, which might interact more strongly with the perpendicular probe pulse; 3) vibrational energy relaxation (VER): vibrational excitation is dissipated thermally. In order to eliminate the effect of VER one can construct a quantity $r(t)$ called the anisotropy decay, given by

$$r(t) = \frac{I_{\parallel}(t) - I_{\perp}(t)}{I_{\parallel}(t) + 2I_{\perp}(t)}. \tag{5.1}$$

Therefore, anisotropy decay could tell one something about molecular rotation and VET in molecular systems. Specifically for OH stretch in ice, molecular rotation is hindered due to the hydrogen-bond network (see section 1.3.2), so the anisotropy decay is an ideal way to understand OH stretch VET in ice Ih experimentally.

As there are multiple interactions between the sample and light in a pump-probe experiment, the calculation of vibrational anisotropy decay usually involves the doubly-excited vibrational states, as well as the singly-excited states and the ground state. However, Yang, Li and Skinner[230] showed that within some reasonable approximations, the anisotropy decay for the frequency-integrated detection in the context of the mixed quantum/classical approach can be calculated approximately for isotropic systems by

$$r(t) = \frac{2}{5} \frac{\langle \sum_j m_j(t)^2 |U_{ji}(t)|^2 m_i(0)^2 P_2(\hat{u}_i(0) \cdot \hat{u}_j(t)) \rangle_i}{\langle \sum_j m_j(t)^2 |U_{ji}(t)|^2 m_i(0)^2 \rangle_i}, \tag{5.2}$$

where $m_i \equiv \mu_i' x_i$ is the magnitude of the transition dipole of chromophore i, $U_{ji}(t) \equiv \langle j | \, U(t) \, | i \rangle$, P_2 is the second Legendre polynomial, and the brackets with the subscript i denote a time average over the trajectories and over all initially excited chromophores i.

To clarify the physical meaning behind anisotropy decay $r(t)$, we can make further approximations. If we make the Condon approximation (i.e., the magnitudes of the transition dipoles m_i are taken to be constants.), Eq. (5.2) becomes

$$r(t) = \frac{2}{5} \left\langle \sum_j |U_{ji}(t)|^2 P_2(\hat{u}_i(0) \cdot \hat{u}_j(t)) \right\rangle_i \tag{5.3}$$

where the identity $\sum_j |U_{ji}(t)|^2 = 1$ is used. Note that the Condon approximation is good for ice since all the water molecules in ice are fully hydrogen bonded.[35] The physical meaning of Eq. (5.3) is evident: $|U_{ji}(t)|^2$ is the transition probability of the excitation from chromophore i to j for $j \neq i$ at time t, and $P_2(\hat{u}_i(0) \cdot \hat{u}_j(t))$ describes the molecular rotation and the molecular arrangement in the material. If there is no energy transfer in the system (i.e., $U_{ji}(t) = \delta_{ji}$), Eq. (5.3) recovers the conventional P_2 rotational time correlation function with a prefactor $2/5$. If the molecular rotation can be ignored in the material on the time scale of experiment (i.e.,

$\hat{u}_j(t) \approx \hat{u}_j(0)$), which is the case for ice, Eq. (5.3) becomes

$$r(t) = \frac{2}{5}\left[S(t) + \left\langle \sum_{j\neq i} |U_{ji}(t)|^2 P_2(\hat{u}_i(0)\cdot\hat{u}_j(0))\right\rangle_i\right], \tag{5.4}$$

where $S(t)$ is the so-called survival probability, defined by

$$S(t) = \left\langle |U_{ii}(t)|^2 \right\rangle_i . \tag{5.5}$$

This survival probability tells one the average probability of finding the excitation remaining on chromophore i at time t given that the initial excitation is localized on chromophore i. By monitering the time evolution of the survival probability, one can characterize the resonant energy transfer in the system. Therefore, the anisotropy decay in this situation reflects the resonant energy transfer weighted by some geometric factors $P_2(\hat{u}_i(0)\cdot\hat{u}_j(0))$.

5.3 Results and Comparison with Experiment

The system that Timmer and Bakker studied is the OH stretch in ice Ih of either neat H_2O or H_2O/HOD/D_2O mixture at 270 K. The effect of OD here is essentially to dilute the OH chromophores in the system as the OD stretch is not an effective VET acceptor for OH vibational excitation due to large frequency mismatch between the OH and OD stretches. Since fewer OH stretch acceptors surround an OH stretch donor in the H_2O/HOD/D_2O mixture compared to neat H_2O, one might expect that VET in ice is impeded or slowed down in the isotopic mixtures. Indeed, Timmer and Bakker observed that as the hydrogen mole fraction decreases, the anisotropy decay $r(t)$ slows down dramatically, and the "plateau" in $r(t)$ at 1 ps rises. As mentioned earlier, these observation was interpreted in terms of the Förster theory of incoherent hopping by Timmer and Bakker, and they concluded that VET outside the first solvaion shell was negligible, and the level of the plateau reflected the probability of finding acceptors (i.e., OH chromophores) within the first solvation shell. Within their dipole-dipole coupling model, the rate of intramolecular hopping was larger than all intermolecular rates since the distance between the two dipoles is the closest.

To mimic the experiment, we performed MD simulations for ice Ih of neat H_2O and of

H_2O/HOD/D_2O mixtures using the E3B model at 245 K (the melting point of the E3B model is 251 K[84]). For neat H_2O, the simulation is the same as that in Section 4.2. For isotopic mixtures, the simulation is run with D_2O, then we assign the D atoms at random to be H atoms to match the given hydrogen mole fraction, and to obey the rule of the geometric mean for the equilibrium constant of the isotopic self-exchange reaction of water (i.e., $K_D = 4$ for H_2O + $D_2O \rightarrow$ 2HOD), which is close to the experimental value for liquid water at about 300 K.[233,234] Then we perform an average over 80 different random realizations of the H_2O/HOD/D_2O mixture to obtain a spectrum for each concentration.

Fig. 5.1 displays the experimental (270 K)[31] and calculated (245 K) (from Eq. (5.2)) pump-probe anisotropy decay for H_2O/HOD/D_2O ice Ih at various hydrogen mole fractions including 100%. Note that the experimental work by Timmer and Bakker showed that the anisotropy decay for this system has little temperature dependence and is not sensitive to the probe frequency,[31] so our calculation is done for the frequency-integrated detection at 245 K, even though their experimental data are frequency-averaged signals with their two-color pump-probe experimental setup at 270 K.[31] As shown in Fig. 5.1, our calculations are in fairly good agreement with the experiment for all hydrogen mole fractions.[31] In addition to the fast initial decay and the plateau after 300 fs, our calculated anisotropy decays also have some oscillations, especially for the mixtures at low hydrogen mole fractions. A high-frequency component is seen at short times, especially at low OH concentrations, and a low-frequency component is observed on a longer time scale. However, only the low-frequency oscillation is observed in the experiment. We confirm that the oscillations in our calculated results are mainly due to the hindered rotation (libration) in ice Ih by checking the OH rotational time correlation function.

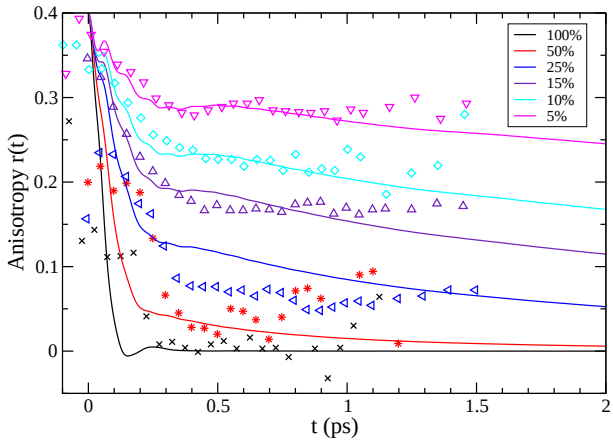

Figure 5.1: Calculated (at 245 K) and experimental (at 270 K) pump-probe anisotropy for H_2O/HOD/D_2O ice Ih at hydrogen mole fractions (as indicated by the colors and the legend).

5.4 Discussion

In spite of some discrepancies between our theoretical results and experiment, we believe that our model qualitatively captures the physics of the OH stretch resonant energy transfer in ice Ih. Therefore, we will attempt to understand the mechanism and paths of the resonant energy tranfer in ice Ih with our theoretical model, and will focus our attention on the case of neat H_2O hereafter. To this end, we first classify the relevant OH donor-acceptor pairs in the system, and this classification has been already done in Section 4.4 (Fig. 4.10). In order to show these VET donor-acceptor pairs in ice Ih more clearly, a six-molecule fragment of ice Ih with a vertical c axis of the hexagonal crystal lattice is shown in Fig. 5.2. The large blue spheres are oxygen atoms, and other color-coded small spheres are hydrogen atoms. For pictorial clarity, we assume the initial excitation locates on the red hydrogen atom, and the water molecule to which the red hydrogen atom belongs is regarded as the central water molecule. The red and purple hydrogen atoms in the central water form an intramolecular donor-acceptor pair, and the magnitude of its coupling is very small as shown in Fig. 4.11. The strongest intermolecular couplings are the four red-green pairs (i.e., S pairs), and we expect these four green hydrogens to be the main acceptors of the vibrational energy. The other four yellow hydrogen atoms within the first

solvation shell of the central water molecule might also accept the excitation through the weak intermolecular couplings, which can be further classified to W0, W60, W120 and W180 pairs (see Fig. 4.10). Note that in this particular fragment in Fig. 5.2, only W60, W120 and W180 pairs are shown. The final important donor-acceptor class is the red-orange pairs (WII pairs); as mentioned in the previous chapter, the vibrational coupling of the WII pair is the second strongest intermolecular coupling in the system.[82] The couplings of donor-acceptor pairs other than these six (e.g., red-white hydrogen pairs in Fig. 5.2) are probaby negligible since they are very apart, and their coupling strengths are very small. We thus group all these couplings together as a seventh class.

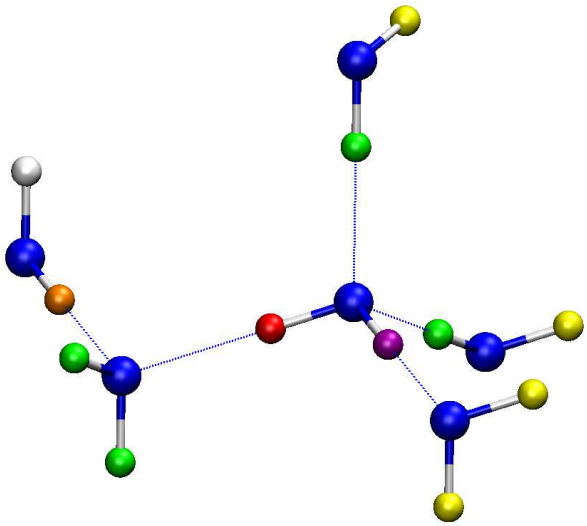

Figure 5.2: Vibrational resonant energy transfer donor-acceptor pairs in a six-molecule fragment of ice Ih. The c axis is vertical, and the dotted lines are hydrogen bonds. The large blue spheres are oxygen atoms, and the small spheres of white and other colors are hydrogen atoms. The locations of the vibrational excitation are taken to be on the hydrogen atoms for pictorial clarity. Assume that the initial vibrational excitation is localized on the OH chromophore involving the red hydrogen atom, and the vibrational excitation can transfer to the four green hydrogen atoms through the intermolecular couplings of S class. The excitation can also transfer to the orange hydrogen atom through the intermolecular coupling of WII class, to the yellow hydrogen atoms through the intermolecular coupling of weak classes (only W60, W120 and W180 shown here),

and to the purple hydrogen atom through the intramolecular coupling. The classification of the intermolecular pairs is explained in the main text.

With a better understanding of the donor-acceptor pairs in the system, we now examine the survival probability $S(t)$ of the OH vibrational excitation, which is a direct way to investigate the resonant energy transfer process. As shown in Fig. 5.3, the survival probability (solid black line, from Eq. (5.5)) decays on a similar (albeit slightly longer) time scale to the anisotropy decay. This suggests the initial rapid drop in the anisotropy decay is mainly due to resonant energy transfer for high OH concentrations. To further verify this, we consider Eq. (5.4), in which the molecular rotation is neglected. As mentioned above, the S pairs (red-green hydrogen atoms in Fig. 5.2) are expected to be the main donor-acceptor pairs in the system, which we confirm in Fig. 5.3 by calculating the survival probability including only the intermolecular couplings of S pairs in the Hamiltonian (dashed black line). Therefore, at short times the excitation will primarily transfer from the initially excited OH chromophore to its four neighbor chromophores through the intermolecular couplings of S pairs (that is from the red hydrogen atom to the four green hydrogen atoms in Fig. 5.2). Considering that the angle between the two OH chromophores in the S pairs is about $(180^\circ - 109.52^\circ =)\ 70.48^\circ$, the geometrical factor $P_2(\hat{u}_i(0) \cdot \hat{u}_j(0))$ gives -1/3, leading to an approximate relation between the anisotropy decay and the survival probability at short times for ice Ih:

$$r(t) = \frac{2}{15}[4S(t) - 1], \tag{5.6}$$

where the identity that $\sum_j |U_{ji}(t)|^2 = 1$ is applied again. The anisotropy decay estimated in this way, using the "exact" survival probability (solid black line in Fig. 5.3), is plotted as the dotted line in Fig. 5.4. Within about 100 fs, the agreement between the dashed and dotted lines is fairly good, but the dotted line is higher within about 50 fs and lacks the initial oscillation as a result of the negligence of the hindered molecular rotation. Hence, it is evident that the main physical origin of the initial drop is resonant energy transfer, which will be shown below to have coherent characteristics. The discrepancy between the dashed and dotted lines after 100 fs is not surprising, as Eq. (5.6) is only valid at short times, and at long times the excitation is delocalized further (beyond the first solvation shell of the central molecule). By

examining the survival probabilities and the anisotropy decays for the $H_2O/HOD/D_2O$ mixutres, we find the dependence of the end level on the hydrogen mole fraction results from the level of delocalization of the excitation. The contribution from molecular rotation, meanwhile, is constant for different hydrogen mole fractions.

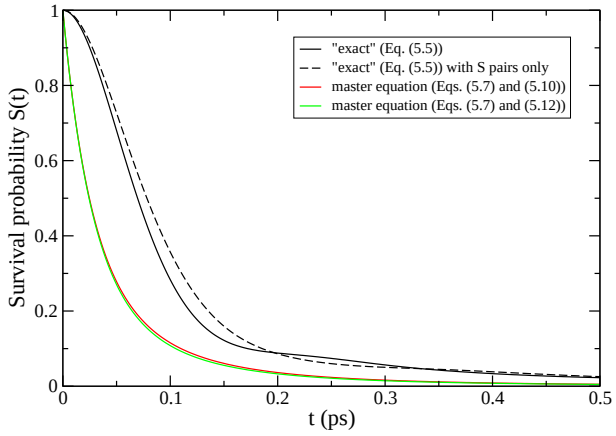

Figure 5.3: Calculated survival probability of the vibrational excitation. The solid black line is the "exact" result from Eq. (5.5), and the dashed black is also from Eq. (5.5) but with only the intermolecular couplings of S class included in the excitonic Hamiltonian. The red and green curves are the results from the master equation (Eq. (5.7)) with the hopping rates calculated using Eq. (5.10) and Eq. (5.12), respectively.

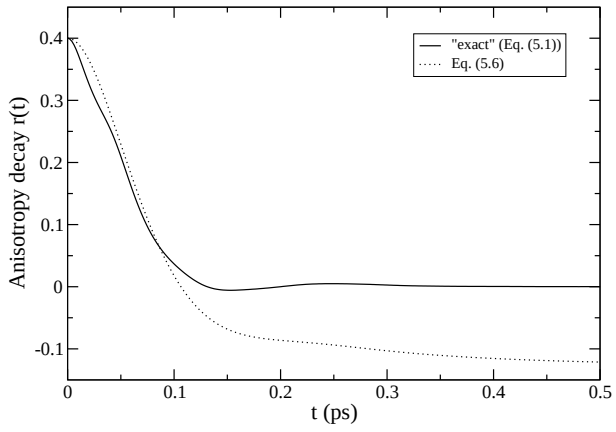

Figure 5.4: Anisotrpy decay for neat H_2O calculated "exactly" from Eq. (5.2) (solid line), and estimated approximately from Eq. (5.6) (dotted line).

The survival probability shows a recurrence between 200 fs and 300 fs, which is a characteristic feature of the coherent energy transfer. This recurrence also contributes to the oscillation between 200 fs and 300 fs in the anisotropy decay. To further investigate the mechanism of the energy tranfer in ice Ih, we would like to examine whether an incoherent hopping model can reproduce this survival probability. A perturbative Markovian treatment of the Liouville equation for the system density matrix leads to a master equation[214,215]

$$\dot{P}_i(t) = -\sum_{j\neq i} k_{ij} P_i(t) + \sum_{j\neq i} k_{ji} P_j(t), \tag{5.7}$$

where $P_i(t)$ is the probability of finding the excitation on chromophore i at time t, and k_{ij} is the hopping rate constant for the energy transfer from chromophore i to j. Note that with this master equation, $S(t) = \langle P_i(t)\rangle_i$ given the initial condition $P_i(0) = 1$. In the context of our exciton Hamiltonian (Eq. (2.22)) and our mixed quantum/classical approach, the hopping rate constant k_{ij} can be expressed as[215,217,230]

$$k_{ij} = 2\mathrm{Re}\int_0^\infty dt \left\langle \omega_{ij}(t)\omega_{ij}(0) e^{i\int_0^t d\tau(\omega_i(\tau)-\omega_j(\tau))} \right\rangle, \tag{5.8}$$

where ω_{ij} is either intramolecular or intermolecular coupling between chromophores i and j, and the brackets indicate a time average over the trajectory. Note that since the bath is treated classically, we have $k_{ij} = k_{ji}$.

In principle, we can evaluate the hopping rate for each pair in the system (about 0.4 million pairs in a 432-molecule simulation box), but it is not practical (and not necessary) to do so. Instead, we rewrite Eq. (5.8) as

$$k_{ij} = 2\mathrm{Re}\int_0^\infty dt\, e^{i\langle\omega_i\rangle - \langle\omega_j\rangle t} \left\langle \omega_{ij}(t)\omega_{ij}(0) e^{i\int_0^t d\tau(\delta\omega_i(\tau)-\delta\omega_j(\tau))} \right\rangle, \tag{5.9}$$

where $\langle\omega_i\rangle$ is the time-averaged transition frequency of chromophore i, and $\delta\omega_i(\tau) \equiv \omega_i(\tau) - \langle\omega_i\rangle$. Then we assume that the quantity in brackets in Eq. (5.9) is the same for all the pairs

belonging to a given class of donor-acceptor pairs. With this assumption, we obtain

$$k_{ij}^{c} = \hat{B}^{c}(\langle\omega_i\rangle - \langle\omega_j\rangle), \tag{5.10}$$

where the superscript c indicates the pair of chromophores i and j belongs to the class c of donor-acceptor pairs, $\hat{B}^{c}(\omega) = \int_{-\infty}^{\infty} dt\, e^{i\omega t} B^{c}(t)$, and $B^{c}(t)$ is defined as

$$B^{c}(t) = \left\langle \omega_{ij}(t)\omega_{ij}(0) e^{i\int_0^t d\tau(\delta\omega_i(\tau) - \delta\omega_j(\tau))} \right\rangle_{c}. \tag{5.11}$$

The brackets with the subscript c indicate a time average over the trajectory as well as an average over the pairs of class c. Note that as it is mentioned in the previous chapter and will be elaborated further in the next chapter, ice Ih has static structural inhomogeneity due to the proton disorder so that the time-averaged frequency difference between chromophores i and j (that is $\langle\omega_i\rangle - \langle\omega_j\rangle$) is not necessarily zero for each pair. Therefore, Eq. (5.10) takes this static inhomogeneity into account. Thus, the hopping rate between chromophores i and j can be evaluated as the Fourier transform of the time correlation function in Eq. (5.11) at their time-averaged frequency difference.

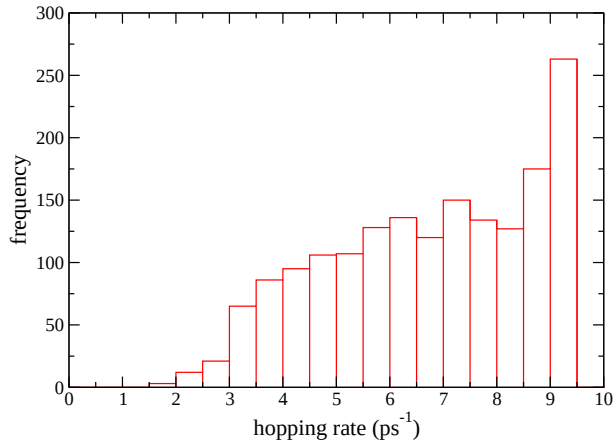

Figure 5.5: The histogram of the hopping rates between the intermolecular pairs of S class, calculated from Eq. (5.10).

In Fig. 5.5, we show the histogram of the hopping rates for all the S pairs (1728 pairs) in the system, calculated from Eq. (5.10). The majority of the S pairs have the hopping rates close to 9.2 ps^{-1}, which corresponds to zero time-averaged frequency difference. However, the static inhomogeneity indeed spreads out the distribution of the hopping rates in Fig. 5.5. To check the accuracy of Eq. (5.10), we calculate the hopping rates "exactly" from Eq. (5.8) for all the S pairs, and the mean relative absolute error is 11%. Also, we verify that this error for the S pairs does not bring much difference in the survival probability, calculated by solving the master equation numerically. The hopping rates between the pairs of other classes are also calculated from Eq. (5.10). In Fig. 5.3, the solid red line is the calculated survival probability based on solving the master equation numerically using Eq. (5.10). A significant underestimation of the survival probability is observed compared to the "exact" calculation (solid black line), implying that the incoherent hopping is not a proper picture for resonant OH vibrational energy transfer in ice Ih. Also, the recurrence is absent in the result from solving the master equation (solid red line). Therefore, the resonant OH vibrational energy transfer has some coherent features at least up to 300 fs. The validity of the incoherent hopping model hinges on the assumption that the dephasing rate caused by the bath fluctuation is much faster than the resonant energy transfer rate.[215,235] (A more straightforward way to understand this is that the system-bath coupling has to be much larger than the inter-chromophoric coupling for the incoherent hopping model.) However, this is not the case for the OH stretch in ice Ih, for which the resonant energy transfer is also ultrafast within 100 fs (the intermolecular coupling of S pairs is comparable to the system-bath coupling in magnitude). Since Förster theory is an approximate way to solve the master equation,[230] it is not appropriate to apply Förster theory directly to understand the resonant OH vibrational energy transfer in ice Ih.

Even though the incoherent hopping model is not correct here, the hopping rate constants are still helpful for recognizing the important donor-acceptor pairs in the system. Therefore, we calculate the average hopping rates for the pairs of a given class c as follows

$$\langle k \rangle_c = 2\mathrm{Re} \int_0^\infty dt \left\langle \omega_{ij}(t)\omega_{ij}(0) e^{i\int_0^t d\tau(\omega_i(\tau)-\omega_j(\tau))} \right\rangle_c , \tag{5.12}$$

where $\langle k \rangle_c$ is the average hopping rate over the trajectory and the sub-ensemble of the donor-acceptor pairs of class c. The average hopping rates for all the seven classes of pairs are shown in Table 5.1. The average hopping rate for S pairs is one order of magnitude larger than those for

other pairs, and 6.73 ps^{-1} agrees with the value (1/140 fs^{-1}) estimated by Timmer and Bakker.[31] This explains why including only the S pairs is sufficient to get the survival probability semi-quantitatively correct (Fig. 5.3). The hopping rates of other pairs are all less than 1.00 ps^{-1}, and the second largest hopping rate is from WII pairs as expected. The hopping rates for W0, intra, W60 pairs are of the same order of magnitude as that for WII pairs, and other pairs are not efficient energy transfer pairs. Note these results agree with the six-nearest-neighbor idea, suggested by Timmer and Bakker, though their treatment of the intramolecular couplings is not adequate as they assumed the dipolar coupling form for them.[31] Another point of interest to investigate here is the effect of the static inhomogeneity on the energy transfer process. We assign the average hopping rate of a class (Table 5.1) to all the pairs in that class, and solve the master equation (Eq. (5.7)) numerically to obtain the survival probability, shown as the solid green line in Fig. 5.3. The difference between the solid red and green lines is essentially negligible, indicating that the static structural inhomogeneity due to the proton disorder has little effect on the energy transfer. This is because the time-averaged frequency differences between chromophores in ice Ih are small, and the overlap of the absorption line shapes for the donor and acceptor is dominated by the homogeneous broadening in the context of the Förster theory, which has been discussed by Rosenfeld and Fayer recently.[236]

donor-acceptor pair class	average hopping rates (ps^{-1})
S (red-green)	6.73
WII (red-orange)	0.77
Intra (red-purple)	0.36
W0 (not shown)	0.64
W60 (red-yellow)	0.31
W120 (red-yellow)	0.05
W180 (red-yellow)	0.02
Other (red-white)	0.002

Table 5.1: Average hopping rates for different donor-acceptor pairs calculated from Eq. (5.12). The color pairs in the parentheses correspond to the pairs of the color-coded hydrogen atoms in Fig. 5.2.

Finally, we can discuss the time scale and length scale of the energy transfer in neat H_2O ice Ih. For simplicity, we assume the OH vibrational excitation locates on the hydrogen atoms. To examine the delocalization of the excitation, we define a root mean square displacement (RMSD) for the excitation, given by[237]

$$\mathrm{RMSD}(t) = \sqrt{\left\langle \sum_j |\vec{r}_j(t) - \vec{r}_i(0)|^2 |U_{ji}(t)|^2 \right\rangle_i}, \tag{5.13}$$

where $\vec{r}_j(t)$ is the position vector of the hydrogen atom of chromophore j at time t. If there is no energy transfer, the RMSD reflects the diffusion of the hydrogen atom in ice. As a result, Eq. (5.13) is the generalized RMSD with the energy transfer included. The calculated RMSD is plotted in Fig. 5.6, with the H-H radial distribution function (RDF) to its left (the intramolecular hydrogen peak is not shown) and the anisotropy decay below it. It is clear that the excitation is delocalized to the nearest chromophores of the initially excited chromophore on its neighbor molecules (the position of the chromophore is taken to be on the hydrogen atom) through the intermolecular couplings of S pairs within 100 fs, causing the anisotropy decay to fall below 0.1. At about 200 fs, the excitation has been transported to the second solvation shell of the central molecule, and the anisotropy decay has almost vanished. Considering that the donor-acceptor pairs of the S class are much more efficient than other pairs in transferring the OH vibrational energy and that the excitation is transported between the solvation shells almost at an equal time interval (100 fs), we speculate that the vibrational excitation is mainly transferred stepwise through the intermolecular couplings of S pairs in ice Ih, with a diffusion rate of about one solvation shell every 100 fs. To verify this, we calculate the RMSD of the excitation with only the intermolecular couplings of S pairs included in the Hamiltonian, shown as the red solid line in the top right panel of Fig. 5.6. Indeed, the S pairs account for the largest part of the OH resonant vibrational energy transfer in ice Ih. Another noteworthy observation in Fig. 5.6 is that up to 50 fs the RMSD is roughly linear in time, which is a signature of coherent energy transfer.[238–240]

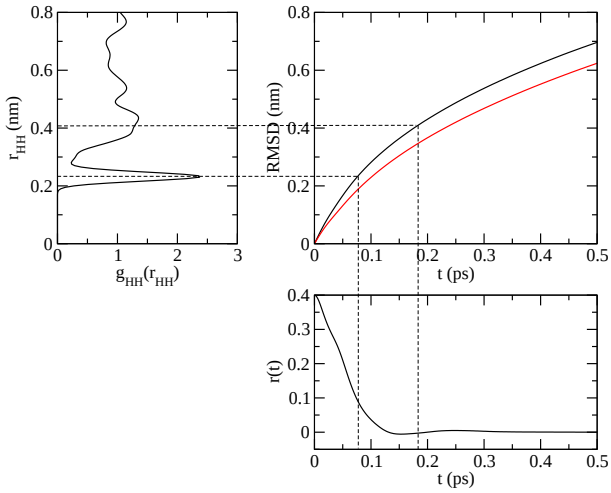

Figure 5.6: RMSD of the OH vibrational excitation in neat H_2O ice Ih. The black solid line in the top right panel is the RMSD of the excitation calculated from Eq. (5.13), the top left panel is the H-H radial distribution function, and the bottom right panel is the "exact" anisotropy decay from Eq. (5.2). The vertical dashed lines indicate the time scale of the excitation spreading, and the horizontal dashed lines indicate the corresponding length scale. The red solid line in the top right panel is the RMSD of the excitation with only the intermolecular couplings of S pairs in the Hamiltonian.

5.5 Concluding Remarks

In this chapter, we simulated the vibrational pump-probe anisotropy decays with the mixed quantum/classical approach for neat H_2O ice Ih and mixtures with deuterium substitution, and the agreement between theory and experiment is fairly good. By calculating the survival probability, we find the resonant OH vibrational energy transfer in ice Ih has coherent characteristics up to about 300 fs for neat H_2O, so that the incoherent hopping model cannot describe this process appropriately, not to mention the Förster theory. From the analysis of our theoretical model, we are able to interpret some features in the experimental anisotropy decay: (1) the rapid initial decay mainly arises from the fast resonant energy transfer for high hydrogen mole fractions; (2) the end levels reflect the level of the delocalization of the excitation at different hydrogen

mole fractions; (3) the oscillations are attributed to mainly the hindered rotation of the water molecules, and in part to the coherent characteristics of the energy transfer. We also find that the dominant donor-acceptor pairs in the energy transfer process are the nearest intermolecular pairs of OH chromophores (S pairs). For neat H_2O, the OH vibrational excitation is transferred to the first solvation shell of the initially excited molecule mostly through the S pairs on the time scale of 100 fs, and is subsequently transferred to further solvation shells in a stepwise manner through the S pairs. It is also shown that the static inhomogeneity due to the proton disorder in ice Ih has little effect on the energy transfer process. Given all this, we answer the question raised in the introduction by asserting that the resonant OH vibrational energy transfer in ice Ih (coherent) is qualitatively different from that in liquid water (incoherent) on the time scale of pump-probe experiments.

Chapter 6

Proton Disorder: Inhomogeneous Broadening

Contents

The content of this chapter corresponds to Ref. 241. Reprinted with permission from J. Phys. Chem. B 117, 15536 (2013); copyright 2013 American Chemical Society. We thank Dr. Fivos Perakis and Prof. Peter Hamm for sending their raw experimental data, and for helpful correspondence.

6.1 Introduction

In the previous two chapters, we have mentioned the structural heterogeneity due to the proton disorder in ice Ih, and its effect on linear spectra and vibrational energy transfer. This structural heterogeneity gives rise to different time-averaged transition frequencies for different OH

(OD) chromophores in ice Ih due to their slightly different local environments, and the resulting line shape broadening in the linear spectra is often called inhomogeneous broadening (the corresponding line-width is called inhomogeneous line-width). Therefore, understanding inhomogeneous broadening is particularly important because it provides an experimental window for understanding proton disorder. In this chapter, we focus primarily on this inhomogeneous broadening.

As discussed extensively in Chapter 4, vibrational coupling will further broaden vibrational spectra for ice Ih, making the spectral interpretation difficult. Therefore, a desirable system to understand the inhomogeneous broadening is an isotope-diluted ice Ih sample, such as dilute HOD in D_2O (HOD/D_2O for short),[26–28] for which the local OH stretch is essentially a normal mode of the system due to the large frequency mismatch between OH and OD stretches. Unlike the situation for neat H_2O, the IR spectrum for dilute OH consists of a single peak. The width of this peak is temperature dependent, ranging from about 125 cm^{-1} near the melting point to about 65 cm^{-1} at 86 K.[35] Note, however, that one experiment at 70 K has a line-width below 50 cm^{-1}.[185] Raman spectra have been measured down to lower temperatures, in one case finding a line-width as small as 25 cm^{-1} at 10 K.[186]

One can then ask: what fraction of the line-width is due to inhomogeneous broadening, and what fraction is due to homogeneous broadening, in this case due to low-frequency vibrational modes (phonons) and the excited-state lifetime (T_1)? Note that the homogeneous broadening comes from the system-bath interaction (low-frequency modes lead to transient OH stretch frequency fluctuation, and they can also accept vibrational energy from the excited OH chromophore through vibrational energy relaxation). Therefore, the homogeneous line-width due to thermal fluctuation will be temperature dependent, while the temperature dependence of T_1 is very small.[242] In contrast, the nature and extent of proton disorder is essentially temperature independent,[12] so the observed strong temperature dependence of the line-width shows that it must have at least some homogeneous contribution. However, for temperatures much less than the Debye temperature (which for ice is approximately 226 K[7]), the homogeneous contribution from phonons should become unimportant.[243,244] Therefore, at 80 K one might expect that the line-width would be dominated by an inhomogeneous contribution from proton disorder, and a homogeneous contribution from the excited state lifetime. The latter is about 400 fs and roughly temperature independent,[242] which by itself would lead to a line-width of 13 cm^{-1}. A

convolution of a Lorentzian (i.e., homogeneous line shape) with this width, and a Gaussian (i.e., inhomogeneous line shape), suggests that the experimental width at 86 K of 65 cm^{-1} therefore has an inhomogeneous contribution with a width of 58 cm^{-1}. Li and Skinner have modeled the linear vibrational spectroscopy of the HOD/D_2O ice Ih system.[35] The calculated temperature-dependent IR line-widths are in reasonable agreement with experiment. The density of ice depends on temperature (it increases as T decreases),[7] and so even though the proton disorder is temperature independent, we found (see Fig. 12 in Ref. 35) that the inhomogeneous broadening is weakly temperature dependent, with widths ranging from 59 cm^{-1} at 245 K, to 63 cm^{-1} at 125 K, to 70 cm^{-1} at 1 K.[35] A simple interpolation suggests a theoretical inhomogeneous width of about 65 cm^{-1} at 80 K due to the proton disorder.

Recently, the emergence of ultrafast vibrational spectroscopy rendered the experimental extraction of the inhomogeneous width possible at relatively high temperature.[41] Graener and coworkers carried out a picosecond IR hole-burning experiment on HOD in D_2O ice Ih at 230 K in 1997.[245] They found an inhomogeneous width of $\sim$50 cm^{-1}, which they attributed to proton disorder. Another cutting-edge nonlinear technique is two-dimensional infrared spectroscopy (2DIR), which adds an additional frequency dimension to the linear IR, analogous to two-dimensional NMR.[246] If inhomogeneous broadening is dominant, the 2DIR spectrum will usually be elongated along the diagonal. If homogeneous broadening is dominant, the 2DIR spectrum will be more round. If both broadening mechanisms are important, the anti-diagonal line-width of the 2DIR spectrum will provide some information about the homogeneous broadening, while the diagonal line-width will reflect both broadening mechanisms.[246] A very recent 2DIR study on isotope-diluted ice Ih at 80 K by Hamm and coworkers showed even less inhomogeneous broadening in their 2DIR spectra as their 2DIR line shape looked round.[36,241]

To summarize, then, linear IR spectroscopy suggests that the inhomogeneous line-width in HOD/D_2O ice Ih at 86 K is about 58 cm^{-1}, hole-burning experiments at 230 K suggest an inhomogeneous width of about 50 cm^{-1}, 2DIR experiments at 80 K suggest probably an even smaller inhomogeneous width (probably less than 50 cm^{-1}), and theoretical calculations indicate an inhomogeneous width about 65 cm^{-1} at 80 K and 59 cm^{-1} at 245 K.

In this chapter, we will simulate the 2DIR spectrum for HOD/D_2O ice Ih at 80 K, and investigate how the 2DIR line shape changes with the amount of the inhomogeneous broadening due to the proton disorder. Moreover, we propose a potentially better way to examine this in-

homogeneous broadening. The rest of this chapter is organized as follows. In Section 6.2, we outline the methodology for calculating linear and 2DIR; in Section 6.3, we compare our calculated linear and 2DIR to experiment; in Section 6.4, we investigate the effect of inhomogeneous broadening on linear and 2DIR line shapes; in Section 6.5, we propose 3PEPS as a better way to examine this inhomogeneous broadening; in Section 6.6, we conclude.

6.2 Theoretical Method: 1D and 2DIR

As the OH chromophores of dilute HOD in D_2O are essentially isolated, ice Ih, Eq. (2.23) is greatly simplified, and the expression for the IR absorption spectrum for light with polarization $\hat{p}$ is given by[35]

$$I_p(\omega) \sim \text{Re} \int_0^\infty e^{i\omega t} \langle \mu_{10}^p(0) \mu_{10}^p(t) U_{10}(t) \rangle e^{-t/2T_1}, \tag{6.1}$$

where $U_{10}(t) = \exp\left[-i \int_0^t \omega_{10}(\tau) d\tau\right]$, $\omega_{10}(\tau)$ is the fluctuating 1-0 transition frequency of that OH stretch, and μ_{10}^p is the pth Cartesian component of the corresponding transition dipole (p is now a superscript). The phenomenological vibrational lifetime is $T_1 = 0.4$ ps for HOD in D_2O.[242]

In a typical time-domain 2DIR experiment, three ultrafast laser pulses are applied to interact with the sample, and the time delays between three pulses and the detected signal are denoted as t_1, t_2 and t_3; t_2 is often called the waiting time.[246] The time-domain signal is then tranformed to the frequency domain by performing Fourier transforms for t_1 and t_3. The resulting spectrum $S(\omega_3, t_2, \omega_1)$ is plotted as a two-dimensional coutour with ω_1 and ω_3 as the x and y axes, respectively (this is the convention we choose in this chapter). The 2DIR spectrum for an isotope-diluted system is more or less a correlation spectrum: the chromophore (e.g., OH stretch) is excited resonantly at a frequency of ω_1 (sometimes called the pump frequency), and after the waiting time t_2, it is probed to be vibrating at a frequency of ω_3 (sometimes called the probe frequency). If the molecular environment around that chromophore is basically unaltered during t_2, ω_3 will be highly correlated with ω_1, leading to a diagonally elongated 2DIR line shape (i.e., an inhomogeneously broadened line shape). In the other limit, when the molecular environment around that chromophore is changed drastically during t_2, ω_3 and ω_1 are uncorrelated, leading to a round 2DIR line shape (i.e., an homogeneously broadened line shape). Certainly, whether the line shape is dominated by inhomogeneous or homogeneous broadening

depends upon the waiting time t_2. By varying t_2, one can see how the 2DIR line shape changes with time due to the gradual loss of frequency correlation (sometimes called spectral diffusion), providing an estimate of the time scale for the fluctuation of the local environment around the chromophore. Therefore, 2DIR is powerful for understanding structural heterogeneity (from inhomogeneous broadening) as well as molecular dynamics (from spectral diffusion). Note that as 2DIR can access the second vibrational excited state (i.e., pump 1-0 transition, but probe 2-1 transition), peaks are shown as pairs in 2DIR spectrum, and the gap along the ω_3 axis between 1-0 (positive) and 2-1 (negative) peaks reflects the anharmonicity of the chromophore.

From a theoretical perspective, calculating the 2DIR line shape $S(\omega_3, t_2, \omega_1)$ is much more challenging than linear IR, requiring the calculation of the so-called third-order nonlinear response functions (at least six of them: $R_{1,2,3,4,5,6}(t_3, t_2, t_1)$). Within the mixed quantum/classical approach and delta-pulse approximation, the calculation is simplified; details are shown in Appendix A. For these calculations, we employ molecular dynamics simulations of D_2O at 80 K, the details of which are the same as in Section 4.2. To calculate spectra, we average over the putative substitution of each D with an H, and use the maps for OH spectroscopy.

6.3 Results and Comparison with Experiment

In Fig. 6.1, the experimental IR line shape for HOD/D_2O ice Ih at 80 K is plotted (black solid line).[36] This line shape is more or less consistent with older data,[35] although a bit broader (full-width-half-max (FWHM) is 79 cm^{-1}, compared to 65 cm^{-1} at 86 K[180]). The theoretical IR line shape at 80 K is also plotted (red solid line). It is in reasonable agreement with the experiment, although the calculated line shape is slightly red-shifted and narrower (FWHM of 75 cm^{-1}) compared to the experimental line shape (but 10 cm^{-1} broader than the older experiment). Both line shapes show a single peak with little if any structure.

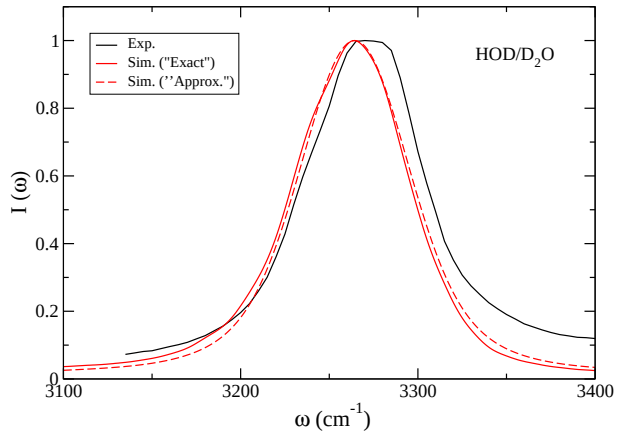

Figure 6.1: Calculated (from Eq. (6.1)) and experimental[36] infrared (IR) line shapes for HOD/D_2O ice Ih at 80 K. Note that the baseline of the original experimental spectrum[36] has been subtracted, and the absorbance is converted to the line-shape function. The red dashed line is the line shape for HOD/D_2O ice Ih with the approximate linear response function (from Eq. (A10)). All line shapes are normalized to have the same peak height.

Next, we consider the 2DIR spectra for HOD in D_2O ice Ih at 80 K. The experimental 2DIR spectra were reported in Refs. 36 and 241, and only the 2DIR spectrum with the waiting time $t_2 = 200$ fs is replotted in the right panel of Fig. 6.2 using the raw experimental data,[247] as the spectral diffusion is expected to be slow (the experimental spectrum at 100 fs suffers from a so-called "coherent artifact", and the spectrum at a long waiting time (t_2 = 1 ps) loses intensity because of VER). Note that this version of the 2DIR spectrum for HOD/D_2O ice Ih as it is an anisotropic 2DIR spectrum (i.e., $S_{\|} - S_{\perp}$),[241] which is discussed in Appendix B. The advantage of anisotropic 2DIR is that it suppresses the effects of the local heating on the spectrum, which might occur in $S_{\|}$ and $S_{\perp}$ in experiment (see the old spectrum in Ref. 36). The apparent anharmonicity (difference between the 1-0 and 2-1 peak maxima) in this spectrum is about 285 cm^{-1}. The 1-0 transition peak (red lobe) appears to be primarily homogeneously broadened (the diagonal elongation is small). The 2-1 transition peak (blue lobe) is much broader than 1-0 transition peak, which is also observed in the pump-probe[248] and hole-burning[245] experiments. If we compare the experimental HOD/D_2O 2DIR spectra for ice Ih to those for liquid water,[249] there are two major differences: (1) The 2DIR spectra for ice barely change with increasing

waiting time (at least for 1-0 transition peak, see t_2=200 fs and 500 fs in Fig. 2 of Ref. 36), while 2DIR spectra for liquid water becomes circular gradually;[250,251] (2) the 2DIR spectrum for ice is much narrower than that for liquid water.

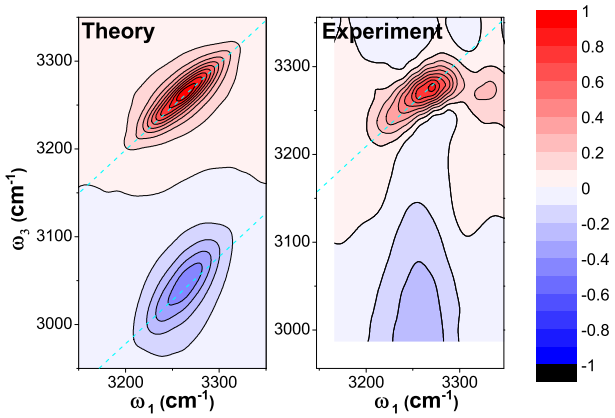

Figure 6.2: Calculated (from Eqs. (A2) - (A5) and (B3) for $S_{\|}$) and experimental[36] ($S_{\|} - S_{\perp}$) 2DIR spectra for HOD/D_2O ice Ih at 80 K (t_2=200 fs). The red lobe is the 1-0 transition peak associated with ground state bleach and stimulated emission processes, and the blue lobe is the 2-1 transition peak associated with the excited state absorption process. The spectra are normalized to have the same 1-0 transition peak height. The dashed line indicates the diagonal.

In Fig. 6.2, we also show our theoretical 2DIR spectrum ($t_2 = 200$ fs, parallel polarization geometry) for HOD/D_2O ice Ih at 80 K (left panel). Note that the calculated 2DIR is $S_{\|}$, as theoretically $S_{\perp} \approx S_{\|}/3$ for HOD/D_2O ice Ih (see Appendix B). Both the 1-0 and 2-1 transition peaks in our theoretical 2DIR spectrum are elongated along the diagonal (actually, along a line steeper than the diagonal for the 2-1 transition), indicative of substantial inhomogeneous broadening (more evident than in experiment). The frequency gap between the 1-0 and 2-1 peaks (apparent anharmonicity of 217 cm^{-1}) is smaller in our calculated 2DIR spectra compared to that in the experiment at this waiting time. Except for these issues, the agreement between the theoretical and experimental 2DIR for HOD/D_2O ice Ih is reasonable.

6.4 Discussion: Inhomogeneous Broadening

Each individual putative OH chromophore has a time-averaged frequency determined by its proton-disordered environment, and fluctuations about this average frequency due to thermal motion (phonons). The distribution of time-averaged frequencies represents the inhomogeneous broadening. For the 864 chromophores in our crystal at 80 K, this distribution is shown in Fig. 6.3 for both the 1-0 and 2-1 transition frequencies. The dashed lines are the best Gaussian fits for the histograms. The standard deviations are about 26 cm^{-1} and 32 cm^{-1}, for the 1-0 and 2-1 transitions respectively. The corresponding FWHM of the 1-0 distribution is about 62 cm^{-1}. This is few cm^{-1} less than the interpolated value of 65 cm^{-1} from the work by Li and Skinner;[35] this small discrepancy presumably arises because the earlier work used the first version of the E3B model.[83] Since the width of the theoretical absorption spectrum at 80 K is 75 cm^{-1}, this means that the line shape is dominated by inhomogeneous broadening.

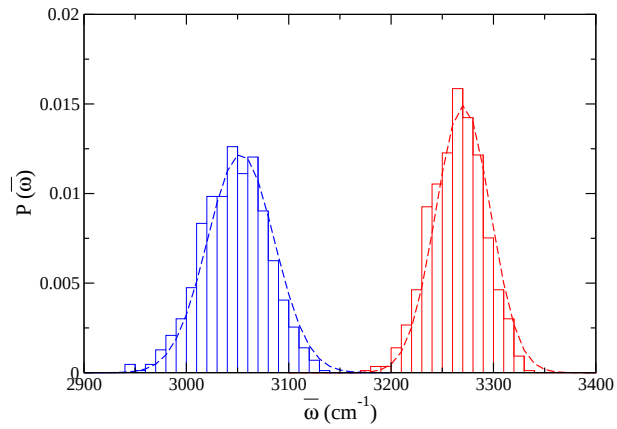

Figure 6.3: Histograms of time-averaged transition frequencies $\bar{\omega}$ for HOD/D_2O ice Ih at 80 K. The dashed lines are the best Gaussian fits. Red lines are for 1-0 transition frequency, and blue lines are for 2-1 transition frequency.

The inhomogeneous broadening of the 2-1 peak is larger than for the 1-0 peak, which is reflected in the wider peak in the theoretical 2DIR spectrum. The reason for the broader 2-1

distribution is that the OH-stretch potential curve in ice is very anharmonic, and the anharmonicity increases with the hydrogen bond strength.[78] Since the 1-0 and 2-1 frequencies are highly correlated, this also explains the steeper slope of the 2-1 transition peak in our theoretical 2DIR. It is worth mentioning that the large breadth of the 2-1 transition peak has been discussed extensively in some experimental studies, and many explanations have been conjectured, such as an asymmetric double well potential for the proton between two oxygen atoms,[245] vibrational energy relaxation of the second excited state through some intermediate states,[248] and the non-adiabatic coupling of the OH stretch with the quantal low-frequency modes.[36]

In order to understand the sensitivity of the 2DIR spectrum to the amount of inhomogeneous broadening, it is convenient to derive some approximate expressions for the response functions. Basically, we make the Condon approximation, neglect the rotational dynamics of the chromophores, make the Gaussian approximation for the inhomogeneous broadening, make the cumulant approximation for the frequency fluctuations of each chromophore, and assume that the frequency time-correlation function for each chromophore is the same. The details are described in Appendix A. In turns out that these approximations all work well (compared to the "exact" theoretical results) for ice (although most of them do not work at all well for liquid water). To show this, in Fig. 6.1 we plot the approximate result using Eq. (A10) for the absorption spectrum (red dashed line), and in Fig. 6.4 we plot the approximate result using Eq. (A12) for the 2DIR spectrum for HOD/D_2O ice Ih. In both cases comparison with the exact theoretical results is excellent.

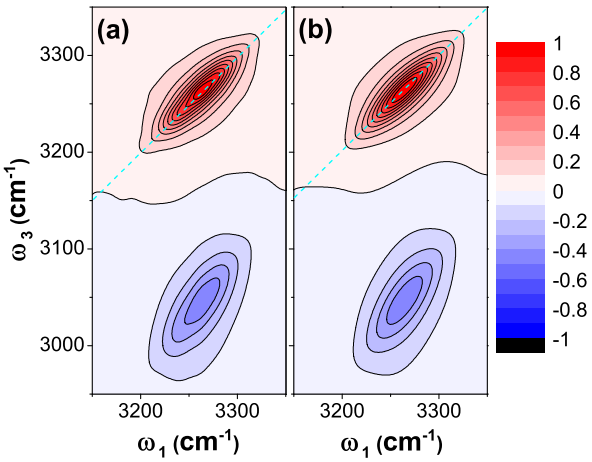

Figure 6.4: Calculated 2DIR spectra for HOD/D_2O ice Ih at 80 K (t_2=200 fs): (a) "exact" spectrum with the exact 3rd-order response functions in Eq. (A2), identical to the left panel in Fig. 6.2; (b) approximate spectrum with the approximate 3rd-order response functions in Eq. (A12).

Our approximate expressions involve the variances of the time-averaged frequency distribution for the 1-0 transition, σ_1^2, the 2-1 transition, σ_3^2, and the covariance, σ_2^2, as defined in Appendix A. For the sake of argument and illustration, we can artifically decrease σ_1, σ_2, and σ_3, to see the effect on the 1D and 2DIR spectra. We consider three cases: where these values are decreased by 1/3, decreased by 2/3, and set to 0. The results for the 1D spectrum are shown in Fig. 6.5. All three of these new spectra are quite a bit too narrow and not consistent with the experiment by Hamm and coworkers[36] (note that their IR spectrum is a bit broader than that in a previous study at 86 K[180]). The results for the 2DIR spectra are shown in Fig. 6.6. Here we see that the result with the inhomogeneous broadening decreased by 1/3 in panel (c) is perhaps in best agreement with experiment. Indeed, this would give an inhomogeneous width of about $62 \times 2/3 = 42$ cm^{-1} for the 1-0 transition, consistent with our estimate (less than 50 cm^{-1}) based on the experimental spectrum.

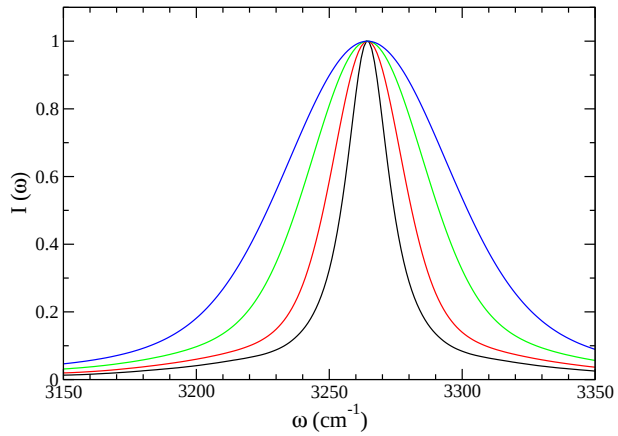

Figure 6.5: Absorption line shapes with full inhomogeneous broadening (blue), reduced by 1/3 (green), reduced by 2/3 (red), and set to 0 (black).

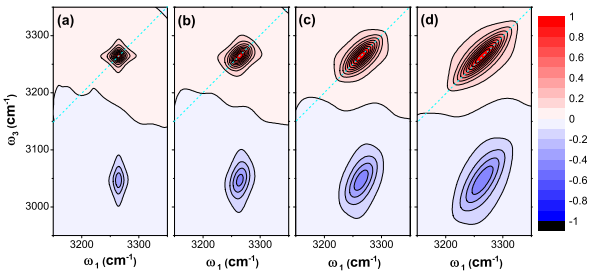

Figure 6.6: Calculated 2DIR spectra for HOD/D_2O ice Ih at 80 K (t_2=200 fs) with the approximate 3rd-order response functions in Eq. (A12), and inhomogeneous broadening due to the proton disorder (σ_a, $a = 1, 2, 3$): (a) set to 0; (b) reduced by 2/3; (c) reduced by 1/3; (d) kept in full, identical to Fig. 6.4(b).

This leaves the rather uncomfortable situation where our model results are consistent with the experimental 1D but not the 2D spectrum, whereas if we decrease the inhomogeneous broadening by 1/3 our results are consistent with the 2DIR but not the 1D experiments. If we consider, for the moment, reasons why our theoretical inhomogeneous broadening could be too large, the most likely candidate is the accuracy of our frequency map for ice. After all, the map was parameterized for liquid water. However, we have recently compared our map to DFT calculations from ice configurations, and while there is a small more or less uniform frequency shift from the ice results to the map, the slope of the map (versus electric field) and slope of the ice points are about the same, and therefore the amount of inhomogeneous broadening would be unchanged.[78] To reiterate, the slope of the map reflects the dispersion in the frequencies for different electric fields, and so two maps with the same slope would have the same width in the frequency distribution. Decreasing the inhomogeneous broadening by 1/3 is equivalant to decreasing the slope of the map by 1/3, which is incompatible with the DFT calculations.[78] Therefore, in the next section, we propose the vibrational three-pulse photon-echo peak-shift (3PEPS) experiment as a better way to estimate this inhomogeneous broadening as well as to probe low-frequency dynamics in ice.

6.5 Proposed Experiment: 3PEPS

Ultrafast spectroscopy of liquid HOD/D_2O has shown that the 3PEPS experiment actually leads to higher resolution dynamical information than does the 2DIR (3PEPS shows the oscillation due to the hydrogen bond stretch for liquid water, where 2DIR does not).[252] In fact, at "long" times the peak shift can be shown to be proportional to the frequency-frequency time-correlation function,[253–256] which is the object of primary theoretical interest. For ice the theoretical phonon contribution to the frequency-frequency time-correlation function ($C_1(t)$, see Eq. (A9)) is shown in Fig. 6.7. It shows pronounced structure indeed, reflecting the various low-frequency modes of the system.

In the vibrational 3PEPS measurement, a series of time-integrated three-pulse photon-echo measurements with different waiting times are taken. In the impulsive limit, the integrated photon echo intensity is given by[257]

$$I(t_2, t_1) = \int_0^\infty dt_3 \left| \sum_{m=1}^{3} R_m(t_3, t_2, t_1) L_m(t_3, t_2, t_1) \right|^2 , \tag{6.2}$$

where R_m and L_m are defined in Appendix A. The peak shift $t_1^*(t_2)$ is defined by[256]

$$\left. \frac{\partial I(t_2, t_1)}{\partial t_1} \right|_{t_1 = t_1^*(t_2)} = 0. \tag{6.3}$$

As the approximate third-order response functions (Eq. (A12)) perform very well in the calculation of the 2DIR spectrum (Fig. 6.4), we again use them to calculate the 3PEPS signal. In order to get a smooth 3PEPS curve, we increase the resolution of the time-correlation functions to 0.1 fs using the cubic spline interpolation method.[258] The calculated 3PEPS signal is shown in Fig. 6.7(b), and we see that it does show similar structure as the time-correlation function itself in panel (a).

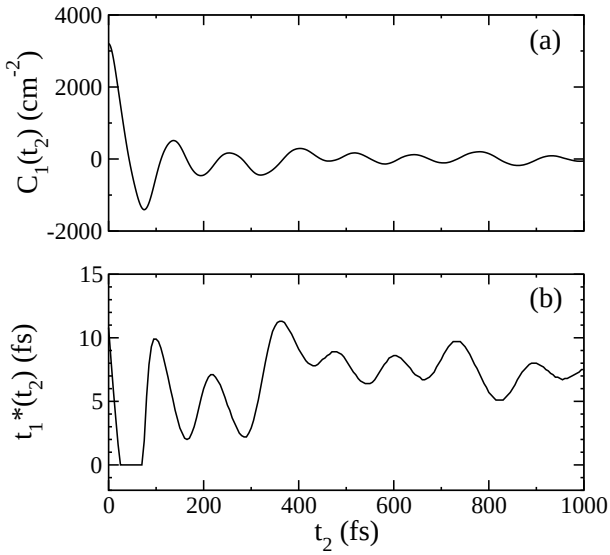

Figure 6.7: (a) Time-correlation function for the dynamic fluctuations; (b) Calculated vibrational three-pulse photon echo peak shift (3PEPS) (from Eqs. (6.2) and (6.3)) for HOD/D_2O ice Ih at 80 K with the approximate 3rd-order response functions in Eq. (A12).

Another interesting feature of the theoretical 3PEPS signal is that it does not decay to 0 as t_2 gets large. In fact, as mentioned above we have previously shown[256] that at long times the peak shift is related to the frequency-frequency time-correlation function, but for ice the full time-correlation function does not decay to zero (as in Eq. (A9)). In Appendix C we show that under certain conditions

$$t_1^*(\infty) = T_p\sigma_1^2/(\sigma_1^2 + C_1(0)), \tag{6.4}$$

where σ_1 and $C_1(0)$ are defined in Appendix A, and T_p is defined in Appendix C. The value of $t_1^*(\infty)$ from Fig. 6.7 is about 7.5 fs, compared to 11.1 fs from the above. In any case, since $t_1^*(\infty)$ depends on the amount of inhomogeneous broadening, σ_1, it may well be an interesting quantity to measure in experiment.

6.6 Concluding Remarks

OH (OD) stretch vibrational spectroscopy has been used to study the microscopic structure of ice Ih for almost a century. However, the presence of a spectral signature of proton disorder is

still controversial, even with the power of nonlinear spectroscopy. In this work, we attempt to deepen our understanding of this issue by calculating 2DIR spectra for HOD/D_2O ice Ih with our mixed quantum/classical approach. Our calculated 2DIR line shape shows evident inhomogeneous broadening, which is not very pronounced in the experimental line shape, while our calculated linear IR spectrum is in good agreement with the experiment at the same temperature. We explore the effect of inhomogeneous broadening due to the proton disorder on the 2DIR line shapes. If the amount of inhomogeneous broadening is reduced, the model becomes compatible with the 2DIR spectrum, but incompatible with the 1DIR spectrum. This situation is not satisfactory, and further experimental and theoretical work needs to be done to resolve this controversy. As a possible experiment to probe low-frequency dynamics in ice, and also to study inhomogeneous broadening further, we encourage experimenters to perform a 3PEPS experiment. To this end, we have presented a theoretical calculation of such.

Chapter 7

Vibrational Dynamics: Incoherent Inelastic Neutron Scattering

Contents

7.1 Introduction

In the previous several chapters, we have discussed vibrational spectroscopy with photons (e.g., IR and Raman). Although these optical techniques are very useful in probing structure and dynamics in condensed phases, they still have some limitations:[259] for instance, the sample usually has to be optically transparent or thin as photons often do not penetrate deeply into materials; optical spectroscopy is usually subject to the optical selection rules so that spectra do not necessarily reflect the vibrational density of states in the system; successful theoretical modeling of these optical spectra requires not only a good description of inter-atomic potential energy

surface, but also a reliable reproduction of other quantities (for IR, dipole moment surface or transition dipole moment); and last but not least, if there are many degenerate chromophores in the system (e.g., OH stretches in neat H_2O), these chromophores can interfere "coherently" due to vibrational coupling, further complicating the spectra.

Over the past fifty years, vibrational spectroscopy with neutrons has been an alternative method to optical vibrational spectroscopy for investigating the structure and dynamics of condensed phases. Neutrons, which carry almost the same mass as hydrogen atoms, can penetrate deeply into most bulk materials and interact primarily with nuclei (especially hydrogen), making neutron vibrational spectroscopy a natural choice to probe nuclear arrangement and motions.[259] Furthermore, coherent and incoherent contributions to neutron scattering can be measured separately. As the de Brogile wavelength of a thermal neutron is close to interatomic distances, coherent (inelastic) neutron scattering is widely used to determine radial distribution functions for condensed phases.[29,260] Meanwhile, if the energy of the incident neutron is comparable to molecular vibrational energies, incoherent (inelastic) neutron scattering enable experimentalists to extract vibrational density of states directly.[37,259] In this chapter, we will focus on incoherent inelastic neutron scattering.

Nowadays, neutron spectrometers can cover the whole infrared region for typical molecular (fundamental) vibrations (i.e., 0-4000 cm^{-1}).[259,261,262] As the incoherent scattering cross section of hydrogen atom (80.3 barn) is at least one order of magnitude larger than that of any other atom including deuterium (5.6 barn),[261] the incoherent inelastic neutron scattering (IINS) spectra of hydrogen-containing materials are dominated by scattering from hydrogen atoms, making IINS a good probe for vibrations involving hydrogen motions (e.g., OH stretch, hydrogen-bond stretch).[259,261] In fact, hydrogen bonding in various phases of ice (e.g., Ih, Ic, II, V, VI, VII, VIII, IX, XI, and amorphous ices) has been studied experimentally by IINS (typically below 1000 cm^{-1}),[173,176,201,203,205,263–266] and many theoretical methods have been scrutinized against these experimental IINS spectra.[172,177,204,267–276] Due to the availability of higher energy neutrons (above 1000 cm^{-1}), IINS spectra for OH stretch have also been measured and analysed to understand hydrogen-bonding in condensed phases, just like OH-stretch IR and Raman spectra. Recent IINS spectral analysis has triggered a debate in the literature[277–283] on the existence of another water anomaly: an excess of proton mean kinetic energy in supercooled water. Moreover, one recent study[283] suggests a very counter-intuitive view that the hydrogen bond might

be weaker in ice than that in supercooled water at similar temperatures. Clearly, the resolution of these controversial issues needs further experimental and especially theoretical studies.

The formal theory for incoherent neutron scattering was developed right after the IINS experiments were achievable.[38,40,284–286] There are two basic methods for treating IINS spectra of condensed phases: one is a phonon approach, which is primarily applied to solids; the other is based on time-correlation functions (TCFs), and can be applied to both solids and liquids.[38–40] In this chapter, we adopt the second approach as both liquid and solid water will be discussed here. The key quantity to calculate IINS spectra is a TCF shown in the last row of Table 2.1. If we consider the low-frequency IINS (below 1000 cm^{-1}) of water, this TCF can be evaluated readily from molecular dynamics simulations as discussed in Section 2.4 and Chapter 3.[267,269,287] If the modeling of nuclear quantum effects is desired, a quantum correction factor can be applied, and there are also existing approaches in the literature to calculate this quantum TCF directly.[288–291] For the OH-stretch IINS of water, a mixed quantum/classical approach is highly desirable, and we are aware of the theoretical works only by Bratos and coworkers in this direction.[292–295] However, their method requires the input of empirical parameters. Therefore, in this chapter we extend our mixed quantum/classical approach to the calculation of OH IINS spectra for water. The rest of the chapter is organized as follows. In Section 7.2, the theoretical methodology for calculating IINS is outlined; in Section 7.3, we compare our calculated OH IINS for liquid water, supercooled water and ice Ih to experiment, and make connections to OH IR spectra; in Section 7.4, the calculated low-frequency IINS spectra for these systems are presented and compared to experiment; in Section 7.5, hydrogen bonding in these systems is discussed in the context of our calculations; in Section 7.6, we conclude.

7.2 Theoretical Method: IINS

For H-containing systems like water, the IINS cross section is dominated by hydrogen, as its scattering cross section is much larger than those of other atoms including deuterium. It is thus a rather good approximation to only consider the scattering due to hydrogen in the IINS calculation for water. Assuming the first Born approximation and Fermi pseudopotential between the incident neutron and the scattering atom (e.g., hydrogen), the IINS double differential cross section is proportional to the incoherent scattering function (sometimes also called incoherent

dynamical structure factor), given by[37]

$$S(\vec{k},\omega) = \frac{1}{2\pi}\int_{-\infty}^{\infty} dt e^{-i\omega t} I(\vec{k},t), \tag{7.1}$$

where $\vec{k}$ is the momentum transferred during the scattering, and $I(\vec{k},t)$ is the incoherent intermediate scattering function, defined by[37]

$$I(\vec{k},t) = \left\langle e^{-i\vec{k}\cdot\vec{r}_j(0)} e^{i\vec{k}\cdot\vec{r}_j(t)} \right\rangle, \tag{7.2}$$

where the brackets denote an equilibrium quantum-mechanical ensemble average and an average over all hydrogen atoms in the system (see Section 2.1 and Table 2.1), and $\vec{r}_j(t)$ is the time-dependent position operator associated with the jth hydrogen in the Heisenberg picture. Note that $I(\vec{k},t)$ can also be expressed as follows

$$I(\vec{k},t) = \int_{-\infty}^{\infty} d\omega e^{i\omega t} S(\vec{k},\omega). \tag{7.3}$$

These two equivalent ways of writing $I(\vec{k},t)$ lead to a very useful relation between the experimentally measurable incoherent scattering function and the microscopic velocity TCF for isotropic systems, given by

$$\lim_{k\to 0} \frac{\omega^2}{k^2} S(\vec{k},\omega) = \frac{1}{6\pi} f(\omega), \tag{7.4}$$

where $k = |\vec{k}|$, and $f(\omega)$ is the Fourier transform of the velocity TCF mentioned in Chapter 3, given by

$$f(\omega) = \int_{-\infty}^{\infty} dt e^{i\omega t} \langle \vec{v}(t)\cdot\vec{v}(0)\rangle. \tag{7.5}$$

A proof of Eq. (7.4) is given in Appendix D.

As the velocity TCF can be calculated easily from molecular dynamics simulations, IINS provides a route to a direct comparison between theory and experiment in terms of molecular dynamics. Moreover, for a harmonic system (e.g., molecular vibrations in ice Ih at low temperatures), one can show that this $f(\omega)$ is identical with the phonon density of states (i.e., the frequency distribution of the normal modes),[38,286] which might be obtained from lattice dynamics calculations or electronic structure methods. Therefore, a new quantity is often defined in

the literature

$$G(\vec{k},\omega) \equiv \frac{\omega^2}{k^2} S(\vec{k},\omega), \tag{7.6}$$

which is sometimes called k-dependent proton density of states. For low-frequency IINS (i.e., below 1000 cm^{-1}), $f(\omega)$ might be directly evaluated from classical MD simulations (see Section 2.4), sometimes with an additional quantum correction factor.[58]

For high-frequency IINS (e.g., OH stretch), as in the case of IR and Raman, quantum mechanics is essential. As mentioned in Section 2.5.1, mixed quantum/classical approaches are particularly attractive in dealing with high-frequency vibrations in condensed phases, and in the rest of this section, our mixed quantum/classical approach is applied to calculate OH stretch IINS. In order to keep our convention consistent, we consider a time correlation function $C(\vec{k},t) = I(\vec{k},-t)$ so that

$$C(\vec{k},t) = \left\langle e^{-i\vec{k}\cdot\vec{r}_j(t)} e^{i\vec{k}\cdot\vec{r}_j(0)} \right\rangle, \tag{7.7}$$

and $I(\vec{k},t) = C^*(\vec{k},t)$. Recalling the general discussion in Section 2.5.1, $C(\vec{k},t)$ can be evaluated using our mixed quantum/classical approach (see Eq. (2.23)), and we need to evaluate transition moments, such as $\langle 0| e^{-i\vec{k}\cdot\vec{r}_j(t)} |l\rangle$ (l is used here as a system state index instead of i for the avoidance of confusion with the imaginary unit). Note that the position operator within the system-bath treatment can be written as $\vec{r}_j(t) = \vec{R}_j(t) + \vec{q}_j(t)$, where $\vec{R}_j(t)$ is the equilibrium position of hydrogen atom regarding OH stretch (i.e., $\vec{R}_j(t) = \langle 0| \vec{r}_j(t) |0\rangle$), and can be obtained from classical MD simulations. The remaining $\vec{q}_j(t)$ is the vibrational displacement of hydrogen atom from its equilibrium position during the OH stretch. If we consider that the vibrational coordinate x of OH stretch is dominated by hydrogen atom displacement, we have approximately $\vec{q}_j(t) \approx x_j(t)\hat{u}_j(t)$, where $\hat{u}_j(t)$ is taken to be the jth OH bond unit vector. Now we have

$$\langle 0| e^{-i\vec{k}\cdot\vec{r}_j(t)} |l\rangle \approx e^{-i\vec{k}\cdot\vec{R}_j(t)} \langle 0| e^{-ikx_j(t)(\hat{\epsilon}\cdot\hat{u}_j(t))} |l\rangle, \tag{7.8}$$

where $\hat{\epsilon} \equiv \vec{k}/k$. It would be desirable to have a "map" for $\langle 0| e^{-ikx(\hat{\epsilon}\cdot\hat{u})} |1\rangle$, but this is not easy to obtain. We have two approaches to proceed given the maps in Table 2.2. One is to make a harmonic approximation for the oscillators, which is not particularly good for OH stretch. For a harmonic oscillator, $\langle 0| x^n |1\rangle$ is equal to $(\langle 0| x |1\rangle)^n$ for odd n, and otherwise zero. Therefore, $\langle 0| e^{-ikx(\hat{\epsilon}\cdot\hat{u})} |1\rangle$ can be evaluated by Taylor expansion. Alternatively, as we

are only interested in the limit $k \rightarrow 0$, we can simply truncate $\langle 0| e^{-ikx(\hat{\epsilon}\cdot\hat{u})} |1\rangle$ at the first order in its Taylor expansion. This approximation is what we take in this chapter, and we have $\langle 0| e^{-ikx_j(t)(\hat{\epsilon}\cdot\hat{u}_j(t))} |l\rangle \approx -ikx_{01,j}(t)(\hat{\epsilon}\cdot\hat{u}_j(t))\delta_{jl}$, where $x_{01,j}(t) \equiv \langle 0| x_j(t) |j\rangle$. Now, the incoherent intermediate scattering function for small k values is approximated by

$$I(\vec{k},t) \approx \left\langle e^{-i\vec{k}\cdot(\vec{R}_j(0)-\vec{R}_j(t))} k^2 m_{01,j}(0) U^*_{jj}(t) m_{01,j}(t) \right\rangle_b, \tag{7.9}$$

where $m_{01,j}(t) \equiv (\hat{u}_j(t)\cdot\hat{\epsilon})x_{01,j}(t)$, and the brackets with the subscript b denote ensemble averages over the bath and the OH chromophores in the system.

Finally, in the limit $k \rightarrow 0$ we have

$$G_0(\hat{\epsilon},\omega) \equiv \lim_{k\rightarrow 0} G(\vec{k},\omega) \approx 2\omega^2 \mathrm{Re} \int_0^\infty dt e^{i\omega t} \langle m_{01,j}(t) U_{jj}(t) m_{01,j}(0)\rangle_b e^{-t/2T_1}, \tag{7.10}$$

where vibrational relaxation is again included phenomenologically. For isotropic systems, $G_0(\omega) = (G_0(\hat{x},\omega) + G_0(\hat{y},\omega) + G_0(\hat{z},\omega))/3$, where $\hat{x}$, $\hat{y}$ and $\hat{z}$ are unit vectors along the Cartesian coordinate axes in the simulation-box frame. Eq. (7.10) is very similar to the formula we used for IR spectrum except that: 1) an extra factor of ω^2 is in Eq. (7.10) due to the definition of $G(\vec{k},\omega)$; 2) the transition moment $m_{01,j}$ in IR (transition dipole moment, denoted as $\mu_{01,j}$ later) has a component μ'_j due to the dipole interaction between the IR light and the sample, which is absent for IINS; 3) as we are considering incoherent neutron scattering, Eq. (7.10) has only an incoherent part ($U_{jj}(t)$), while the IR line shape usually contains both incoherent and coherent parts ($U_{ij}(t)$). Despite these differences, the calculations of IINS (Eq. (7.10)) and of the IR spectrum within our mixed quantum/classical approach are under the same level of approximation — truncation at the first order in OH stretch coordinate x. From the second and third differences, one can see clearly that IINS is more suitable (than IR and Raman) for probing full vibrational density of states.

The MD simulations in this chapter are performed in the NPT ensemble with the third version of the E3B model (E3Bv3).[85] Liquid water, supercooled water and ice Ih are all simulated with 432-molecule simulation boxes. The pressure is controlled by a Parrinello-Rahman barostat[296] with a coupling constant of 10.0 ps in production runs, and the temperature is controlled by a Nosé-Hoover thermostat[297,298] with a coupling constant of 5.0 ps. Other simulation details are the same as in Section 4.2. For low-frequency IINS, we directly calculate the Fourier trans-

form of velocity TCF $f(\omega)$ and include the harmonic quantum correction factor (see Section 2.4). For the calculation of high-frequency IINS, the latest maps in Ref. 78 are used. Note that for all the spectral calculations, the molecular geometry and charges on atoms are adjusted from TIP4P/2005 (the reference potential for the E3Bv3 model) to TIP4P, for which all the spectroscopic maps were developed.

7.3 High-Frequency IINS: OH Stretch

Fig. 7.1 displays the calculated $G_0(\omega)$ for liquid water (top panel), supercooled water (middle panel), and ice Ih (bottom panel), along with extrapolated results from experiment for the same systems. Note that as the melting temperature of the E3Bv3 model employed in this chapter is 260 K,[85] we choose 258 K for ice Ih and supercooled water in our simulations. All the theoretical and experimental spectra show essentially single peaks, except that the theoretical spectrum for ice Ih shows a shoulder on the low-frequency side of the main peak. This shoulder may also exist in experiment, but the low frequency-resolution of the experiment precludes a definitive answer. In terms of peak position, a fair agreement between theory and experiment is seen for liquid and supercooled water. However, for ice Ih, the calculated spectrum is blue-shifted by about 50 cm^{-1} compared to the experiment. This blue shift is probably due to the fact that the frequency map overestimates the OH 0-1 transition frequency in ice Ih by about 30 - 40 cm^{-1}.[78] Regarding the line-width, our theory is too narrow for supercooled water and ice Ih, and this discrepany might be due to the inadequacy of the experimental extrapolation or the fact that our simulation temperatures (258 K) are lower than corresponding experimental ones ($\sim$270 K).

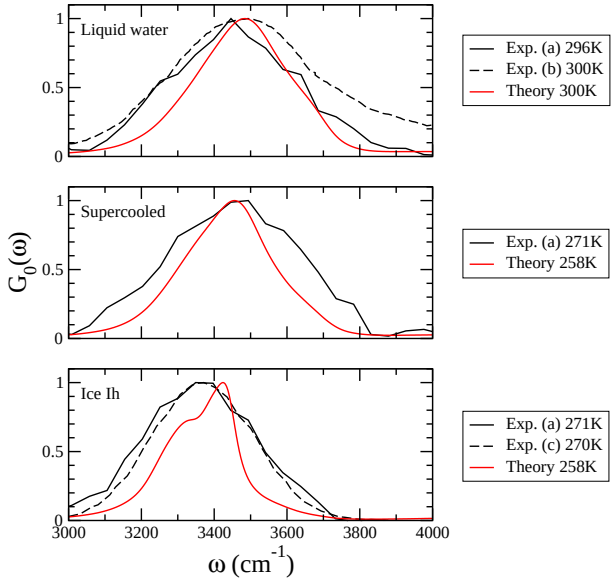

Figure 7.1: Experimentally extrapolated (black lines) and calculated (red lines) $G_0(\omega)$ for OH stretch in liquid water, supercooled water and ice Ih. Reference numbers for experiment are: (a) Ref. 283; (b) Ref. 299; (c) Ref. 300. All the spectra are normalized to have the same height of 1.

In order to see the connection between IR and IINS spectra, we also calculate IR spectra for ice Ih and supercooled water at 258 K, shown as solid black lines in Fig. 7.2, along with IINS spectra (solid red lines). IR spectra in both cases show a single peak, red-shifted compared to the main peaks in IINS. In order to understand this, we decompose IR line shape into its incoherent and coherent parts, given by, respectively

$$I_{\rm IR}^{\rm inc}(\omega) = 2{\rm Re}\int_0^\infty dt e^{i\omega t}\frac{1}{3}\sum_p\sum_j \left\langle \mu_{01,j}^p(t)U_{jj}(t)\mu_{01,j}^p(0)\right\rangle_b e^{-t/2T_1}, \tag{7.11}$$

and

$$I_{\rm IR}^{\rm coh}(\omega) = 2{\rm Re}\int_0^\infty dt e^{i\omega t}\frac{1}{3}\sum_p\sum_{j,l\neq j} \left\langle \mu_{01,j}^p(t)U_{jl}(t)\mu_{01,l}^p(0)\right\rangle_b e^{-t/2T_1}, \tag{7.12}$$

where $\mu_{01,j}^p(t)$ is the pth Cartesian component of 0-1 transition dipole associated with the jth OH chromophore, and $\mu_{01,j}^p(t) \approx \mu_j'(t)x_{01,j}(t)(\hat{u}_j(t)\cdot\hat{p})$ ($\hat{p} = \hat{x},\hat{y},\hat{z}$). It is clear that the incoherent

part of IR spectrum $I_{\text{IR}}^{\text{inc}}(\omega)$ (dashed black line) is very similar to $G_0(\omega)$ from IINS, especially in the case of ice Ih. This is simply because within our mixed quantum/classical approach, the only difference between Eqs. (7.11) and (7.10) is that Eq. (7.11) contains dipole derivative $\mu_j'(t)$, the main contributor to the so-called non-Condon effect in IR spectra. As mentioned in Chapter 6, the non-Condon effect is negligle in ice Ih, so $I_{\text{IR}}^{\text{inc}}(\omega)$ and $G_0(\omega)$ are very similar for ice. The non-Condon effect is more pronounced in supercooled water, and $I_{\text{IR}}^{\text{inc}}(\omega)$ shows a slightly visible shoulder on the red side of the main peak, which is not seen in $G_0(\omega)$. Even though the incoherent part of the IR spectra essentially carries the same information as IINS does, the coherent part of the IR spectra (which arises from vibrational couplings) considerably diminishes the intensity over 3400 cm^{-1}, and enhances the red side of the spectra. Therefore, if one is interested in the vibrational density of states, IINS is to be preferred over IR. In order to demonstrate this further, we also calculate the distribution of vibrational eigen-frequencies (solid blue lines in Fig. 7.2), defined by

$$F(\omega) = \langle \delta(\omega - \lambda_m) \rangle \,, \tag{7.13}$$

where λ_m is the mth vibrational eigen-frequency obtained by diagonalizing κ matrix (Eq. (2.22)). This frequency distribution is basically the OH stretch vibrational density of states, and $G_0(\omega)$ from IINS resembles it quite well, while IR spectrum is quite different from it. This observation could be understood as follows. If we consider Eq. (7.10) in the inhomogeneous limit (transition moments and exciton Hamiltonian are time-independent), assume that $m_{01,j}$ is a constant for all j's (usually a good assumption for IINS of isotropic systems), and also neglect the ω^2 prefactor and the lifetime factor ($e^{-t/2T_1}$), we will have $G_0(\omega) \sim F(\omega)$. As the system is not exactly in the inhomogeneous limit (motional narrowing exists) and the lifetime does play a role, $G_0(\omega)$ is narrowed and sharpened from $F(\omega)$. Within the same approximations, we also have $I_{\text{IR}}^{\text{inc}}(\omega) \sim F(\omega)$, but this relation does not hold for total IR line shape.

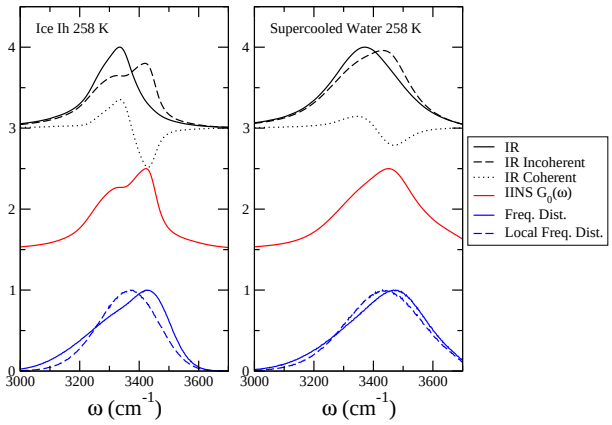

Figure 7.2: Calculated OH stretch IR and IINS spectra for ice Ih (left panel) and supercooled water (right panel) at 258 K. IR line shapes (solid black lines) with incoherent (dashed black lines, from Eq. (7.11)) and coherent (dotted black lines, from Eq. (7.12)) contributions are shown in the top, and IINS spectra $G_0(\omega)$ (red lines, from Eq. (7.10)) are in the middle. Frequency distributions (solid blue lines), calculated from Eq. (7.13), along with local OH-stretch frequency distributions (dashed blue lines, from Eq. (7.14)) are shown at the bottom. IR and IINS spectra are shifted by 3 and 1.5 arbitrary units, respectively, for pictorial clarity.

7.4 Low-Frequency IINS: Intermolecular Motions

We also calculate low-frequency IINS for liquid water, supercooled water and ice Ih with (blue lines) and without (red lines) the harmonic quantum correction factor (HQCF), shown in Fig. 7.3 along with experimental results. The theoretical spectra without the HQCF seem to resemble the experimental ones better than those with HQCF. The reason for this might be that the empirical E3Bv3 model has already included some nuclear quantum effects in its parametrization; supporting this idea is the fact that the E3Bv3 model reproduces the diffusion constant and rotational correlation time semi-quantitatively.[91] Nevertheless, the qualitative spectral features are unchanged regardless of whether the HQCF is included. For liquid phases, the peak at about 50 cm^{-1} is seen in both experimental and theoretical spectra, and it is usually assigned to O–O–O bending motion.[301] The peaks and shoulders above 400 cm^{-1} (due to librations) are blue shifted

compared to experiment, which is presumably related to the flaw of the E3Bv3 model for describing water rotation (the E3Bv3 model overestimates the H-H rotational correlation time,[85] as it exhibits too strong of a hydrogen-bond network). We also see some intensity buildup between 200 and 300 cm^{-1} in our calculated spectrum, the existence of which is difficult to confirm in experiment. However, this feature is believed to be associated with the hydrogen-bond stretch, which is well resolved in the low-frequency IR spectrum for liquid water (see below). For ice Ih, it is well-known that at 15 K there are four peaks below 400 cm^{-1} in IINS, the assignment of which has triggered some debates in the literature.[117,172–174,178,201,203–205,275,302] Because the calculated spectrum below 400 cm^{-1} is still somewhat noisy, we claim only that our theory reproduces the first and fourth peaks in experiment, and that we see considerable phonon density of states between 100 and 300 cm^{-1}. The librational peaks in our theoretical spectrum for ice are also blue-shifted, but all three experimentally observed peaks are present in the calculated spectrum.

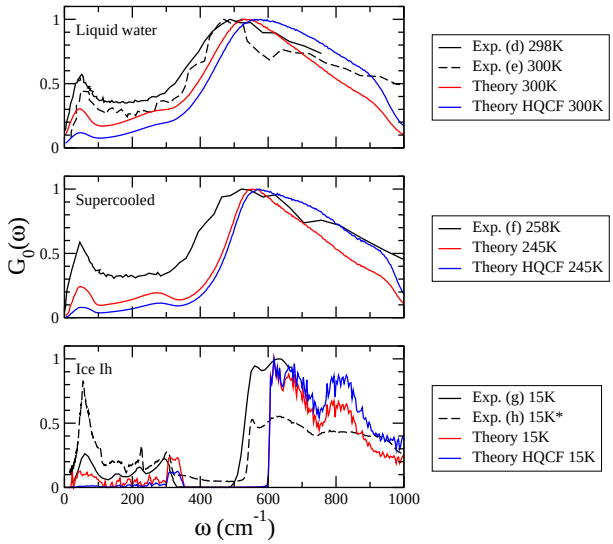

Figure 7.3: Experimentally extrapolated (black lines) and calculated $G_0(\omega)$ in the frequency range of 0-1000 cm^{-1} for liquid water, supercooled water and ice Ih. The red lines are calculated $G_0(\omega)$ without harmonic the QCF, while the blue lines are with it. Reference numbers for experiment are: (d) Ref. 303; (e) Ref. 304; (f) Ref. 305; (g) Ref. 173; (h) Ref. 176. All the spectra are normalized to have the same height of 1, except for that from Ref. 176, denoted by

an asterisk. The spectrum from Ref. 176 is raw experimental IINS intensity data, so only the peak positions should be considered in the comparison with theory. Fig. 23 in Ref. 176 shows $G_0(\omega)$ between 0 and 400 cm^{-1}, which is similar to the result from Ref. 173.

As in the high-frequency case, we also compare the low-frequency IR and IINS (including the harmonic quantum correction factor) for ice Ih and supercooled water at 258 K. As discussed in Chapter 3, a successful reproduction of low-frequency IR for ice Ih requires the incorporation of the polarization effect on the dipole surface, and we have developed a simple scheme to include this effect for the E3B model (see Chapter 3). The parameter γ (which can be regarded as an effective polarizability) for ice Ih is 2.300 $\mathring{A}^3$, and for supercooled water we choose 1.495 $\mathring{A}^3$, the value for liquid water. Note that we change the water molecule from TIP4P/2005 to TIP4P in the calculation of low-frequency IR spectrum in order to use these values of parameter γ. Fig. 7.4 displays calculated low-frequency IR (solid black lines) for supercooled water and ice Ih at 258 K, along with the low-frequency IINS (red lines). In Chapter 3, we decomposed low-frequency IR into single-particle correlation and intermolecular cross correlation, which in the language of this chapter are the incoherent and coherent parts of the low-frequency IR. Therefore, we repeat this decomposition for supercooled water and ice Ih, and incoherent and coherent parts of low-frequency IR are shown as dashed and dotted black lines in Fig. 7.4. Similarly to the case for OH stretch, the incoherent part looks like IINS, but due to the optical selection rules the peak intensities are slightly changed in the incoherent IR. The coherent IR then acts to selectively enhance and attenuate some peaks. Experimentally, due to this enhancement or attenuation, low-frequency IR and IINS could play complementary roles in assigning spectral features.[261]

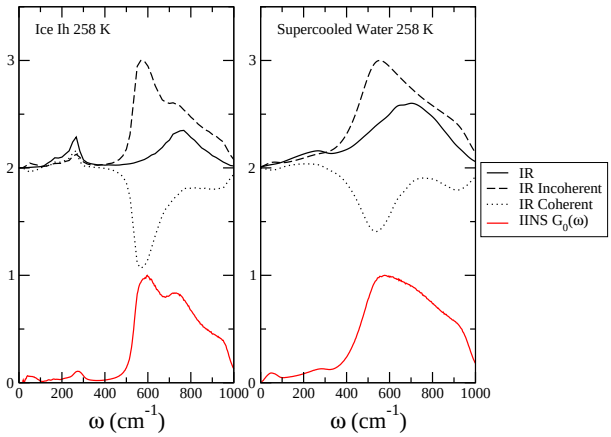

Figure 7.4: Calculated low-frequency IR and IINS spectra (below 1000 cm^{-1}) for ice Ih (left panel) and supercooled water (right panel) at 258 K. IR line shapes (solid black lines) with incoherent (dashed black lines) and coherent (dotted black lines) contributions are shown in the top, and IINS spectra $G_0(\omega)$ (solid red lines) are at the bottom. IR spectra are shifted by 2 arbitrary units, for pictorial clarity.

7.5 Discussion: Hydrogen Bond Strength

As mentioned in Section 7.1, the conventional widsom that hydrogen bonding is stronger in ice Ih than that in supercooled water has been challenged recently.[283] A stronger hydrogen bond presumably leads to a stronger intermolecular interaction between the donor and acceptor molecules (i.e., more negative potential energy), a smaller O$\cdots$H distance ($\cdots$ denotes a hydrogen bond) in O-H$\cdots$O (i.e., the first intermolecular peak in $g_{OH}(r)$ occurs at a smaller r), a red-shift of OH stretch frequency, and a blue-shift of hydrogen-bond stretch frequency. In this section, we attempt to discuss the hydrogen bond strength in supercooled water and ice using these four descriptors in the context of our model.

In panel (a) of Fig. 7.5, we plot the distribution of pairwise intermolecular potential energies $P(E)$ in supercooled water and ice Ih. Note that as TIP4P/2005 is a good effective two-body potential, the pairwise intermolecular potential energy is calculated using the parameters (e.g., charges, L-J parameters) of TIP4P/2005, and three-body interaction is not considered here. We

see in all cases that most pair energies are close to zero simply because that the paired molecules are far apart. A minimum in the distribution is observed at -11.85 kJ/mol for supercooled water, and at -9.85 kJ/mol for ice Ih (the grid size we use is 0.1 kJ/mol). This minimum is widely used as a threshold in energetic definitions of the hydrogen bond.[306,307] If the pair energy is lower than this minimum, a hydrogen bond is believed to be formed between the pair, so the peak below this minimum in $P(E)$ reflects the hydrogen bond strength to some extent. This peak lies at -23.05 kJ/mol for supercooled water, and at -24.65 kJ/mol for ice Ih. Given that the thermal energy at 258 K is about 2.15 kJ/mol, this observation implies that the hydrogen bond in ice Ih might be slightly stronger than that in supercooled water, consistent with the conventional wisdom. In panel (b), we also plot the OH radial distribution functions (RDFs) $g_{OH}(r)$ for these two phases (intramolecular OH peak is not shown), and both RDFs show the first peak at 0.18 nm. Given the resolution (0.005 nm) we use, we cannot tell in which phase the intermolecular O$\cdots$H distance is shorter, so it seems that the OH RDF is not sensitive enough to tell the small difference in hydrogen bond strength between these two phases. However, one common feature in $P(E)$ and $g_{OH}(r)$ is that the peak associated with hydrogen-bonded pairs is always more intense in ice than that in supercooled water, indicating that there are more hydrogen bonds in ice Ih, even if they are not stronger.

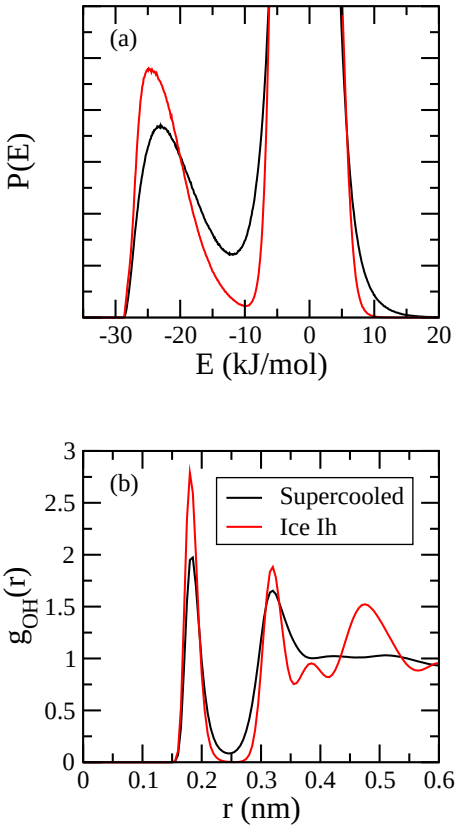

Figure 7.5: (a) Distributions of pairwise intermolecular potential energy $P(E)$, and (b) OH radial distribution functions $g_{OH}(r)$ for supercooled water (black lines) and ice Ih (red lines) at 258 K from simulations with the E3Bv3 model.

As we discussed in Section 1.3, both OH-stretch and low-frequency vibrational spectra can be utilized to examine hydrogen bonding in water. From Fig. 7.2, all the spectra (IR and IINS) for ice are red-shifted with respect to the spectra for supercooled water. These spectra, including $F(\omega)$, are all complicated by vibrational couplings. In order to remove the effect of vibrational couplings, in Fig. 7.2 we also plot the distribution of local OH stretch transition frequency (dashed blue lines), given by

$$F_0(\omega) = \langle \delta(\omega - \omega_j) \rangle \,, \tag{7.14}$$

where ω_j is the vibrational frequency of the jth local OH chromphore. In fact, the red-shift from supercooled water to ice is even more evident in $F_0(\omega)$ than in $F(\omega)$. This red-shift of the

OH-stretch peak suggests that the hydrogen bond is stronger in ice. In examining low-frequency vibrational spectra in Fig. 7.4, we find that the positions of translational peaks below 400 cm^{-1} for supercooled water and ice Ih are very close, and no blue shift is evident (at least within our calculations).

To sum up, two out of four descriptors (pairwise intermolecular potential energy and OH-stretch peak position) in our calculations seem to support the conventional wisdom, but disagree with a recent study,[283] while the other two (OH RDF and hydrogen-bond stretch peak positions in low-frequency IR) evince no clear distinction between the hydrogen-bond strength in supercooled water and in ice Ih at 258 K. Certainly, we do not treat low-frequency motions quantum mechanically in these systems (note that we do treat OH stretch quantum mechanically in our spectral calculations), so we cannot rule out the possibility that the quantum nature of water in these phases will make the hydrogen bond in supercooled water stronger than that in ice. However, this scenario is not supported by a recent path-integral study either.[282] Further studies might be required to fully understand this issue. Also, note that we have only approached the problem about the hydrogen-bond strength in an averaged sense, but we have not yet addressed this problem given that we consider the same type of hydrogen bond in both phases (hydrogen bond can be classified according to the hydrogen bonding conditions of the donor and acceptor molecules). Such an analysis is ongoing.

7.6 Concluding Remarks

The mixed quantum/classical approach developed in the Skinner group has been extended to calculate incoherent inelastic neutron scattering (IINS) for the OH stretch. Reasonable agreement is reached between theory and experiment for liquid water, supercooled water and ice Ih. Along with presenting the low-frequency IINS, we have shown the connection between IINS and IR spectra, and argued that IINS provides a more direct way to measure vibrational density of states. Moreover, the analysis of our calculated spectra and simulations seem to support the conventional wisdom that the hydrogen bond is stronger in ice Ih than that in supercooled water at similar temperatures, but probably only by a very small amount.

Chapter 8

Summary and Future Directions

In this thesis, we have illustrated with five examples how vibrational spectroscopy can help us to understand the structure and dynamics of ice Ih with the aid of theory and molecular simulations. On one hand, from these studies we are able to interpret many features in various vibrational spectra. On the other hand, the agreement between theory and experiment validates our theoretical models, especially the E3B water model. It is our hope that we can provide a versatile and robust theoretical model (water model and spectral calculation approach) to the ice and even the water research community. There is clearly still much work to be done to validate and refine our theoretical model, and some of our ideas in this regard are briefly discussed below.

As mentioned in Chapter 1, there are 16 crystalline phases and 3 amorphous phases for ice.[9] Here, we note a few interesting observations in other ice phases, and basic scientific questions behind them. IR and Raman spectra have been recently reported for ice XI, the proton-ordered hexagonal ice,[193,264,308,309] and its OH-stretch Raman and low-frequency IINS spectra look similar to those for ice Ih, but its OH-stretch IR spectrum and low-frequency Raman look quite different from those for ice Ih. Simulating these spectra may help us understand proton order/disorder in ice phases. 2DIR spectra for isotope-diluted low- and high-density amorphous ices reported recently shows much more inhomogeneous broadening than for ice Ih,[91,310,311] meaning that there will be more diagonal and off-diagonal disorder in amorphous ices. Therefore, studying vibrational resonant energy transfer in these phases could enhance our understanding of energy transfer in disordered systems, for which many models (e.g., the Anderson model[312,313]) have been developed in the past.

Ice in heterogeneous or confined environments is very important practically, and vibrational spectroscopy has been very useful for studying these systems. Surface premelting at the air/ice interface is relevant for the frost heave phenomenon mentioned in Chapter 1, and glancing angle Raman and sum-frequency generation spectra for this interface have been measured,[314–320] but their interpretation still requires the aid of theoretical modeling. Understanding ice nucleation is essential for environmental science as well as public transportation interests, such as the aviation industry (mentioned in Chapter 1). Vibrational spectra of mesoscopic water clusters of various sizes ($\sim$ nm), which might be precursers to macroscopic ice crystals in clouds ($\sim$ mm), have been measured,[321,322] and again theoretical modeling might shed light on this problem.

There is still plenty of room to improve our spectral calculation approach. The water bending mode is ignored in our current approach, but experiment suggests that it might influence stretching modes through Fermi resonance.[196,323,324] Including the bend in our exciton Hamiltonian represents a natural extension of our current method. Furthermore, vibrational nonadiabaticity is suggested by Hamm and coworkers to be possibly important in ice,[36,325] and including this in the spectral calculation requires revisions of our system-bath treatment. In fact, surface hopping[326] and Ehrenfest[327] methods have been implemented in the spectral calculations by Jansen and coworkers. Nuclear quantum effects are pronounced in ice, especially in H_2O ice at low temperatures.[171,209,210,282] Including these in our approach requires a quantum description of the bath evolution, and path-integral-based methods might be promising in this regard.[328–332]

Appendix A: Third-Order Nonlinear Response Functions for 2DIR

In this appendix, we provide details of the third-order nonlinear response functions for 2DIR as well as the linear response function for linear IR within the mixed quantum/classical approach for isotope-dilute ice Ih (only one chromophore). The linear response function for light with polarization $\hat{p}$ is given by[35]

$$R_L^p(t) = \langle \mu_{10}^p(0)\mu_{10}^p(t)U_{10}(t)\rangle \tag{A1}$$

where the subscript L indicates the linear response function, and $U_{10}(t) = \exp\left[-i\int_0^t \omega_{10}(\tau)d\tau\right]$, $\omega_{10}(\tau)$ is the fluctuating 1-0 transition frequency of that OH stretch, μ_{10}^p is the pth Cartesian component of the corresponding transition dipole (p is now a supercript).

The third-order response functions have four polarization indices (i.e., p, q, r, s), and are given by[41,333]

$$\begin{aligned}
R_1^{pqrs}(t_3,t_2,t_1) &= \langle \mu_{10}^p(0)\mu_{10}^q(t_1)\mu_{10}^r(t_1+t_2)\mu_{10}^s(t_1+t_2+t_3) \\
&\quad U_{10}^*(t_1)U_{10}^*(t_1+t_2)U_{10}(t_1+t_2+t_3)\rangle \\
R_2^{pqrs}(t_3,t_2,t_1) &= R_1^{pqrs}(t_3,t_2,t_1) \\
R_3^{pqrs}(t_3,t_2,t_1) &= -\langle \mu_{10}^p(0)\mu_{10}^q(t_1)\mu_{21}^r(t_1+t_2)\mu_{21}^s(t_1+t_2+t_3) \\
&\quad U_{10}^*(t_1)U_{21}^*(t_1+t_2)U_{21}(t_1+t_2+t_3)\rangle \\
R_4^{pqrs}(t_3,t_2,t_1) &= \langle \mu_{10}^p(0)\mu_{10}^q(t_1)\mu_{10}^r(t_1+t_2)\mu_{10}^s(t_1+t_2+t_3) \\
&\quad U_{10}(t_1)U_{10}^*(t_1+t_2)U_{10}(t_1+t_2+t_3)\rangle \\
R_5^{pqrs}(t_3,t_2,t_1) &= R_4^{pqrs}(t_3,t_2,t_1) \\
R_6^{pqrs}(t_3,t_2,t_1) &= -\langle \mu_{10}^p(0)\mu_{10}^q(t_1)\mu_{21}^r(t_1+t_2)\mu_{21}^s(t_1+t_2+t_3) \\
&\quad U_{10}(t_1)U_{21}^*(t_1+t_2)U_{21}(t_1+t_2+t_3)\rangle,
\end{aligned} \tag{A2}$$

where t_1, t_2 and t_3 are the three time delays in the four-wave-mixing experiments, and $U_{21}(t) = \exp\left[-i\int_0^t \omega_{21}(\tau)d\tau\right]$. $\omega_{21}(\tau)$ is the fluctuating 2-1 transition frequency of the OH stretch, and μ_{21}^p is the pth Cartesian component of the corresponding 2-1 transition dipole. For a polycrystalline sample, one needs to average over all orientations of the polarizations with respect to the crystal axes in order to obtain the response functions in the lab frame (R_L, and $R_{1,2,3,4,5,6}$), and

details are given in Appendix B.

The 2DIR line shape in the impulsive limit is then given by[246,333,334]

$$S(\omega_3, t_2, \omega_1) \sim \mathrm{Re} \sum_{i=1}^{6} S_i(\omega_3, t_2, \omega_1), \tag{A3}$$

where

$$\begin{aligned}
S_1(\omega_3, t_2, \omega_1) &= S_2(\omega_3, t_2, \omega_1) = \int_0^\infty dt_3 \int_0^\infty dt_1 \exp(i\omega_3 t_3 - i\omega_1 t_1) R_1(t_3, t_2, t_1) L_1(t_3, t_2, t_1) \\
S_3(\omega_3, t_2, \omega_1) &= \int_0^\infty dt_3 \int_0^\infty dt_1 \exp(i\omega_3 t_3 - i\omega_1 t_1) R_3(t_3, t_2, t_1) L_3(t_3, t_2, t_1) \\
S_4(\omega_3, t_2, \omega_1) &= S_5(\omega_3, t_2, \omega_1) = \int_0^\infty dt_3 \int_0^\infty dt_1 \exp(i\omega_3 t_3 + i\omega_1 t_1) R_4(t_3, t_2, t_1) L_4(t_3, t_2, t_1) \\
S_6(\omega_3, t_2, \omega_1) &= \int_0^\infty dt_3 \int_0^\infty dt_1 \exp(i\omega_3 t_3 + i\omega_1 t_1) R_6(t_3, t_2, t_1) L_6(t_3, t_2, t_1),
\end{aligned} \tag{A4}$$

and

$$\begin{aligned}
L_1(t_3, t_2, t_1) &= L_2(t_3, t_2, t_1) = L_4(t_3, t_2, t_1) = L_5(t_3, t_2, t_1) = e^{-(t_3 + 2t_2 + t_1)/2T_1} \\
L_3(t_3, t_2, t_1) &= L_6(t_3, t_2, t_1) = e^{-(3t_3 + 2t_2 + t_1)/2T_1}.
\end{aligned} \tag{A5}$$

Note that as in the calculation for linear IR, the lifetime is taken into account phenomenologically.[334,335] The linear line shape is given by Eq. (6.1).

The calculation of the third-order response functions is relatively expensive, but for ice we can make some approximations to simplify the calculation. The first two approximations we make are the Condon approximation (i.e., the magnitudes of the transition dipoles are taken to be constants), and the harmonic approximation for their magnitudes ($\mu_{21} = \sqrt{2}\mu_{10}$). For ice Ih, all water molecules are fully hydrogen bonded to four nearest neighbors. Therefore, the Condon approximation is expected to hold. Regarding the harmonic approximation for the transition dipoles, our DFT calculations show that the anharmonicity for the transition dipole of the OH chromophores is very small throughout the frequency range of interest.[78] We can also neglect the orientational dynamics (changes in the directions of the transition dipoles) as the reorientation of the water molecules are hindered due to the rigid hydrogen bond network in ice Ih. With these three approximations, the orientationally-averaged linear and third-order

response functions become

$$R_L(t) \sim \langle U_{10}(t) \rangle, \tag{A6}$$

and

$$\begin{aligned} R_1(t_3,t_2,t_1) &= R_2(t_3,t_2,t_1) \sim \langle U_{10}^*(t_1) U_{10}^*(t_1+t_2) U_{10}(t_1+t_2+t_3) \rangle \\ R_3(t_3,t_2,t_1) &\sim -2\langle U_{10}^*(t_1) U_{21}^*(t_1+t_2) U_{21}(t_1+t_2+t_3) \rangle \\ R_4(t_3,t_2,t_1) &= R_5(t_3,t_2,t_1) \sim \langle U_{10}(t_1) U_{10}^*(t_1+t_2) U_{10}(t_1+t_2+t_3) \rangle \\ R_6(t_3,t_2,t_1) &\sim -2\langle U_{10}(t_1) U_{21}^*(t_1+t_2) U_{21}(t_1+t_2+t_3) \rangle. \end{aligned} \tag{A7}$$

For each chromophore we can write

$$\omega_{10}(\tau) = \langle \omega_{10} \rangle + \delta\bar{\omega}_{10} + \delta\omega_{10}(\tau). \tag{A8}$$

The first term on the right-hand side is the global average over all chromophores, the second term is the deviation of the time-averaged frequency for a given chromophore from the global average, and the third term represents the dynamic fluctuations for each chromophore. Thus, the second term results from proton-disorder-induced static inhomogeneity, and the third term comes from phonon fluctuations. The time-averaged frequency for a given chromophore discussed before is the sum of the first two terms. A simple, and it turns out, accurate approximation, is to take static fluctuations to be uncorrelated with the dynamic ones, and assume that the dynamic fluctuations are independent of chromophore. In this case the frequency-frequency time-correlation function is

$$C(\tau) = \langle (\omega_{10}(\tau) - \langle \omega_{10} \rangle)(\omega_{10}(0) - \langle \omega_{10} \rangle) \rangle = \langle \delta\bar{\omega}_{10}^2 \rangle + \langle \delta\omega_{10}(\tau)\delta\omega_{10}(0) \rangle \equiv \sigma_1^2 + C_1(\tau). \tag{A9}$$

The average in the first term on the right-hand side is an ensemble average over the chromophores, while the average in the second term is a time average over the fluctuations.

At this point we can make the cumulant expansion, which is valid for the two terms in Eq. (A8) for completely different reasons. The inhomogeneous broadening evidently (see Fig. 6.3) is Gaussian because of the central limit theorem, while the time-dependent fluctatuations are Gaussian because the low-frequency vibrations are approximately harmonic. Therefore, we obtain[41]

$$R_L(t) \sim e^{-i\langle \omega_{10} \rangle t} e^{-\frac{1}{2}\sigma_1^2 t^2} e^{-g_1(t)}, \tag{A10}$$

where

$$g_m(t) = \int_0^t d\tau (t-\tau) C_m(\tau) \tag{A11}$$

(see below for $m = 2, 3$).

Similarly,

$$\begin{aligned}
R_1(t_3,t_2,t_1) = R_2(t_3,t_2,t_1) &\sim e^{i\langle\omega_{10}\rangle t_1 - i\langle\omega_{10}\rangle t_3} \\
&\quad e^{-\frac{1}{2}\sigma_1^2(t_1-t_3)^2} e^{-g_1(t_1)+g_1(t_2)-g_1(t_3)-g_1(t_1+t_2)-g_1(t_2+t_3)+g_1(t_1+t_2+t_3)} \\
R_3(t_3,t_2,t_1) &\sim -2e^{i\langle\omega_{10}\rangle t_1 - i\langle\omega_{21}\rangle t_3} \\
&\quad e^{-\frac{1}{2}(\sigma_1^2 t_1^2 + \sigma_3^2 t_3^2 - 2\sigma_2^2 t_1 t_3)} e^{-g_1(t_1)+g_2(t_2)-g_3(t_3)-g_2(t_1+t_2)-g_2(t_2+t_3)+g_2(t_1+t_2+t_3)} \\
R_4(t_3,t_2,t_1) = R_5(t_3,t_2,t_1) &\sim e^{-i\langle\omega_{10}\rangle t_1 - i\langle\omega_{10}\rangle t_3} \\
&\quad e^{-\frac{1}{2}\sigma_1^2(t_1+t_3)^2} e^{-g_1(t_1)-g_1(t_2)-g_1(t_3)+g_1(t_1+t_2)+g_1(t_2+t_3)-g_1(t_1+t_2+t_3)} \\
R_6(t_3,t_2,t_1) &\sim -2e^{-i\langle\omega_{10}\rangle t_1 - i\langle\omega_{21}\rangle t_3} \\
&\quad e^{-\frac{1}{2}(\sigma_1^2 t_1^2 + \sigma_3^2 t_3^2 + 2\sigma_2^2 t_1 t_3)} e^{-g_1(t_1)-g_2(t_2)-g_3(t_3)+g_2(t_1+t_2)+g_2(t_2+t_3)-g_2(t_1+t_2+t_3)},
\end{aligned} \tag{A12}$$

where $\sigma_2^2 = \langle \delta\bar{\omega}_{10}\delta\bar{\omega}_{21}\rangle$, $\sigma_3^2 = \langle \delta\bar{\omega}_{21}^2\rangle$,

$$\begin{aligned}
C_2(t) &= \langle \delta\omega_{21}(t)\delta\omega_{10}(0)\rangle \\
C_3(t) &= \langle \delta\omega_{21}(t)\delta\omega_{21}(0)\rangle,
\end{aligned} \tag{A13}$$

and $g_2(t)$ and $g_3(t)$ are defined above.

Appendix B: Orientational Averaging for IR, Raman and 2DIR

For a polycrystalline (isotropic) ice Ih sample, one needs to average over all orientations of the light polarizations with respect to the crystal axes in the calculation of response functions.[37,336] In this appendix, we only consider the line shapes for isotope-diluted samples (one chromophore) within the mixed quantum/classical approach.

The linear response function for linear IR is given by

$$R_{\text{IR}} = \frac{1}{3}(xx + yy + zz), \tag{B1}$$

where $xx \equiv \langle \mu_{10}^x(0)\mu_{10}^x(t)U_{10}(t)\rangle$, etc.

For 2DIR, we first define

$$\begin{aligned} A &= xxxx + yyyy + zzzz, \\ B &= xxyy + xxzz + yyxx + yyzz + zzxx + zzyy, \\ C &= xyxy + yxyx + yzyz + zyzy + zxzx + xzxz, \\ D &= xyyx + yxxy + yzzy + zyyz + zxxz + xzzx, \end{aligned} \tag{B2}$$

where for R_1, $xxxx \equiv \langle \mu_{10}^x(0)\mu_{10}^x(t_1)\mu_{10}^x(t_1+t_2)\mu_{10}^x(t_1+t_2+t_3)U_{10}^*(t_1)U_{10}^*(t_1+t_2)U_{10}(t_1+t_2+t_3)\rangle$, etc. The response functions for 2DIR spectra in the parallel and perpendicular geometries are given, respectively, by

$$R_{\parallel} = \frac{1}{30}(6A + 2B + 2C + 2D), \tag{B3}$$

and

$$R_{\perp} = \frac{1}{30}(2A + 4B - C - D). \tag{B4}$$

Note that this orientational averaging is applied for all six response functions in 2DIR, after which one performs appropriate Fourier transform (Eq. (A4) in Appendix A) to get $S_{\parallel}$ and $S_{\perp}$ in Chapter 6. For static systems, $B = C = D$. Therefore, $S_{\perp} = S_{\parallel}/3$. This relation is, to a good approximation, valid for ice Ih.

For Raman, the terms in Eq. (B2) are redefined: for instance, $xyxy \equiv \langle \alpha_{10}^{xy}(0)\alpha_{10}^{xy}(t)U_{10}(t)\rangle$, where α_{10}^{xy} is the xy tensor element of transition polarizability. As $\alpha_{pq} = \alpha_{qp}$ for $p, q = x, y, z$,

we further define

$$E \equiv C = D = 2(xyxy + yzyz + zxzx). \tag{B5}$$

Now the polarizaed and depolarized Raman line shapes are given, respectively, by

$$R_{\mathrm{VV}} = \frac{1}{30}(6A + 2B + 4E), \tag{B6}$$

and

$$R_{\mathrm{VH}} = \frac{1}{30}(2A - B + 3E). \tag{B7}$$

For neat H_2O (D_2O) ice Ih, the expressions for orientational averaging are the same, but the terms in Eqs. (B1), (B2) and (B5) have to be redefined, and the expressions for IR and Raman can be found in Ref. 82. Also note that Eq. (5.2) in Chapter 5 has already taken the orientational averaging into account.[230,337]

Appendix C: 3PEPS and Inhomogeneous Broadening

In a paper by Piryatinski and Skinner[256] they showed that under certain approximations (including $C_1(t) = C_2(t) = C_3(t)$ and $\sigma_1^2 = \sigma_2^2 = \sigma_3^2$) at long times the peak shift is related to the full frequency-frequency time-correlation function $C(t)$ by

$$t_1^*(t_2) = T_p C(t_2)/C(0), \tag{C1}$$

where

$$T_p = \frac{1}{\sqrt{\pi C(0)}} \frac{\zeta D(\zeta/2)}{(1 - e^{-\zeta^2/4})}, \tag{C2}$$

$\zeta = \Delta/\sqrt{C(0)}$, $D(z) = e^{-z^2} \int_0^z dx\, e^{x^2}$ is Dawson's integral, and $\Delta = \langle\omega_{10}\rangle - \langle\omega_{21}\rangle$ is the anharmonicity.

In the case of ice $C(t)$ is given by Eq. (A9), and so $C(0) = \sigma_1^2 + C_1(0)$. Since $C_1(\infty) = 0$, that means that

$$t_1^*(\infty) = T_p \sigma_1^2/(\sigma_1^2 + C_1(0)). \tag{C3}$$

Appendix D: IINS and the Velocity Time Correlation Function

Eq. (7.4) is well-known to be true for isotropic classical systems, and in this appendix, we show that it is also valid for isotropic quantum systems. The derivation strategy is the same for both classical and quantum systems, and details for the classical case can be found in Ref. 37. (Note that in Ref. 40, if one manipulates Eq. (1.39), Eq. (1.45), Eq. (1.46) and Eq. (8.5) correctly, the relation for the quantum case can be also verified.)

Following elegant work by Rahman, Singwi and Sjölander,[286] the incoherent part of the intermediate scattering function (Eq. (7.2)) can be written as a cumulant expansion

$$I(\vec{k},t) = \exp\left[it\frac{\hbar k^2}{2m} + \sum_{n=1}^{\infty}(-k^2)^n\gamma_n(t)\right], \tag{D1}$$

where $\gamma_n(t)$ is related to a $2n$-point velocity time correlation function (TCF), such as

$$\gamma_1(t) = \int_0^t dt_1 \int_0^{t_1} dt_2 \langle v_k(t_2)v_k(t_1)\rangle = \int_0^t d\tau(t-\tau)\langle v_k(0)v_k(\tau)\rangle, \tag{D2}$$

and

$$\gamma_2(t) = \int_0^t dt_1 \int_0^{t_1} dt_2 \int_0^{t_2} dt_3 \int_0^{t_3} dt_4 \langle v_k(t_4)v_k(t_3)v_k(t_2)v_k(t_1)\rangle - \frac{1}{2}[\gamma_1(t)]^2, \tag{D3}$$

where $v_k = \vec{v}\cdot\vec{k}/k$. Note that $\hbar$ is shown explicitly here for clarity.

Now we differentiate Eq. (D1) with respect to t twice, and have

$$-\frac{1}{k^2}\frac{\partial^2 I(\vec{k},t)}{\partial t^2} = \ddot{\gamma}_1(t)e^{it\hbar k^2/2m} + o(k^2), \tag{D4}$$

where

$$\ddot{\gamma}_1(t) = \frac{1}{3}\langle\vec{v}(0)\cdot\vec{v}(t)\rangle, \tag{D5}$$

and $o(k^2)$ denotes the second and higher order terms in k. Note that the identity $\langle v_k(0)v_k(t)\rangle = \langle\vec{v}(0)\cdot\vec{v}(t)\rangle/3$ for isotropic systems is applied to get Eq. (D5). Then we also differentiate Eq.

(7.3) with respect to t twice, and obtain

$$\int_{-\infty}^{\infty} \frac{\omega^2}{k^2} S(\vec{k},\omega) e^{i\omega t} d\omega = -\frac{1}{k^2} \frac{\partial^2 I(\vec{k},t)}{\partial t^2}. \tag{D6}$$

Combining Eqs. (D4) and (D6), we have

$$\frac{\omega^2}{k^2} S(\vec{k},\omega) = \frac{1}{2\pi} \int_{-\infty}^{\infty} e^{-i\omega t} dt \left[\frac{1}{3} \langle \vec{v}(0) \cdot \vec{v}(t) \rangle e^{it\hbar k^2/2m} + o(k^2) \right], \tag{D7}$$

where the Fourier transform is inverted. Finally, taking the limit $k \to 0$ and employing the symmetry property of quantum TCFs, we reach Eq. (7.4).

Bibliography

[1] T. Bartels-Rausch, "Ten things we need to know about ice and snow." Nature **494**, 27 (2013).

[2] *SKYbrary: In-Flight Icing*, http://www.skybrary.aero/index.php/In-Flight_Icing.

[3] *Wikipedia: Air France Flight 447*, http://en.wikipedia.org/wiki/Air_France_Flight_447.

[4] J. G. Dash, H. Fu, and J. S. Wettlaufer, "The premelting of ice and its environmental consequences." Rept. Prog. Phys. **58**, 115 (1995).

[5] T. Bartels-Rausch, V. Bergeron, J. H. E. Cartwright et al., "Ice structures, patterns, and processes: A view across the icefields." Rev. Mod. Phys. **84**, 885 (2012).

[6] G. Malenkov, "Liquid water and ices: understanding the structure and physical properties." J. Phys. Cond. Matt. **21**, 283101 (2009).

[7] V. F. Petrenko and R. W. Whitworth, *Physics of Ice* (Oxford University Press: Oxford 1999).

[8] G. Tammann, "Ueber die Grenzen des festen Zustandes IV." Ann. Phys. **2**, 1 (1900).

[9] M. Chaplin, *Water structure and science*, http://www.lsbu.ac.uk/water/.

[10] S. J. Singer and C. Knight, "Hydrogen-bond topology and proton ordering in ice and water clusters." Adv. Chem. Phys. **147**, 1 (2012).

[11] J. D. Bernal and R. H. Fowler, "A Theory of Water and Ionic Solution, with Particular Reference to Hydrogen and Hydroxyl Ions." J. Chem. Phys. **1**, 515 (1933).

[12] L. Pauling, "The structure and entropy of ice and of other crystals with some randomness of atomic arrangement." J. Am. Chem. Soc. **57**, 2680 (1935).

[13] E. O. Wollan, W. L. Davidson, and C. G. Shull, "Neutron diffraction study of the structure of ice." Phys. Rev. **75**, 1348 (1949).

[14] S. T. Bramwell and M. J. P. Gingras, "Spin ice state in frustrated magnetic pyrochlore materials." Science **294**, 1495 (2001).

[15] M. J. P. Gingras, "Observing monopoles in a magnetic analog of ice." Science **326**, 375 (2009).

[16] A. Rahman and F. H. Stillinger, "Proton distribution in ice and the Kirkwood correlation factor." J. Chem. Phys. **57**, 4009 (1972).

[17] R. E. Shawyer and P. Dean, "Atomic vibrations in orientationally disordered systems: II. Hexagonal ice." J. Phys. C Solid State Phys. **5**, 1028 (1972).

[18] E. Cota and W. G. Hoover, "Computer simulation of hexagonal ice." J. Chem. Phys. **67**, 3839 (1977).

[19] M. D. Morse and S. A. Rice, "Tests of effective pair potentials for water: Predicted ice structures." J. Chem. Phys. **76**, 650 (1982).

[20] J. L. F. Abascal, R. G. Fernández, L. G. MacDowell et al., "Ice: a fruitful source of information about liquid water." J. Mol. Liq. **136**, 214 (2007).

[21] C. Vega, J. L. F. Abascal, M. M. Conde et al., "What ice can teach us about water interactions: a critical comparison of the performance of different water models." Faraday Discuss. **141**, 251 (2009).

[22] G. P. Johari and E. Whalley, "The dielectric properties of ice Ih in the range 272-133 K." J. Chem. Phys. **75**, 1333 (1981).

[23] J. L. Skinner, B. M. Auer, and Y.-S. Lin, "Vibrational line shapes and spectral diffusion in liquid water." Adv. Chem. Phys. **142**, 59 (2009).

[24] L. Wang, C. T. Middleton, M. T. Zanni et al., "Development and validation of transferable amide I vibrational frequency maps for peptides." J. Phys. Chem. B **115**, 3713 (2011).

[25] B. A. Lindquist, K. E. Furse, and S. A. Corcelli, "Nitrile groups as vibrational probes of biomolecular structure and dynamics: an overview." Phys. Chem. Chem. Phys. **11**, 8119 (2009).

[26] D. F. Hornig, H. F. White, and F. P. Reding, "The infrared spectra of crystalline H_2O, D_2O and HDO." Spectrochim. Acta Part A **12**, 338 (1958).

[27] C. Haas and D. F. Hornig, "Inter- and intramolecular potentials and the spectrum of ice." J. Chem. Phys. **32**, 1763 (1960).

[28] J. E. Bertie and E. Whalley, "Infrared sepctra of ices Ih and Ic." J. Chem. Phys. **40**, 1637 (1964).

[29] A. K. Soper, "The radial distribution functions of water and ice from 220 to 673 K and at pressures up to 400 MPa." Chem. Phys. **258**, 121 (2000).

[30] T. Förster, "Experimentelle und theoretische Untersuchung des zwischenmolekularen Übergangs von Elektronenanregungsenergie." Z. Naturforsch. A **4**, 321 (1949).

[31] R. L. A. Timmer and H. J. Bakker, "Vibrational Förster transfer in ice Ih." J. Phys. Chem. A **114**, 4148 (2010).

[32] S. G. Warren and R. E. Brandt, "Optical constants of ice from the ultraviolet to the microwave: a revised compilation." J. Geophys. Research **113**, D14220 (2008).

[33] C. P. Lawrence and J. L. Skinner, "Ultrafast infrared spectroscopy probes hydrogen-bonding dynamics in liquid water." Chem. Phys. Lett. **369**, 472 (2003).

[34] C. P. Lawrence and J. L. Skinner, "Vibrational spectroscopy of HOD in liquid D_2O. III. Spectral diffusion, and hydrogen-bonding and rotational dynamics." J. Chem. Phys. **118**, 264 (2003).

[35] F. Li and J. L. Skinner, "Infrared and Raman line shapes for ice Ih. I. Dilute HOD in H_2O and D_2O." J. Chem. Phys. **132**, 204505 (2010).

[36] F. Perakis, S. Widmer, and P. Hamm, "Two-dimensional infrared spectroscopy of isotope-diluted ice Ih." J. Chem. Phys. **134**, 204505 (2011).

[37] D. A. McQuarrie, *Statistical Mechanics* (Harper and Row: New York 1976).

[38] W. Marshall and S. W. Lovesey, *Theory of Thermal Neutron Scattering* (Oxford University Press: Ely House, London, UK 1971).

[39] G. L. Squires, *Introduction to the Theory of Thermal Neutron Scattering* (Cambridge University Press: Cambridge, UK 2012).

[40] P. A. Egelstaff, *Thermal Neutron Scattering* (Academic Press: New York, US 1965).

[41] S. Mukamel, *Principles of Nonlinear Optical Spectroscopy* (Oxford: New York 1995).

[42] B. M. Auer and J. L. Skinner, "Vibrational sum-frequency spectroscopy of the liquid/vapor interface for dilute HOD in D_2O." J. Chem. Phys. **129**, 214705 (2008).

[43] S. Abbate, G. Longhi, K. Kwon et al., "The use of cross-correlation functions in the analysis of circular dichroism spectra." J. Chem. Phys. **108**, 50 (1998).

[44] M. S. Bergren and S. A. Rice, "An improved analysis of the OH stretch region of the vibrational spectrum of ice Ih." J. Chem. Phys. **77**, 583 (1982).

[45] S. Rice, M. Bergren, A. Belch et al., "A theoretical analysis of the hydroxyl stretching spectra of ice Ih, liquid water, and amorphous solid water." J. Phys. Chem. **87**, 4295 (1983).

[46] S. Fritsch, R. Potestio, D. Donadio et al., "Nuclear quantum effects in water: A multiscale study." J. Chem. Th. Comp. **10**, 816 (2014).

[47] S. Habershon, G. S. Fanourgakis, and D. E. Manolopoulos, "Comparison of path integral molecular dynamics methods for the infrared absorption spectrum of liquid water." J. Chem. Phys. **129**, 074501 (2008).

[48] J. G. Kirkwood, "The dielectric polarization of polar liquids." J. Chem. Phys. **7**, 911 (1939).

[49] M. Neumann, "Dipole Moment Fluctuation Formulas in Computer Simulations of Polar Systems." Mol. Phys. **50**, 841 (1983).

[50] L. G. MacDowell and C. Vega, "Dielectric constant of ice Ih and ice V: A computer simulation study." J. Phys. Chem. B **114**, 6089 (2010).

[51] J. D. Jackson, *Classical Electrodynamics* (John Wiley and Sons: New York 1975).

[52] R. P. Auty and R. H. Cole, "Dielectric properties of ice and solid D_2O." J. Chem. Phys. **20**, 1309 (1952).

[53] G. P. Johari, "The dielectric properties of H_2O and D_2O ice Ih at MHz frequencies." J. Chem. Phys. **64**, 3998 (1976).

[54] J. M. Caillol, D. Levesque, and J. J. Weis, "Theoretical calculation of ionic solution properties." J. Chem. Phys. **85**, 6645 (1986).

[55] J. L. Aragones, L. G. MacDowell, and C. Vega, "Dielectric constant of ices and water: a lesson about water interactions." J. Phys. Chem. A **115**, 5745 (2011).

[56] C. P. Lawrence and J. L. Skinner, "Quantum corrections in vibrational and electronic condensed phase spectroscopy: Line shapes and echoes." Proc. Natl. Acad. Sci. USA **102**, 6720 (2005).

[57] S. A. Egorov and J. L. Skinner, "Semiclassical approximations to quantum time correlation functions." Chem. Phys. Lett. **293**, 469 (1998).

[58] C. P. Lawrence, A. Nakayama, N. Makri et al., "Quantum dynamics in simple fluids." J. Chem. Phys. **120**, 6621 (2004).

[59] S. A. Egorov, K. F. Everitt, and J. L. Skinner, "Quantum dynamics and vibrational relaxation." J. Phys. Chem. A **103**, 9494 (1999).

[60] R. Ramirez, T. Lopez-Ciudad, P. Kumar et al., "Quantum corrections to classical time-correlation functions: Hydrogen bonding and anharmonic floppy modes." J. Chem. Phys. **121**, 3973 (2004).

[61] G. S. Fanourgakis and S. S. Xantheas, "Development of transferable interaction potentials for water. V. Extension of the flexible, polarizable, Thole-type model potential (TTM3-F, v. 3.0) to describe the vibrational spectra of water clusters and liquid water." J. Chem. Phys. **128**, 074506 (2008).

[62] C. Zhang, D. Donadio, F. Gygi et al., "First principles simulations of the infrared spectrum of liquid water using hybrid density functionals." J. Chem. Th. Comp. **7**, 1443 (2011).

[63] C. Zhang, J. Wu, G. Galli et al., "Structural and vibrational properties of liquid water from van der Waals density functionals." J. Chem. Th. Comp. **7**, 3054 (2011).

[64] L.-P. Wang, T. L. Head-Gordon, J. W. Ponder et al., "Systematic Improvement of a Classical Molecular Model of Water." J. Phys. Chem. B **117**, 9956 (2013).

[65] F. Paesani and G. A. Voth, "The properties of water: Insights from quantum simulations." J. Phys. Chem. B **113**, 5702 (2009).

[66] F. Paesani, S. S. Xantheas, and G. A. Voth, "Infrared spectroscopy and hydrogen-bond dynamics of liquid water from centroid molecular dynamics with an ab initio-based force field." J. Phys. Chem. B **113**, 13118 (2009).

[67] S. Habershon, D. E. Manolopoulos, T. E. Markland et al., "Ring-polymer molecular dynamics: quantum effects in chemical dynamics from classical trajectories in an extended phase space." Annu. Rev. Phys. Chem. **64**, 387 (2013).

[68] J. G. Saven and J. L. Skinner, "A molecular theory of the line shape: Inhomogeneous and homogeneous electronic spectra of dilute chromophores in nonpolar fluids." J. Chem. Phys. **99**, 4391 (1993).

[69] C. P. Lawrence and J. L. Skinner, "Vibrational spectroscopy of HOD in liquid D_2O. II. Infrared line shapes and vibrational Stokes shift." J. Chem. Phys. **117**, 8847 (2002).

[70] M. Cho, "Correlation between electronic and molecular structure distortions and vibrational properties. I. Adiabatic approximations." J. Chem. Phys. **118**, 3480 (2003).

[71] S. Ham, J.-H. Kim, H. Lee et al., "Correlation between electronic and molecular structure distortions and vibrational properties. II. Amide I modes of NMA-nD_2O complexes." J. Chem. Phys. **118**, 3491 (2003).

[72] K. Kwac and M. Cho, "Molecular dynamics simulation study of N-methylacetamide in water. I. Amide I mode frequency fluctuation." J. Chem. Phys. **119**, 2247 (2003).

[73] U. Buck, I. Ettischer, M. Melzer et al., "Structure and spectra of three-dimensional $(H_2O)_n$ clusters, n=8,9,10." Phys. Rev. Lett. **80**, 2578 (1998).

[74] J. Sadlej, V. Buch, J. K. Kazimirski et al., "Theoretical study of the structure and spectra of cage clusters $(H_2O)_n$, n=7-10." J. Phys. Chem. A **103**, 4933 (1999).

[75] S. A. Corcelli, C. P. Lawrence, and J. L. Skinner, "Combined electronic structure/molecular dynamics approach for ultrafast infrared spectroscopy of dilute HOD in liquid H_2O and D_2O." J. Chem. Phys. **120**, 8107 (2004).

[76] J. R. Schmidt, Ph. D. thesis, University of Wisconsin, 2006.

[77] J.-H. Choi and M. Cho, "Computational IR spectroscopy of water: OH stretch frequencies, transition dipoles, and intermolecular vibrational coupling constants." J. Chem. Phys. **138**, 174108 (2013).

[78] S. M. Gruenbaum, C. J. Tainter, L. Shi et al., "Robustness of frequency, transition dipole, and coupling maps for water vibrational spectroscopy." J. Chem. Th. Comp. **9**, 3109 (2013).

[79] D. Colbert and W. H. Miller, "A Novel Discrete Variable Representation for Quantum Mechanical Reactive Scattering vi the S-Matrix Kohn Method." J. Chem. Phys. **96**, 1982 (1992).

[80] F. Li and J. L. Skinner, "Infrared and Raman line shapes for ice Ih. II. H_2O and D_2O." J. Chem. Phys. **133**, 244504 (2010).

[81] F. Li and J. L. Skinner, "Erratum: Infrared and Raman line shapes for ice Ih. II. H_2O and D_2O [J. Chem. Phys. 133, 244504 (2010)]." J. Chem. Phys. **134**, 099901 (2011).

[82] L. Shi, S. M. Gruenbaum, and J. L. Skinner, "Interpretation of IR and Raman line shapes for H_2O and D_2O ice Ih." J. Phys. Chem. B **116**, 13821 (2012).

[83] R. Kumar and J. L. Skinner, "Water simulation model with explicit three-molecule interactions." J. Phys. Chem. B **112**, 8311 (2008).

[84] C. J. Tainter, P. A. Pieniazek, Y.-S. Lin et al., "Robust three-body water simulation model." J. Chem. Phys. **134**, 184501 (2011).

[85] C. J. Tainter and J. L. Skinner, unpublished.

[86] Y. Ni and J. L. Skinner, unpublished.

[87] I. V. Stiopkin, C. Weeraman, P. A. Pieniazek et al., "Vibrational coupling and hydrogen bonding at the water surface revealed by isotopic dilution spectroscopy." Nature **474**, 192 (2011).

[88] P. A. Pieniazek, C. J. Tainter, and J. L. Skinner, "Surface of liquid water: Three-body interactions and vibrational sum-frequency spectrum." J. Am. Chem. Soc. **133**, 10360 (2011).

[89] P. A. Pieniazek, C. J. Tainter, and J. L. Skinner, "Interpretation of the water surface vibrational sum-frequency spectrum." J. Chem. Phys. **135**, 044701 (2011).

[90] C. J. Tainter and J. L. Skinner, "The water hexamer: Three-body interactions, structures, energetics, and OH-stretch spectroscopy at finite temperature." J. Chem. Phys. **137**, 104304 (2012).

[91] C. J. Tainter, L. Shi, and J. L. Skinner, "Structure and OH-stretch spectroscopy of low- and high-density amorphous ices." J. Chem. Phys. **140**, 134503 (2014).

[92] C. A. Coulson and D. Eisenberg, "Interaction of H_2O molecules in ice. I. The dipole moment of an H_2O molecule in ice." Proc. R. Soc. London A **291**, 445 (1966).

[93] D. P. Fernández, Y. Mulev, A. R. H. Goodwin et al., "A database for the static dielectric constant of water and steam." J. Phys. Chem. Ref. Data **24**, 33 (1995).

[94] J. L. F. Abascal and C. Vega, "A general purpose model for the condensed phases of water: TIP4P/2005." J. Chem. Phys. **123**, 234505 (2005).

[95] S. W. Rick and A. D. J. Haymet, "Dielectric constant and proton order and disorder in ice Ih: Monte Carlo computer simulations." J. Chem. Phys. **118**, 9291 (2003).

[96] G. E. Lindberg and F. Wang, "Efficient sampling of ice structures by electrostatic switching." J. Phys. Chem. B **112**, 6436 (2008).

[97] A. Y. Zasetsky and V. I. Gaiduk, "Study of temperature effect on far-infrared spectra of liquid H_2O and D_2O by analytical theory and molecular dynamics simulations." J. Phys. Chem. A **111**, 5599 (2007).

[98] J. E. Bertie, H. J. Labbé, and E. Whalley, "Absorptivity of ice I in the range of 4000-30 cm^{-1}." J. Chem. Phys. **50**, 4501 (1969).

[99] D. A. Draegert, N. W. B. Stone, B. Curnutte et al., "Far-infrared spectrum of liquid water." J. Opt. Soc. Am. **56**, 64 (1966).

[100] A. N. Rusk and D. Williams, "Optical constants of water in the infrared." J. Opt. Soc. Am. **61**, 895 (1971).

[101] M. N. Afsar and J. B. Hasted, "Measurements of the optical constants of liquid H_2O and D_2O between 6 and 450 cm^{-1}." J. Opt. Soc. Am. **67**, 902 (1977).

[102] H. R. Zelsmann, "Temperature dependence of the optical constants for liquid H_2O and D_2O in the far IR region." J. Mol. Struct. **350**, 95 (1995).

[103] J. E. Bertie and Z. Lan, "Infrared intensities of liquids XX: The intensity of the OH stretching band of liquid water revisited, and the best current values of the optical constants of H_2O(l) at 25 °C between 15,000 and 1 cm^{-1}." Appl. Spec. **50**, 1047 (1996).

[104] M. A. González and J. L. F. Abascal, "A flexible model for water based on TIP4P/2005." J. Chem. Phys. **135**, 224516 (2011).

[105] M. Praprotnik, D. Janezic, and J. Mavri, "Temperature dependence of water vibrational spectrum: A molecular dynamics simulation study." J. Phys. Chem. A **108**, 11056 (2004).

[106] Y. Wu, H. L. Tepper, and G. A. Voth, "Flexible simple point-charge water model with improved liquid-state properties." J. Chem. Phys. **124**, 024503 (2006).

[107] G. Raabe and R. J. Sadus, "Molecular dynamics simulation of the dielectric constant of water: the effect of bond flexibility." J. Chem. Phys. **134**, 234501 (2011).

[108] B. T. Thole, "Molecular Polarizabilites Calculated with a Modified Dipole Interaction." Chem. Phys. **59**, 341 (1981).

[109] A. Wallqvist and B. J. Berne, "Effective potentials for liquid water using polarizable and nonpolarizable models." J. Phys. Chem. **97**, 13841 (1993).

[110] S. W. Rick, S. J. Stuart, and B. J. Berne, "Dynamical fluctuating charge force fields: Application to liquid water." J. Chem. Phys. **101**, 6141 (1994).

[111] S. W. Rick, "Simulations of ice and liquid water over a range of temperatures using the fluctuating charge model." J. Chem. Phys. **114**, 2276 (2001).

[112] G. Lamoureux, A. D. MacKerell, and B. Roux, "A simple polarizable model of water based on classical Drude oscillators." J. Chem. Phys. **119**, 5185 (2003).

[113] H. Yu and W. F. van Gunsteren, "Accouting for polarization in molecular simulation." Comput. Phys. Commun. **172**, 69 (2005).

[114] F. Paesani, S. S. Xantheas, and G. A. Voth, "Infrared spectroscopy and hydrogen-bond dynamics of lquid water from centroid molecular dynamics with an ab initio-based force field." J. Phys. Chem. B **113**, 13118 (2009).

[115] T. Hasegawa and Y. Tanimura, "A polarizable water model for intramolecular and intermolecular vibrational spectroscopies." J. Phys. Chem. B **115**, 5545 (2011).

[116] A. J. Rusnak, E. R. Pinnick, C. E. Calderon et al., "Static dielectric constants and molecular dipole distributions of liquid water and ice-Ih investigated by the PAW-PEB exchange-correlation functional." J. Chem. Phys. **137**, 034510 (2012).

[117] G. Profeta and S. Scandolo, "Far-infrared spectrum of ice Ih: a first-principles study." Phys. Rev. B **84**, 024103 (2011).

[118] M. Heyden, J. Sun, S. Funkner et al., "Dissecting the THz spectrum of liquid water from first principles via correlations in time and space." Proc. Natl. Acad. Sci. USA **107**, 12068 (2010).

[119] M. Sharma, R. Resta, and R. Car, "Intermolecular dynamical charge fluctuations in water: a signature of the H-bond network." Phys. Rev. Lett. **95**, 187401 (2005).

[120] M. Sharma, R. Resta, and R. Car, "Erratum: intermolecular dynamical charge fluctuations in water: a signature of the H-bond netwok [Phys. Rev. Lett. 95, 187401 (2005)]." Phys. Rev. Lett. **100**, 019901 (2008).

[121] M. Sharma, R. Resta, and R. Car, "Dipolar correlations and the dielectric permittivity of water." Phys. Rev. Lett. **98**, 247401 (2007).

[122] W. Chen, M. Sharma, R. Resta et al., "role of dipolar correlations in the infrared spectra of water and ice." Phys. Rev. B **77**, 245114 (2008).

[123] P. L. Silvestrelli, M. Bernasconi, and M. Parrinello, "Ab initio infrared spectrum of liquid water." Chem. Phys. Lett. **277**, 478 (1997).

[124] C. Vega and J. L. F. Abascal, "Simulating water with rigid non-polarizable models: a general perspective." Phys. Chem. Chem. Phys. **13**, 19663 (2011).

[125] I. V. Leontyev and A. A. Stuchebrukhov, "Accounting for electronic polarization in non-polarizable force fields." Phys. Chem. Chem. Phys. **13**, 2613 (2011).

[126] J. Hayward and J. Reimers, "Unit cells for the simulation of hexagonal ice." J. Chem. Phys. **106**, 1518 (1997).

[127] V. Buch, P. Sandler, and J. Sadlej, "Simulations of H_2O Solid, Liquid, and Clusters, with an Emphasis on Ferroelectric Ordering Transition in Hexagonal Ice." J. Phys. Chem. B **102**, 8641 (1998).

[128] J.-L. Kuo, J. V. Coe, S. J. Singer et al., "On the use of graph invariants for efficiently generating hydrogen bond topologies and predicting physical properties of water clusters and ice." J. Chem. Phys. **114**, 2527 (2001).

[129] D. van der Spoel, E. Lindahl, B. Hess et al., *Gromacs User Manual version 3.3* (www.gromacs.org: 2005).

[130] H. J. C. Berendsen, J. P. M. Postma, W. F. van Gunsteren et al., "Molecular dynamics with coupling to an external bath." J. Chem. Phys. **81**, 3684 (1984).

[131] S. Miyamoto and P. A. Kollman, "Settle: An analytical version of the SHAKE and RATTLE algorithm for rigid water models." J. Comput. Chem. **13**, 952 (1992).

[132] T. Darden, D. York, and L. Pedersen, "Particle mesh Ewald: An N·log(N) method for Ewald sums in large systems." J. Chem. Phys. **98**, 10089 (1993).

[133] U. Essmann, L. Perera, M. L. Berkowitz et al., "A smooth particle mesh Ewald method." J. Chem. Phys. **103**, 8577 (1995).

[134] B. M. Auer and J. L. Skinner, "IR and Raman spectra of liquid water: Theory and interpretation." J. Chem. Phys. **128**, 224511 (2008).

[135] A. K. Soper and C. J. Benmore, "Quantum differences between heavy and light water." Phys. Rev. Lett. **101**, 065502 (2008).

[136] K. Ichikawa, Y. Kameda, T. Yamaguchi et al., "Neutron-diffraction investigation of the intramolecular structure of a water molecule in the liquid phase at high temperatures." Mol. Phys. **73**, 79 (1991).

[137] P. L. Silvestrelli and M. Parrinello, "Structural, electronic, and bonding properties of liquid water from first principles." J. Chem. Phys. **111**, 3572 (1999).

[138] M. A. Floriano, D. D. Klug, E. Whalley et al., "Direct determination of the intramolecular O-D distance in ice Ih and Ic by neutron diffraction." Nature **329**, 821 (1987).

[139] G. S. Fanourgakis and S. S. Xantheas, "The bend angle of water in ice Ih and liquid water: the significance of implementing the nonlinear monomer dipole moment surface in classical interaction potentials." J. Chem. Phys. **124**, 174504 (2006).

[140] S. A. Clough, Y. Beers, G. P. Klein et al., "Dipole moment of water from Stark measurements of H_2O, HDO, and D_2O." J. Chem. Phys. **59**, 2254 (1973).

[141] Y. S. Badyal, M.-L. Saboungi, D. L. Price et al., "Electron distribution in water." J. Chem. Phys. **112**, 9206 (2000).

[142] A. V. Gubskaya and P. G. Kusalik, "The total molecular dipole moment for liquid water." J. Chem. Phys. **117**, 5290 (2002).

[143] P. Barnes, J. L. Finney, J. D. Nicholas et al., "Cooperative effects in simulated water." Nature **282**, 459 (1979).

[144] S. L. Carnie and G. N. Patey, "Fluids of polarizable hard spheres with dipoles and tetrahedral quadrupoles integral equation results with application to liquid water." Mol. Phys. **47**, 1129 (1982).

[145] M. Sprik and M. L. Klein, "A polarizable model for water using distributed charge sites." J. Chem. Phys. **89**, 7556 (1988).

[146] K. Watanabe and M. L. Klein, "Effective pair potentials and the properties of water." Chem. Phys. **131**, 157 (1989).

[147] P. Ahlström, A. Wallqvist, S. Engström et al., "A molecular dynamics study of polarizable water." Mol. Phys. **68**, 563 (1989).

[148] M. Sprik, "Hydrogen bonding and the static dielectric constant in liquid water." J. Chem. Phys. **95**, 6762 (1991).

[149] K. Laasonen, M. Sprik, and M. Parrinello, "Ab initio liquid water." J. Chem. Phys. **99**, 9080 (1993).

[150] D. Wei and D. R. Salahub, "A combined density functional and molecular dynamics simulation of a quantum water molecule in aqueous solution." Chem. Phys. Lett. **224**, 291 (1994).

[151] D. N. Bernardo, Y. Ding, K. Krogh-Jespersen et al., "An anisotropic polarizable water model: incorporation of all-atom polarizabilities into molecular mechanics force fields." J. Phys. Chem. **98**, 4180 (1994).

[152] I. M. Svishchev, P. G. Kusalik, J. Wang et al., "Polarizable point charge model for water: results under normal and extreme conditions." J. Chem. Phys. **105**, 4742 (1996).

[153] A. A. Chialvo and P. T. Cummings, "Engineering a simple polarizable model for the molecular simulation of water applicable over wide ranges of state conditions." J. Chem. Phys. **105**, 8274 (1996).

[154] B. D. Bursulaya, J. Jeon, D. A. Zichi et al., "Generalized molecular mechanics including quantum electronic structure variation of polar solvents. II. A molecular dynamics simulation study of water." J. Chem. Phys. **108**, 3286 (1998).

[155] P. L. Silvestrelli and M. Parrinello, "Water molecule dipole in the gas and in the liquid phase." Phys. Rev. Lett. **82**, 3308 (1999).

[156] L. Delle Site, A. Alavi, and R. M. Lynden-Bell, "The electrostatic properties of water molecules in condensed phases: an ab initio study." Mol. Phys. **96**, 1683 (1999).

[157] Y. Tu and A. Laaksonen, "The electronic properties of water molecules in water clusters and liquid water." Chem. Phys. Lett. **329**, 283 (2000).

[158] A. V. Gubskaya and P. G. Kusalik, "The multipole polarizabilities and hyperpolarizabilities of the water molecule in liquid state: an ab initio study." Mol. Phys. **99**, 1107 (2001).

[159] E. Harder, J. D. Eaves, A. Tokmakoff et al., "Polarizable molecules in the vibrational spectroscopy of water." Proc. Natl. Acad. Sci. USA **102**, 11611 (2005).

[160] J. A. Morrone and R. Car, "Nuclear quantum effects in water." Phys. Rev. Lett. **101**, 017801 (2008).

[161] W. Yu, P. E. M. Lopes, B. Roux et al., "Six-site polarizable model of water based on the classical Drude oscillator." J. Chem. Phys. **138**, 034508 (2013).

[162] L. Onsager and M. Dupuis, *The electrical properties of ice* (In Electrolytes, ed. by B. Pesce (Pergamon, Oxford, 1962): London 1962).

[163] E. Whalley, "A relation between the strengths of the orientation polarization and the infrared absorption of the O-H stretching vibrations of ice." Chem. Phys. Lett. **53**, 449 (1978).

[164] D. J. Adams, "Theory of the dielectric constant of ice." Nature **293**, 447 (1981).

[165] M. I. Heggie, C. D. Latham, S. C. P. Maynard et al., "Cooperative polarisation in ice Ih and the unusual strength of the hydrogen bond." Chem. Phys. Lett. **249**, 485 (1996).

[166] J. K. Gregory, D. C. Clary, K. Liu et al., "The water dipole moment in water clusters." Science **275**, 814 (1997).

[167] E. R. Batista, S. S. Xantheas, and H. Jónsson, "Molecular multipole moments of water molecules in ice Ih." J. Chem. Phys. **109**, 4546 (1998).

[168] E. R. Batista, S. S. Xantheas, and H. Jónsson, "Multipole moments of water molecules in clusters and ice Ih from first principles calculations." J. Chem. Phys. **111**, 6011 (1999).

[169] E. R. Batista, S. S. Xantheas, and H. Jónsson, "Electric fields in ice and near water clusters." J. Chem. Phys. **112**, 3285 (2000).

[170] M. W. Severson, J. P. Devlin, and V. Buch, "Librational modes of ice I." J. Chem. Phys. **119**, 4449 (2003).

[171] B. Pamuk, J. M. Soler, R. Ramírez et al., "Anomalous nuclear quantum effects in ice." Phys. Rev. Lett. **108**, 193003 (2012).

[172] H. J. Prask, S. F. Trevino, J. D. Gault et al., "Ice I - lattice dynamics and incoherent neutron scattering." J. Chem. Phys. **56**, 3217 (1972).

[173] D. D. Klug, E. Whalley, E. C. Svensson et al., "Densities of vibrational states and heat capacities of crystalline and amorphous H_2O ice determined by neutron scattering." Phys. Rev. B **44**, 841 (1991).

[174] D. D. Klug, J. S. Tse, and E. Whalley, "The longitudinal-optic-transverse-optic mode splitting in ice Ih." J. Chem. Phys. **95**, 7011 (1991).

[175] S. Imoto, S. S. Xantheas, and S. Saito, "Molecular origin of the difference in the HOH bend of the IR spectra between liquid water and ice." J. Chem. Phys. **138**, 054506 (2013).

[176] J.-C. Li, "Inelastic neutron scattering studies of hydrogen bonding in ices." J. Chem. Phys. **105**, 6733 (1996).

[177] P. Zhang, L. Tian, Z. P. Zhang et al., "Investigation of the hydrogen bonding in ice Ih by first-principles density functional methods." J. Chem. Phys. **137**, 044504 (2012).

[178] H. Liu, Y. Wang, and J. M. Bowman, "Vibrational Analysis of an Ice Ih Model from 0 to 4000 cm^{-1} Using the Ab initio WHBB Potential Energy Surface." J. Phys. Chem. B **117**, 10046 (2013).

[179] M. J. Taylor and E. Whalley, "Raman Spectra of Ices Ih, Ic, II, III, and V." J. Chem. Phys. **40**, 1660 (1964).

[180] T.A. Ford and M. Falk, "Hydrogen bonding in water and ice." Can. J. Chem. **46**, 3579 (1968).

[181] P. Wong and E. Whalley, "optical spectra of orientationally disordered crystal." J. Chem. Phys. **62**, 2418 (1975).

[182] J. G. Scherer and R. G. Snyder, "Raman intensities of single crystal ice Ih." J. Chem. Phys. **67**, 4794 (1977).

[183] E. Whalley, "A detailed assignment of the O-H stretching bands of ice i." Can. J. Chem. **55**, 3429 (1977).

[184] T. C. Sivakumar, D. Schuh, M. G. Sceats et al., "The 2500-4000 cm^{-1} Raman and infrared spectra of low density amorphous solid water and of polycrystalline ice I." Chem. Phys. Lett. **48**, 212 (1977).

[185] M. S. Bergren, D. Schuh, M. G. Sceats et al., "the oh stretching region infrared spectra of low density amorphous solid water and polycrystalline ice ih." J. Chem. Phys. **69**, 3477 (1978).

[186] T. C. Sivakumar, S. A. Rice, and M. G. Sceats, "Raman spectroscopic studies of the OH stretching region." J. Chem. Phys. **69**, 3468 (1978).

[187] T. C. Sivakumar, H. A. M. Chew, and G. P. Johari, "Effect of pressure on the Raman spectrum of ice." Nature **275**, 524 (1978).

[188] B. Minceva-Sukarova, W. F. Sherman, and G. R. Wilkinson, "The Raman spectra of ice (Ih, II, III, V, VI and IX) as functions of pressure and temperature." J. Phys. C Solid State Phys. **17**, 5833 (1984).

[189] V. Buch and J. P. Devlin, "A new interpretation of the OH-stretch spectrum of ice." J. Chem. Phys. **110**, 3437 (1999).

[190] H. Iglev, M. Schmeisser, K. Simeonidas et al., "Ultrafast superheating and melting of bulk ice." Nature **439**, 183 (2006).

[191] K. Furic and V. Volovsek, "Water ice at low temperatures and pressures: New Raman results." J. Mol. Struct. **976**, 174 (2010).

[192] F. Perakis and P. Hamm, "Two-dimensional infrared spectroscopy of neat ice Ih." Phys. Chem. Chem. Phys. **14**, 6250 (2012).

[193] T. Shigenari and K. Abe, "Vibrational modes of hydrogens in the proton ordered phase XI of ice: Raman spectra above 400 cm^{-1}." J. Chem. Phys. **136**, 174504 (2012).

[194] R. McGraw, W. G. Madden, S. A. Rice et al., "An interpretation of the OH stretching region of the vibrational spectrum of ice I." Chem. Phys. Lett. **48**, 219 (1977).

[195] R. McGraw, W. Madden, M. Bergren et al., "A theoretical study of the OH stretching region of the vibrational spectrum of ice Ih." J. Chem. Phys. **69**, 3483 (1978).

[196] M. G. Sceats, M. Stavola, and S. A. Rice, "On the role of Fermi resonance in the spectrum of water in its condensed phases." J. Chem. Phys. **71**, 983 (1979).

[197] M. J. Wójcik, K. Szczeponek, and S. Ikeda, "Theoretical study of the OH/OD stretching regions of the vibrational spectra of ice Ih." J. Chem. Phys. **117**, 9850 (2002).

[198] R. Iftimie and M. E. Tuckerman, "Decomposing total IR spectra of aqueous systems into solute and solvent contributions: A computational approach using maximally localized Wannier orbitals." J. Chem. Phys. **122**, 214508 (2005).

[199] V. Buch, A. Milet, R. Vácha et al., "Water surface is acidic." Proc. Natl. Acad. Sci. USA **104**, 7342 (2007).

[200] E. B. Wilson, J. C. Decius, and P. C. Cross, *Molecular Vibrations* (Dover: New York 1980).

[201] J-C. Li and D. K. Ross, "Evidence for two kinds of hydrogen bond in ice." Nature **365**, 327 (1993).

[202] S. W. Rick, "Simulations of proton order and disorder in ice Ih." J. Chem. Phys. **122**, 094504 (2005).

[203] J. C. Li, S. M. Bennington, and D. K. Ross, "Further evidence for the existence of two kinds of H-bonds in ice Ih." Phys. Lett. A **192**, 295 (1994).

[204] J. S. Tse and D. D. Klug, "Comments on 'Further evidence for the existence of two kinds of H-bonds in ice Ih' by Li et al." Phys. Lett. A **198**, 464 (1995).

[205] S. Klotz, T. Strassle, C. G. Salzmann et al., "Incoherent inelastic neutron scattering measurements on ice VII: Are there two kinds of hydrogen bonds in ice?." Europhys. Lett. **74**, 576 (2005).

[206] J. J. Sakurai, *Modern Quantum Mechanics, Revised Edition* (Addison-Wesley: New York 1994).

[207] M. Yang and J. L. Skinner, "Signatures of coherent energy transfer in IR and Raman line shapes for liquid water." Phys. Chem. Chem. Phys. **12**, 982 (2010).

[208] R. Ramirez and C. P. Herrero, "Kinetic energy of protons in ice Ih and water: A path integral study." Phys. Rev. B **84**, 064130 (2011).

[209] Q. Waheed and O. Edholm, "Quantum Corrections to Classical Molecular Dynamics Simulations of Water and Ice." J. Chem. Th. Comp. **7**, 2903 (2011).

[210] C. P. Herrero and R. Ramirez, "Isotope effects in ice Ih: A path-integral simulation." J. Chem. Phys. **134**, 094510 (2011).

[211] G. Ritzhaupt and J. P. Devlin, "Infrared spectrum of D2O vibrationally decoupled in glassy H2O." J. Chem. Phys. **67**, 4779 (1977).

[212] J. Hernandez, N. Uras, and J. P. Devlin, "Molecular bending mode frequencies of the surface and interior of crystalline ice." J. Chem. Phys. **108**, 4525 (1998).

[213] K. Blum, *Density matrix theory and applications* (Plenum Press: New York and London 1980).

[214] R. Zwanzig, *Nonequilibrium statistical mechanics* (Oxford University Press: New York 2001).

[215] M. Yang and G. R. Fleming, "Influence of phonons on exciton transfer dynamics: comparison of the Redfield, Förster, and modified Redfield equations." Chem. Phys. **282**, 163 (2002).

[216] A. Ishizaki and G. R. Fleming, "On the adequacy of the Redfield equation and related approaches to the study of quantum dynamics in electronic energy transfer." J. Chem. Phys. **130**, 234110 (2009).

[217] S. Jang, "Generalization of the Förster resonance energy transfer theory for quantum mechanical modulation of the donor-acceptor coupling." J. Chem. Phys. **127**, 174710 (2007).

[218] A. G. Redfield, "On the theory of relaxation processes." IBM Jr. **1**, 19 (1957).

[219] G. Lindblad, "On the generators of quantum dynamical semigroups." Commun. Math. Phys. **48**, 119 (1976).

[220] V. Gorini, A Kossokowski, and E. C. G. Sudarshan, "Completely positive dynamical semigroups of N-level systems." J. Math. Phys. **17**, 821 (1976).

[221] V. Botan, E. H. G. Backus, R. Pfister et al., "Energy transport in peptide helices." Proc. Natl. Acad. Sci. USA **104**, 12749 (2007).

[222] E. H. G. Backus, P. H. Nguyen, V. Botan et al., "Energy transport in peptides helices: A comparison between high- and low-energy excitations." J. Phys. Chem. B **112**, 9091 (2008).

[223] E. H. G. Backus, P. H. Nguyen, V. Botan et al., "Structural flexibility of a helical peptide regulates vibrational energy transport properties." J. Phys. Chem. B **112**, 15487 (2008).

[224] M. Schade, A. Moretto, P. M. Donaldson et al., "Vibrational energy transport through a capping layer of appropriately designed peptide helices over gold nanoparticles." Nano Lett. **10**, 3057 (2010).

[225] S. Woutersen and H. J. Bakker, "Resonant intermolecular transfer of vibrational energy in liquid water." Nature **402**, 507 (1999).

[226] L. Piatkowski, K. B. Eisenthal, and H. J. Bakker, "Ultrafast intermolecular energy transfer in heavy water." Phys. Chem. Chem. Phys. **11**, 9033 (2009).

[227] M. L. Cowan, B. D. Bruner, N. Huse et al., "Ultrafast memory loss and energy redistribution in the hydrogen bond network of liquid H_2O." Nature **434**, 199 (2005).

[228] D. Kraemer, M. L. Cowan, A. Paarmann et al., "Temperature dependence of the two-dimensional infrared spectrum of liquid H_2O." Proc. Natl. Acad. Sci. USA **105**, 437 (2008).

[229] W. Amir, G. Gallot, and F. Hache, "Libration induced stretching mode excitation for pump-probe spectroscopy in pure liquid water." J. Chem. Phys. **121**, 7908 (2004).

[230] M. Yang, F. Li, and J. L. Skinner, "Vibrational energy transfer and anisotropy decay in liquid water: Is the Förster model valid?." J. Chem. Phys. **135**, 164505 (2011).

[231] J. A. Poulsen, G. Nyman, and S. Nordholm, "Wave packet study of ultrafast relaxation in ice Ih and liquid water. Resonant intermolecular vibrational energy transfer." J. Phys. Chem. A **107**, 8420 (2003).

[232] C. Backtorp, J. A. Poulsen, and G. Nyman, "Direct dynamics study of ultrafast vibrational energy relaxation in ice Ih." J. Phys. Chem. A **109**, 3105 (2005).

[233] J. W. Pyper and L. D. Christensen, "Equilibrium constants of hydrogen-deuterium-tritium self-exchange reactions in water vapor as studied with a pulsed molecular-beam quadrupole mass filter." J. Chem. Phys. **62**, 2596 (1975).

[234] J. C. Duplan, L. Mahi, and J. L. Brunet, "NMR determination of the equilibrium constant for the liquid H_2O-D_2O mixture." Chem. Phys. Lett. **413**, 400 (2005).

[235] E. N. Zimanyi and R. J. Silbey, "Theoretical description of quantum effects in multi-chromophoric aggregrates." Phil. Trans. R. Soc. A **370**, 3620 (2012).

[236] D. E. Rosenfeld and M. D. Fayer, "Excitation transfer induced spectral diffusion and the influence of structural spectral diffusion." J. Chem. Phys. **137**, 064109 (2012).

[237] T. L. C. Jansen, B. M. Auer, M. Yang et al., "Two-dimensional infrared spectroscopy and ultrafast anisotropy decay of water." J. Chem. Phys. **132**, 224503 (2010).

[238] M. Grover and R. Silbey, "Exciton migration in molecular crystals." J. Chem. Phys. **54**, 4843 (1971).

[239] V. M. Kenkre and P. Reineker, *Exciton Dynamics in Molecular Crystals and Aggregates* (Springer-Verlag: Berlin, Germany 1982).

[240] M. D. Fayer, *In: Spectroscopy and Excitation Dynamics of Condensed Molecular Systems, ed. V. M. Agranovich and R. M. Hochstrasser* (North-Holand: Amsterdam 1983).

[241] L. Shi and J. L. Skinner, "Proton Disorder in Ice Ih and Inhomogeneous Broadening in Two-Dimensional Infrared Spectroscopy." J. Phys. Chem. B **117**, 15536 (2013).

[242] S. Woutersen, U. Emmerichs, H.-K. Nienhuys et al., "Anomalous temperature dependence of vibrational lifetimes in water and ice." Phys. Rev. Lett. **81**, 1106 (1998).

[243] D. Hsu and J. L. Skinner, "On the thermal broadening of zero-phonon impurity lines in absorption and fluorescence spectra." J. Chem. Phys. **81**, 1604 (1984).

[244] D. Hsu and J. L. Skinner, "Nonperturbative theory of temperature-dependent optical dephasing in crystals. I. Acoustic or optical phonons." J. Chem. Phys. **81**, 5471 (1984).

[245] G. Seifert, K. Weidlich, and H. Graener, "Picosecond ir hole-burning spectroscopy on HDO ice Ih." Phys. Rev. B **56**, (1997).

[246] P. Hamm and M. Zanni, *Concepts and methods of 2D infrared spectroscopy* (Cambridge University Press: Cambridge, UK 2011).

[247] F. Perakis and P. Hamm, private communication.

[248] A. Dokter and H. Bakker, "Transient absorption of vibrationally excited ice ih." J. Chem. Phys. **128**, 024502 (2008).

[249] J. D. Eaves, J. J. Loparo, C. J. Fecko et al., "Hydrogen bonds in liquid water are broken only fleetingly." Proc. Natl. Acad. Sci. USA **102**, 13019 (2005).

[250] J. B. Asbury, T. Steinel, C. Stromberg et al., "Water dynamics: Vibrational echo correlation spectroscopy and comparison to molecular dynamics simulations." J. Phys. Chem. A **108**, 1107 (2004).

[251] C. J. Fecko, J. J. Loparo, S. T. Roberts et al., "Local hydrogen bonding dynamics and collective reorganization in water: Ultrafast infrared spectroscopy of HOD/D_2O." J. Chem. Phys. **122**, 054506 (2005).

[252] C. J. Fecko, J. D. Eaves, J. J. Loparo et al., "Ultrafast hydrogen-bond dynamics in the infrared spectroscopy of water." Science **301**, 1698 (2003).

[253] W. P. de Boeij, M. S. Pshenichnikov, and D. A. Wiersma, "On the relation between the echo-peak shift and Brownian-oscillator correlation function." Chem. Phys. Lett. **253**, 53 (1996).

[254] M. Cho, J.-Y. Yu, T. Joo et al., "The integrated photon echo and solvation dynamics." J. Phys. Chem. **100**, 11944 (1996).

[255] T. Joo, Y. Jia, J. Yu et al., "Third-order nonlinear time domain probes of solvation dynamics." J. Chem. Phys. **104**, 6089 (1996).

[256] A. Piryatinski and J. L. Skinner, "Determining vibrational solvation-correlation functions from three-pulse infrared photon echoes." J. Phys. Chem. B **106**, 8055 (2002).

[257] S. Li, J. R. Schmidt, A. Piryatinski et al., "Vibrational spectral diffusion of azide in water." J. Phys. Chem. B **110**, 18933 (2006).

[258] W. H. Press, S. A. Teukolsky, W. T. Vetterling et al., *Numerical Recipes in Fortran* (Cambridge University Press: 1992).

[259] P. C. H. Mitchell, S. F. Parker, A. J. Ramirez-Cuesta et al., *Vibrational Spectroscopy with Neutrons With Applications in Chemistry, Biology, Materials Science and Catalysis* (World Scientific Publishing Co. Pte. Ltd.: Singapore 2005).

[260] A. K. Soper, F. Bruni, and M. A. Ricci, "Site-site pair correlation functions of water from 25 to 400 C: Revised analysis of new and old diffraction data." J. Chem. Phys. **106**, 247 (1997).

[261] S. F. Parker, D. Lennon, and P. W. Albers, "Vibrational spectroscopy with neutrons: a review of new directions." Appl. Spec. **65**, 1325 (2011).

[262] C. M. Brown, A. J. Ramirez-Cuesta, M. R. Johnson et al., "Chemical spectroscopy using neutrons." Chem. Phys. **427**, 1 (2013).

[263] J.-C. Li, J. D. Londono, D. K. Ross et al., "An inelastic incoherent neutron scattering study of ice II, IX, V, and VI - in the range from 2 to 140 meV." J. Chem. Phys. **94**, 6770 (1991).

[264] J.-C. Li, V. M. Nield, and S. M. Jackson, "Spectroscopic measurements of ice XI." Chem. Phys. Lett. **241**, 290 (1995).

[265] J.-C. Li, C. Burnham, A. I. Kolesnikov et al., "Neutron spectroscopy of ice VIII in the region of 20-500 meV." Phys. Rev. B **59**, 9088 (1999).

[266] Y. Wang, A. I. Kolesnikov, S. L. Dong et al., "Neutron-scattering studies of the phase transitions in high-pressure ices during annealing." Can. J. Phys. **81**, 401 (2003).

[267] J. S. Tse, M. L. Klein, and I. R. McDonald, "Lattice vibrations of ices Ih, VIII, and IX." J. Chem. Phys. **81**, 6124 (1984).

[268] A. Criado, F. J. Bermejo, M. García-Hernández et al., "Phonon dispersion in polycrystalline ice: Implications for the collective behavior of liquid water." Phys. Rev. E **47**, 3516 (1993).

[269] H. Itoh, K. Kawamura, T. Hondoh et al., "Molecular dynamics studies of proton ordering effects on lattice vibrations in ice Ih." Physica B **219**, 469 (1996).

[270] I. Morrison and S. Jenkins, "First principles lattice dynamics studies of the vibrational spectra of ice." Physica B **263**, 442 (1999).

[271] S. Jenkins and I. Morrison, "The dependence on structure of the projected vibrational density of states of various phases of ice as calculated by *ab initio* methods." J. Phys. Cond. Matt. **13**, 9207 (2001).

[272] A. S. Cote, I. Morrison, X. Cui et al., "Ab-initio density-functional lattice-dynamics studies of ice." Can. J. Phys. **81**, 115 (2003).

[273] A. Erba, S. Casassa, R. Dovesi et al., "Periodic density functional theory and local-MP2 study of the librational modes of ice XI." J. Chem. Phys. **130**, 074505 (2009).

[274] L. Tian, A. I. Kolesnikov, and J. Li, "Ab initio simulation of hydrogen bonding in ices under ultra-high pressure." J. Chem. Phys. **137**, 204507 (2012).

[275] X. He, O. Sode, S. S. Xantheas et al., "Second-order many-body perturbation study of ice Ih." J. Chem. Phys. **137**, 204505 (2012).

[276] K. Gilliard, O. Sode, and S. Hirata, "Second-order many-body perturbation and coupled-cluster singles and doubles study of ice VIII." J. Chem. Phys. **140**, 174507 (2014).

[277] A. Pietropaolo, R. Senesi, C. Andreani et al., "Excess of proton mean kinetic energy in supercooled water." Phys. Rev. Lett. **100**, 127802 (2008).

[278] A. K. Soper, "Comment on "Excess of Proton Mean Kinetic Energy in Supercooled Water"." Phys. Rev. Lett. **103**, 069801 (2009).

[279] A. Pietropaolo, R. Senesi, C. Andreani et al., "Pietropaolo *et al.* Reply." Phys. Rev. Lett. **103**, 068902 (2009).

[280] A. Pietropaolo, R. Senesi, C. Andreani et al., "Quantum effects in water: proton kinetic energy maxima in stable and supercooled liquid." Braz. J. Phys. **39**, 318 (2009).

[281] D. Flammini, M. A. Ricci, and F. Bruni, "A new water anomaly: the temperature dependence of the proton mean kinetic energy." J. Chem. Phys. **130**, 236101 (2009).

[282] R. Ramírez and C. P. Herrero, "Kinetic energy of protons in ice Ih and water: a path integral study." Phys. Rev. B **84**, 064130 (2011).

[283] R. Senesi, D. Flammini, A. I. Kolesnikov et al., "The quantum nature of the OH stretching mode in ice and water probed by neutron scattering experiments." J. Chem. Phys. **139**, 074504 (2013).

[284] L. van Hove, "Correlations in space and time and Born approximation scattering in systems of interacting particles." Phys. Rev. **95**, 249 (1954).

[285] *Inelastic Scattering of Neutrons in Solids and Liquids* (International Atomic Energy Agency: Vienna 1961).

[286] A. Rahman, K. S. Singwi, and A. Sjölander, "Theory of slow neutron scattering by liquid. I." Phys. Rev. **126**, 986 (1962).

[287] J. I. Marquez Damian, D. C. Malaspina, and J. R. Granada, "Vibrational spectra of light and heavy water with application to neutron cross section calculations." J. Chem. Phys. **139**, 024504 (2013).

[288] E. J. Heller, J. R. Reimers, and G. Drolshagen, "Classical and semiclassical approximations for incoherent neutron scattering." Phys. Rev. A **36**, 2613 (1987).

[289] T. D. Hone and G. A. Voth, "A centroid molecular dynamics study of liquid para-hydrogen and ortho-deuterium." J. Chem. Phys. **121**, 6412 (2004).

[290] I. R. Craig and D. E. Manolopoulos, "Inelastic neutron scattering from liquid para-hydrogen by ring polymer molecular dynamics." Chem. Phys. **322**, 236 (2006).

[291] J. Liu and W. H. Miller, "Test of the consistency of various linearized semiclassical initial value time correlation functions in application to inelastic neutron scattering from liquid para-hydrogen." J. Chem. Phys. **128**, 144511 (2008).

[292] S. Bratos, G. Tarjus, M. Diraison et al., "Incoherent inelastic neutron scattering from liquid water: a theoretical study." Phys. Rev. A **44**, 2745 (1991).

[293] S. Bratos, M. Diraison, G. Tarjus et al., "Incoherent inelastic neutron scattering from liquid water: a theoretical investigation." Phys. Rev. A **45**, 5556 (1992).

[294] G. Tarjus, M. Diraison, J.-Cl. Leicknam et al., "Inelastic neutron scattering from liquid water. Theory and simulation." J. Mol. Struct. **296**, 199 (1993).

[295] M. Diraison, J.-Cl. Leicknam, G. Tarjus et al., "Computer simulation study of inelastic neutron scattering from liquid water." Phys. Rev. E **50**, 2689 (1994).

[296] M. Parrinello and A. Rahman, "Strain fluctuations and elastic-constants." J. Chem. Phys. **76**, 2662 (1982).

[297] S. Nosé, "A molecular dynamics method for simulations in the canonical ensemble." Mol. Phys. **52**, 255 (1984).

[298] W. G. Hoover, "Canonical dynamics – equilibrium phase-space distributions." Phys. Rev. A **31**, 1695 (1985).

[299] M. A. Ricci, M. Nardone, A. Fontana et al., "Light and neutron scattering studies of the OH stretching band in liquid and supercritical water." J. Chem. Phys. **108**, 450 (1998).

[300] E. Perelli-Cippo, G. Gorini, M. Tardocchi et al., "The O-H stretching band in ice Ih derived via eV neutron spectroscopy on VESUVIO using the new very low angle detector bank." Appl. Phys. A **83**, 453 (2006).

[301] G. E. Walrafen, Y. C. Chu, and G. J. Piermarini, "Low-frequency Raman scattering from water at high pressures and high temperatures." J. Phys. Chem. **100**, 10363 (1996).

[302] R. Zhang, A. Khalizov, L. Wang et al., "Nucleation and growth of nanoparticles in the atmosphere." Chem. Rev. **112**, 1957 (2012).

[303] M.-C. Bellissent-Funel, S. H. Chen, and J.-M. Zanotti, "Single-particle dynamics of water molecules in confined space." Phys. Rev. E **51**, 4558 (1995).

[304] A. G. Novikov, A. A. Van'kov, and L. S. Gosteva, "Temperature dependence of the general spectrum for water." J Struct Chem **31**, 77 (1990).

[305] M.-C. Bellissent-Funel and J. Teixeira, "Dynamics of water studied by coherent and incoherent inelastic neutron scattering." J. Mol. Struct. **250**, 213 (1991).

[306] F. H. Stillinger, "Water revisited." Science **209**, 451 (1980).

[307] R. Kumar, J. R. Schmidt, and J. L. Skinner, "Hydrogen bonding definitions and dynamics in liquid water." J. Chem. Phys. **126**, 204107 (2007).

[308] K. Iwano, T. Yokoo, M. Oguro et al., "Propagating librations in ice XI: model analysis and coherent inelastic neutron scattering experiment." J. Phys. Soc. Jap. **79**, 063601 (2010).

[309] K. Abe and T. Shigenari, "Raman spectra of proton ordered phase XI of ice I. Translational vibrations below 350 cm^{-1}." J. Chem. Phys. **134**, 104506 (2011).

[310] A. Shalit, F. Perakis, and P. Hamm, "Two-Dimensional Infrared Spectroscopy of Isotope-Diluted Low Density Amorphous Ice." J. Phys. Chem. B **117**, 15512 (2013).

[311] A. Shalit, F. Perakis, and P. Hamm, "Communication: Disorder-suppressed vibrational relaxation in vapor-deposited high-density amorphous ice." J. Chem. Phys. **140**, 151102 (2014).

[312] P. W. Anderson, "Absence of diffusion in certain random lattices." Phys. Rev. **109**, 1492 (1958).

[313] J. L. Skinner, "Models of Anderson localization." J. Phys. Chem. **98**, 2503 (1994).

[314] T. F. Kahan, J. P. Reid, and D. J. Donaldson, "Spectroscopic probes of the quasi-liquid layer on ice." J. Phys. Chem. A **111**, 11006 (2007).

[315] X. Wei, P. B. Miranda, and Y. R. Shen, "Surface vibrational spectroscopic study of surface melting of ice." Phys. Rev. Lett. **86**, 1554 (2001).

[316] X. Wei and Y. R. Shen, "Vibrational spectroscopy of ice interfaces." Appl. Phys. B **74**, 617 (2002).

[317] H. Groenzin, I. Li, V. Buch et al., "The single-crystal, basal face of ice Ih investigated with sum frequency generation." J. Chem. Phys. **127**, 214502 (2007).

[318] H. Groenzin, I. Li, and M. J. Shultz, "Sum-frequency generation: Polarization surface spectroscopy analysis of the vibrational surface modes on the basal face of ice Ih." J. Chem. Phys. **128**, 214510 (2008).

[319] I. L. Barnett, H. Groenzin, and M. J. Shultz, "Hydrogen bonding in the hexagonal ice surface." J. Phys. Chem. A **115**, 6039 (2011).

[320] P. J. Bisson and M. J. Shultz, "Hydrogen Bonding in the Prism Face of Ice Ih via Sum Frequency Vibrational Spectroscopy." J. Phys. Chem. A **117**, 6116 (2013).

[321] C. C. Pradzynski, R. M. Forck, T. Zeuch et al., "A fully size-resolved perspective on the crystallization of water clusters." Science **337**, 1529 (2012).

[322] U. Buck, C. C. Pradzynski, T. Zeuch et al., "A size resolved investigation of large water clusters." Phys. Chem. Chem. Phys. **16**, 6859 (2014).

[323] K. Ramasesha, L. De Marco, A. Mandal et al., "Water vibrations have strongly mixed intra- and intermolecular character." Nature Chemistry **5**, 935 (2013).

[324] L. De Marco, K. Ramasesha, and A. Tokmakoff, "Experimental evidence of Fermi resonances in isotopically dilute water from ultrafast broadband IR spectroscopy." J. Phys. Chem. B **117**, 15319 (2013).

[325] P. Hamm and G. Stock, "Vibrational conical intersections as a mechanism of ultrafast vibrational relaxation." Phys. Rev. Lett. **109**, 173201 (2012).

[326] R. Tempelaar, C. P. van der Vegte, J. Knoester et al., "Surface hopping modeling of two-dimensional spectra." J. Chem. Phys. **138**, 164106 (2013).

[327] C. P. van der Vegte, A. G. Dijkstra, J. Knoester et al., "Calculating two-dimensional spectra with the mixed quantum-classical Ehrenfest method." J. Phys. Chem. A **117**, 5970 (2013).

[328] L. H. de la Peña, M. S. G. Razul, and P. G. Kusalik, "Quantum effects in ice Ih." J. Chem. Phys. **123**, 144506 (2005).

[329] J. A. Morrone, V. Srinivasan, D. Sebastiani et al., "Proton momentum distribution in water: an open path integral molecular dynamics study." J. Chem. Phys. **126**, 234504 (2007).

[330] T. E. Markland, S. Habershon, and D. E. Manolopoulos, "Quantum diffusion of hydron and muonium atoms in liquid water and hexagonal ice." J. Chem. Phys. **128**, 194506 (2008).

[331] F. Paesani and G. A. Voth, "Quantum effects strongly influence the surface premelting of ice." J. Phys. Chem. C **112**, 324 (2008).

[332] L. Lin, J. A. Morrone, R. Car et al., "Momentum distribution, vibrational dynamics, and the potential of mean force in ice Ih." Phys. Rev. B **83**, 220302 (2011).

[333] J. R. Schmidt, S. A. Corcelli, and J. L. Skinner, "Pronounced non-Condon effects in the ultrafast infrared spectroscopy of water." J. Chem. Phys. **123**, 044513 (2005).

[334] J. R. Schmidt, S. T. Roberts, J. J. Loparo et al., "Are water simulation models consistent with steady-state and ultrafast vibrational spectroscopy experiments?." Chem. Phys. **341**, 143 (2007).

[335] P. Hamm and R. M. Hochstrasser, "Structure and dynamics of proteins and peptides: Femtosecond two-dimensional infrared spectroscopy." In *Ultrafast Infrared and Raman Spectroscopy*, M. D. Fayer, ed., p 273 (Marcel Dekker: New York 2001).

[336] R. M. Hochstrasser, "Two-dimensional IR-spectroscopy: polarization anisotropy effects." Chem. Phys. **266**, 273 (2001).

[337] Y.-S. Lin, P. A. Pieniazek, M. Yang et al., "On the calculation of rotational anisotropy decay, as measured by ultrafast polarization-resolved vibrational pump-probe experiments." J. Chem. Phys. **132**, 174505 (2010).